Title
The POLARBEAR Experiment: Design and Characterization

Author
Kermish, Zigmund David

Publication Date
2012

The POLARBEAR Experiment: Design and Characterization

by

Zigmund David Kermish

A dissertation submitted in partial satisfaction of the
requirements for the degree of
Doctor of Philosophy

in

Physics

in the

Graduate Division

of the

University of California, Berkeley

Committee in charge:

Professor Adrian T. Lee, Chair
Professor William Holzapfel
Professor Geoffery Bower

Spring 2012

The POLARBEAR Experiment: Design and Characterization

Abstract

The POLARBEAR Experiment: Design and Characterization

by

Zigmund David Kermish

Doctor of Philosophy in Physics

University of California, Berkeley

Professor Adrian T. Lee, Chair

We present the design and characterization of the POLARBEAR experiment. POLARBEAR is a millimeter-wave polarimeter that will measure the Cosmic Microwave Background (CMB) polarization. It was designed to have both the sensitivity and angular resolution to detect the expected B-mode polarization due to gravitational lensing at small angular scales while still enabling a search for the degree scale B-mode polarization caused by inflationary gravitational waves. The instrument utilizes the Huan Tran Telescope (HTT), a 2.5-meter primary mirror telescope, coupled to a unique focal plane of 1,274 antenna-coupled transition-edge sensor (TES) detectors to achieve unprecedented sensitivity from angular scales of the experiment's $4'$ beam to several degrees.

This dissertation focuses on the design, integration and characterization of the cryogenic receiver for the POLARBEAR instrument. The receiver cools the $\sim$20 cm focal plane to 0.25 Kelvin, with detector readout provided by a digital frequency-multiplexed SQUID system. The POLARBEAR receiver was been successfully deployed on the HTT for an engineering run in the Eastern Sierras of California and is currently deployed on Cerro Toco in the Atacama Dessert of Chile. We present results from lab tests done to characterize the instrument, from the engineering run and preliminary results from Chile.

To Mom and Dad

Dad, you instilled in me the curiosity of a scientist, perhaps without either of us knowing it. Our attempts to repair things around the house served as an early introduction to the trials and tribulations of experimental physics.
Mom, your annoyance with our failure to repair things around the house taught me one of the most valuable lessons for an experimentalist: use the right tool for the job. I wish you were here to tell me I've taken too long to get my PhD.

Contents

List of Figures

List of Tables

Acknowledgments

This thesis is the product of many years of effort with help from many people along the way. First, I want to thank my advisor Adrian Lee for welcoming me into his group both when I first started graduate school and when I returned from my brief hiatus. Thanks for all the support during my time at Berkeley. I also want to acknowledge Professors Bill Holzapfel and Paul Richards, my co-advisors of sorts in the Lee/Richards/Holzapfel lab. The combined experience and knowledge of these three scientists was an amazing resource to tap in to.

The other formidable resources of the group are my fellow graduate students and postdocs, without whom POLABEAR would not have happened. Kam Arnold, Bryan Steinbach, Mike Myers, Erin Quealy and Haruki Nishino have all worked closely with me, kept me entertained, and taught me something, all while making substantial contributions to the instrument themselves. The rest of the current Berkeley crew: Toki Suzuki, Ben Westbrook, Nick Harrington, Liz George, Christian Reichardt, Oliver Zahn and Adnan Ghribi have all helped make our lab a great place to work. Some amazing undergraduates have also passed through this group. Jacob Howard, Chase Shimmin, Daniel Flanigan and Marius Lungu not only made great contributions to POLARBEAR but also showed me how awesome Python is. Grad students and postdocs of yore Roger O'Brient, Martin Lueker, Erik Shirokoff, Trevor Lanting, Dan Schwan, Tom Plagge, Jared Mehl, Yuki Takahashi, Brad Johnson, Brad Benson, Nils Halverson, Matt Dobbs, and Sherry Cho have all served as sources of knowledge, advice and procrastination over the years. Special thanks to those who have recently helped me figure out what to do next.

The person perhaps most responsible for my coming to Berkeley was Huan Tran. He convinced a young, impressionable undergraduate that POLARBEAR was *the* experiment to work on (never mind that it wasn't funded at the time). He unfortunately never got to see the experiment he worked so hard on come to fruition. I think we would have had fun in Chile together.

POLARBEAR has grown to a decent sized international collaboration over the years and it's a great group of people to work with. I'd like to recognize several contributors outside of Berkeley I've worked closely with. David Boettger and Nate Stebor from UCSD both became honorary members of the Berkeley crew several times over the past few years. Takayuki Tomaru, Hideki Morii and Tomo Matsumura from KEK have happily jumped in to help mix up stycast, solder tiny connectors, and turn screws. On the analysis-side of things, thanks to Aubra Anthony at the University of Colorado and Nathan Miller at UCSD for their significant contributions to the analysis code, and to Yuji Chinone for his own contributions and illuminating conversations. Aubra also tackled the herculean task of wrangling our analysis meetings. More recently, its been great to see even more of our collaborators contributing with the deployment in Chile and in getting our analysis efforts moving.

Last, I'd like to thank my wife, Janine for her continual love and support.

Chapter 1

Introduction

1.1 Measurements of the CMB

The past two decades have been an incredibly exciting time for researchers making measurements of the Cosmic Microwave Background. Since its discovery by Penzias and Wilson in 1965 [1], there has been steady progress in instrumental sensitivity. Early measurements to characterize the spectrum of the background and search for deviations from isotropy culminated in the measurements made by the far-infrared spectrometer (FIRAS) and differential microwave radiometer (DMR) instruments on board the COBE satellite in the early nineties [2, 3]. FIRAS measured the spectrum of the CMB to unprecedented precision, proving the blackbody nature of the background and dispelling any doubts left in the community about the hot, dense, thermal origin of the radiation. The measured spectrum and 500 σ error bars are shown in Figure 1.1, showing remarkable agreement with the best fit 2.725 Kelvin black body spectrum.

The DMR measured deviations from isotropy at the level of one in 10^5 on scales larger than $\sim 7^\circ$, as shown in Figure 1.2(a). More recently, experiments have continued to probe these primary anisotropies at finer angular scales and measured the influence of effects collectively known as secondary anisotropies as they begin to dominate at even smaller scales. The Wilkinson Microwave Anisotropy Prove (WMAP) followed up on the DMR by making a map of the full sky to 13 arcminute resolution, shown in Figure 1.2(b). WMAP's measurements concluded a decade's worth of effort on ground and balloon-based experiments making smaller scale maps to characterize the angular power spectrum of the anisotropies [4, 5, 6, 7, 8].

The implications of these precise measurements of the CMB intensity on our understanding of cosmology will be discussed in detail in Section 1.2. For now, let us note that while we certainly could appreciate the progress made in creating these high fidelity maps of the microwave sky purely from the viewpoint of instrumental advances, the significance of CMB measurements in driving our understanding of cosmology is astounding. A modern theoretical framework for a standard model of

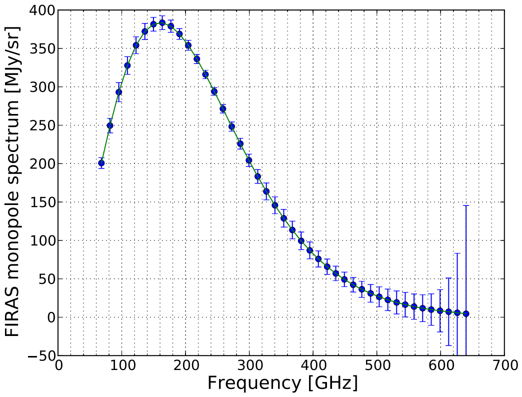

Figure 1.1: A 2.725K blackbody spectrum shown with data from the FIRAS instrument measuring the spectrum of the CMB. Note that the error bars are exaggerated to 500 σ error bars. Data and error bars from Table 4 of [2].

cosmology has developed in large part as a means to explain early measurements of the CMB. Predictions from that standard model have withstood the experimental evidence from modern CMB measurements to an astounding level of accuracy.

With the primary anisotropies now well characterized and secondary anisotropies successfully being probed [9, 10, 11, 12, 13], experimental efforts have shifted to characterizing the polarization of the CMB just as thoroughly. The DASI experiment [14] first measured the polarization of the CMB in 2003 and other experiments have since improved upon the sensitivity, measuring what is known as the E-mode polarization of the CMB with more precision over a larger range of angular scales [15, 16, 17, 18, 19, 20, 21, 22]. The distinction between this polarized signal and the currently undetected B-mode polarization will be made in Section 1.3 when we discuss the physical processes responsible for generating polarization. For the purposes of this discussion, the measured E-mode spectrum is yet another expected signature of the standard cosmological model.

The consistency of the standard cosmological model with measurements over the past two decades is considered quite surprising by some. One could even say that for theorists in the field, this time during which experimentalists have probed the CMB to higher and higher precision and found near complete consistency with expectations, has been disappointingly uneventful. However, the next generation of polarization experiments might be able to probe something very new. The search for the B-mode polarization brings with it the promise of yet more consistency checks, but beyond that the possibility of a signature of the physics responsible for a fundamental aspect of our cosmological framework: inflation.

The theory of inflation is our current best explanation for structure formation

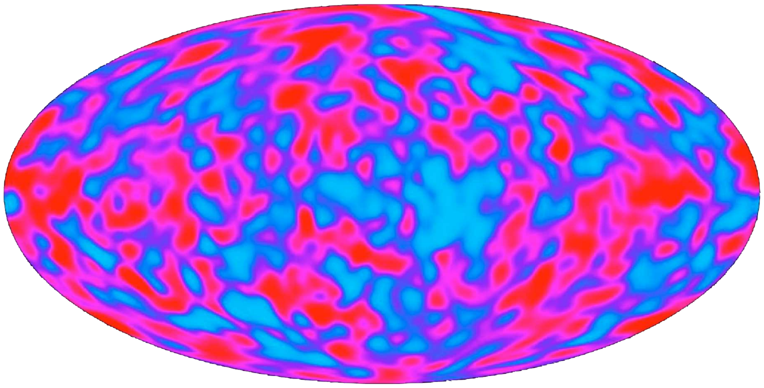

(a) Reduced map of the microwave sky from a weighted sum of 53 and 90Ghz DMR observations with a multiple of the 31GHz DMR map subtracted to minimize sensitivity to Galactic emission. These maps are based on 2 years of DMR observations and shown for comparison. Image courtesy of NASA / the COBE Science Working Group.

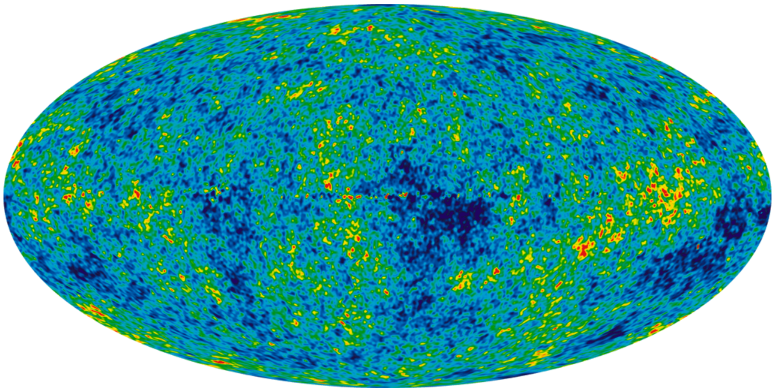

(b) Internal Linear Combination map of the sky using the five WMAP frequencies combined in a weighted average to minimize the Galactic foreground contribution. The map shown is from the seventh year data release. Image courtesy of NASA / the WMAP Science Team

Figure 1.2: Maps of anisotropies in the microwave sky

and several other observables in our universe. A problem with inflation is that a large number of inflationary models, each with a large range of allowed parameter space, can be constructed and still remain consistent with current observations. Large scale B-mode polarization is a unique prediction of a subset of these models, so its detection could help us finally understand what drives inflation and shed light on the high energy physics of the very early universe.

This thesis presents the POLARBEAR experiment. POLARBEAR was designed to measure the B-mode polarization. In this chapter, we provide motivation for our experiment by giving an overview of the relevant topics in cosmology. We begin with a discussion of the inflationary model of cosmology and its observable consequences in the CMB intensity in Section 1.2. We then discuss polarization of the CMB in Section 1.3, again focusing on the observable consequences of inflation. This chapter concludes with a discussion of polarization measurement techniques in Section 1.4. We focus on limiting factors such as instrument loading, foregrounds and systematic errors and how these factors inform instrumental design. The design of the POLARBEAR experiment itself is presented in Chapter 2. Chapter 3 presents the characterization of the POLARBEAR receiver carried out in the Berkeley lab before our initial engineering run deployment to the Cedar Flat site in the eastern Sierras. In Chapter 4, we present the results from that engineering run. Chapter 5 discusses lab measurements in preparation for our science deployment to the Atacama site in Chile. Initial results from the Chilean deployment are presented in Chapter 6.

1.2 Inflation and the CMB

1.2.1 The smooth expanding universe and the big bang

A surprising result of Einstein's theory of general relativity is that the overall dynamics of our universe are dictated by a few simple equations. The following derivation of the dynamics of the smooth, expanding universe can be found in many cosmology or general relativity textbooks (i.e. [23]). If we assume that the universe is homogeneous and isotropic, we have a metric defined by

$$ds^2 = -g_{\mu\nu}dx^\mu dx^\nu = dt^2 - a^2(t)\left[\frac{dr^2}{1+kr^2} + r^2 d\theta^2 + r^2 \sin^2\theta d\phi^2\right] \tag{1.1}$$

In this metric, known as the Friedmann-Robertson-Walker (FRW) metric, $a(t)$ is an overall scale factor to the universe that includes all of the dynamics. Curvature of the universe is parametrized by k. The dynamics can be found by solving the Einstein equations given by

$$R_{\mu\nu} - \frac{1}{2}\mathcal{R}g_{\mu\nu} = 8\pi G T_{\mu\nu}, \tag{1.2}$$

with $g_{\mu\nu}$ defined in 1.1 and the stress-energy tensor, $T_{\mu\nu}$, given by the all the energy fields present in the universe. For a smooth, isotropic universe, the stress energy tensor is that of a perfect fluid with energy density ρ and pressure p

$$T_{\mu\nu} = diag(\rho, -p, -p, -p) \tag{1.3}$$

The time component of Equation 1.2 gives us the Friedmann equation [24]

$$H^2(a) = \left(\frac{\dot{a}}{a}\right)^2 = \frac{8\pi G}{3}\rho(a) - \frac{k}{a^2} \tag{1.4}$$

while a linear combination of the spatial components and the Friedmann equation gives the acceleration equation

$$\frac{\ddot{a}}{a} = -\frac{4\pi G}{3}\left[\rho(a) + 3p(a)\right] \tag{1.5}$$

Equations 1.4 and 1.5 can be solved for the evolution of the scale factor $a(t)$ as a function of the energy content in the universe. Measurements can be made of $H(a)$ using standard candles such as type Ia supernovae in the 'nearby' universe out to redshift of a few to get a handle on the late time evolution of a and the dominant energy contributions at various epochs.

It's useful to rewrite the Friedmann equation in terms of the critical density, $\rho_c = 3H_0^2/8\pi G$, necessary to have a spatially flat universe today and the equation of state $w = p/\rho$ for each energy form present:

$$H^2(a) = H_0^2 \sum_i \Omega_i / a^{3(1+w_i)} - \frac{k}{a^2} \tag{1.6}$$

where $\Omega_i = \rho_i/\rho_c$ and H_0 is the measured value of the Hubble parameter H today.

An obvious consequence of Equation 1.4 is that an expanding universe is a possible solution. This was first suggested soon after general relativity was formulated as an alternative to the steady state models of the universe that were popular at the time [24, 25]. Einstein himself was uncomfortable with the dynamic solutions to his field equation and introduced a cosmological constant term to allow a static solution. However, the expanding universe became an observed fact in 1929 when Edwin Hubble first measured H in our local universe using Cepheid variable stars in galaxies as standard candles [26]. Figure 1.3 shows his results which indicated that the velocity of a distant galaxy is proportional to its distance from us. This is a direct consequence of a non-zero Friedmann equation

$$v = \dot{a}r = Har = Hd \tag{1.7}$$

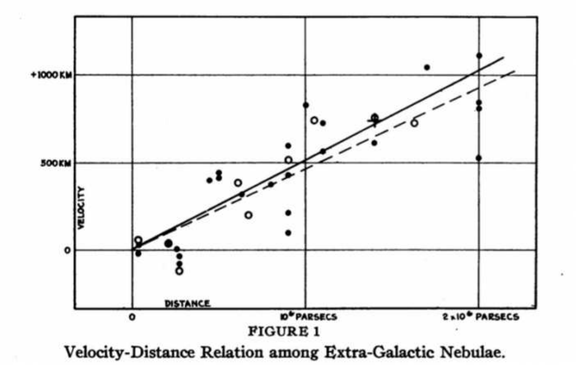

Figure 1.3: Hubble's original Hubble diagram from [26].

If we take this observed expansion and evolve the Friedmann equations back in time, we get to a hot, dense early universe. This simple model of the universe beginning with a hot, 'big bang' and slowly cooling as it expands allows us to make many observable predictions. The most relevant observable for this work is the CMB itself. When the expansion cooled the primordial plasma enough to allow neutral hydrogen to form, the tight coupling between photons and electrons via Thomson scattering was lost. Photons were then essentially able to free stream from that event, commonly referred to as recombination or the 'surface' of last scattering, to us today. CMB photons were also expected to be in equilibrium via that same tight coupling due to Thomson scattering, resulting in the blackbody spectrum observed.

1.2.2 Problems with the big bang

Despite the success of the big bang model in the predicted microwave background and other observables[1], it also has some fundamental problems. The three fundamental problems are known as the horizon problem, the flatness problem and the relic problem. The horizon problem is a simple contradiction between observations and causality. The observed CMB looks the same in all directions on the sky to one part in 10^5, but the horizon size at recombination only fills about 2 degrees on the sky today. Scales larger than this would have not been in causal contact so the uniformity of the CMB and consequently the observed homogeneity of large scale structure in the universe could not be explained by causal effects in the early universe. Theorists would have to appeal to the generally abhorred fine-tuning of initial conditions.

The flatness problem provides another useful example of the need for fine-tuning

---

[1] The relative abundances of light elements predicted via big bang nuleosynthesis (BBN) is another observable that has seen remarkable agreement between measurements and predictions, but an extended discussion is outside the scope of this thesis.

in the standard big bang model. We can rewrite Equation 1.6 as

$$\Omega(t) - 1 = \frac{k}{H(t)^2 a^2} \tag{1.8}$$

where $\Omega(t) = \rho(t)/\rho_c(t)$. To arrive at the essentially flat universe we observe today with $\Omega - 1 \sim 0$ would require $\Omega - 1$ to be incredibly small in the early universe. Small deviations from flatness grow with time, resulting in the universe collapsing in on itself or tearing itself apart and never giving structure such as galaxies, clusters of galaxies, and ourselves time to evolve. This unstable equilibrium point would again require fine tuning to make our own universe a possibility.

Finally, the relic problem comes from our lack of observations of relics such as magnetic monopoles. Relics are predictions of the GUT energy scale phase transition that occur in the early universe as it cools. These phase transitions result in topological defects at the boundaries of transitions. Our current understanding of these transitions would result in a large number of magnetic monopoles today, but none have been observed.

Inflation was introduced as a way to address all of these fundamental problems [27, 28, 29]. Simply stated, inflation calls for a period of exponential expansion in the early universe, shortly after the big bang. This modification to the big bang model not only solves problems with the big bang, but also provides its own unique predictions for observables.

We can see how an accelerated expansion solves the horizon problem by thinking about the comoving horizon, given by $(aH)^{-1}$. During inflation, the Hubble parameter remains nearly constant resulting in an exponentially growing scale factor as the solution to equation 1.4.

$$a(t) \approx a(0)e^{Ht}\,, \qquad H \approx \text{const} \tag{1.9}$$

The result is a decreasing comoving horizon. This allows comoving scales to start out in causal contact at early times before they exit the horizon. After inflation ends and the standard evolution of the universe resumes, scales then re-enter the horizon, as illustrated in Figure 1.4.

This accelerated expansion also easily solves the relic and flatness problems by exponentially diluting the density of relics in our observable universe and by driving any curvature to zero. In fact, the unstable solution of $\Omega(t) - 1 = 0$ is now an attractor solution to Equation 1.8 given the scale factor evolution given by Equation 1.9. An accelerated expansion can be caused by a dominant energy component with negative pressure, more specifically with $p < -\rho/3$ as can be seen from Equation 1.5.

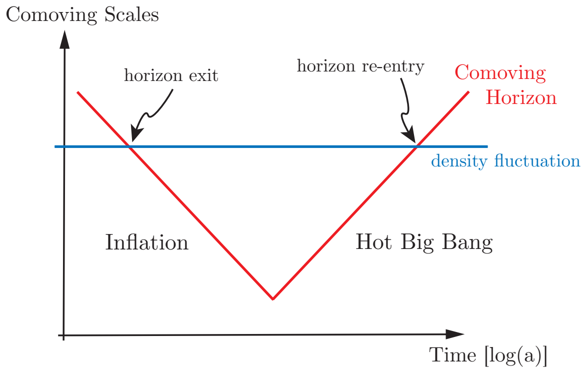

Figure 1.4: An illustration of how inflation solves the horizon problem. Comoving scales start out within the comoving horizon at the left of the plot, but leave the horizon as inflation causes the comoving horizon to shrink. Scales later re-enter the horizon when inflation ends and the standard big bang evolution of the scale factor resumes. Figure from [30].

1.2.3 Slow-roll inflation

While particle physics offers many examples of forms of energy with negative pressures, a canonical example used for inflation is a single scalar field ϕ, 'slowly rolling' down its potential $V(\phi)$. For a spatially homogenous field, the Lagrangian density, given by $\mathcal{L} = \partial^\mu\phi\partial_\mu\phi/2 - V(\phi)$ reduces to $\mathcal{L} = \dot{\phi}/2 - V(\phi)$. The stress energy tensor is given by

$$T^{\mu\nu} = \partial^\mu\phi\partial^\nu\phi - \mathcal{L}g^{\mu\nu} \tag{1.10}$$

The scalar field can then be thought of as a perfect fluid with energy density and pressure given by

$$\rho = \dot{\phi}^2/2 + V(\phi) \tag{1.11}$$

$$p = \dot{\phi}^2/2 - V(\phi) \tag{1.12}$$

From Equation 1.12, we see that a slowly-rolling field with $\dot{\phi} \ll V(\phi)$ gives $p < -\rho/3$, satisfying the requirement for accelerated expansion. The equations of motion of the inflaton field are found by plugging the energy density and pressure of the field back into equations 1.4 and 1.5, with the results

$$H(a)^2 = \frac{8\pi G}{3}\left(\dot{\phi}^2/2 + V(\phi)\right) \tag{1.13}$$

$$\frac{\ddot{a}}{a} = -\frac{8\pi G}{3}\left(\dot{\phi}^2 - V(\phi)\right) \tag{1.14}$$

$$\ddot{\phi} + 3H\dot{\phi} + V'(\phi) = 0 \tag{1.15}$$

From this point on, we assume $k = 0$, as this requirement is quickly met early in inflation. Note that inflation is sustained while $|\ddot{\phi}| \ll |V'|$.

1.2.4 Adiabatic perturbations

If we consider the quantum mechanical nature of the scalar field driving inflation in our slow-roll example, we find a remarkable prediction of inflation. Fluctuations in the scalar field and in the space-time metric create inhomogeneities in the early universe. These serve as the seeds for structure formation through gravitational instability. The spectrum of perturbations produced by inflation are generically adiabatic and nearly scale-invariant. Both scalar and tensor perturbations are expected, and their spectra can be parametrized by

$$P_s(k) = A_s\left(\frac{k}{k_0}\right)^{n_s-1} \tag{1.16}$$

$$P_t(k) = A_t\left(\frac{k}{k_0}\right)^{n_t} \tag{1.17}$$

with pure scale invariance corresponding to $n_s - 1 = n_t = 0$.

In the case of single field slow-roll inflation, the spectra of perturbations are found to be explicitly related to the field potential and its derivatives. Perturbations to the homogenous background metric and inflaton field are given by

$$\phi(t,\mathbf{x}) = \bar{\phi}(t) + \delta\phi(t,\mathbf{x})\,, \qquad g_{\mu\nu}(t,\mathbf{x}) = \bar{g}_{\mu\nu}(t) + \delta g_{\mu\nu}(t,\mathbf{x}) \tag{1.18}$$

A gauge can be chosen such that all scalar and tensor perturbations are encapsulated in the metric perturbation

$$\delta g_{ij}(t,\mathbf{x}) = -a^2(t)\left[2\zeta\delta_{ij} + h_{ij}\right], \qquad \partial_j h_{ij} = h^i_i = 0 \tag{1.19}$$

where ζ, the curvature perturbation on a uniform-density hypersurface, and h_{ij} representing gravitational waves are both gauge-invariant quantities [30]. The curvature perturbations given by

$$-\zeta \equiv \Psi + \frac{H}{\dot{\rho}}\delta\rho \tag{1.20}$$

are related to the quantum mechanical perturbations of the inflaton field following

$$H\frac{\delta\rho}{\dot{\rho}} \approx -H\frac{\delta\phi}{\dot{\phi}} \tag{1.21}$$

This gives us the power spectrum of the curvature perturbations in terms of the inflaton fluctuation power spectrum

$$\langle \zeta_{\mathbf{k}} \zeta_{\mathbf{k}'} \rangle = \left(\frac{H}{\dot{\phi}}\right)^2 \langle \delta\phi_{\mathbf{k}}\, \delta\phi_{\mathbf{k}'} \rangle \tag{1.22}$$

The power spectrum for the scalar perturbations can then be found using the quantum fluctuations of a light scalar field in deSitter space. Similarly, the spectrum for the tensor pertubations are given by the quantum fluctuations of a massless field in deSitter space. The resulting power spectra for scalar and tensor perturbations are then given by

$$P_s(k) = \left(\frac{H}{\dot{\phi}}\right)^2 \left(\frac{H}{2\pi}\right)^2 \Bigg|_{k=aH} = \frac{1}{12\pi^2 M_{pl}^6} \frac{V^3}{V'^2}\Bigg|_{k=aH} \tag{1.23}$$

$$P_t(k) = \frac{8}{M_{pl}^2} \left(\frac{H}{2\pi}\right)^2 \Bigg|_{k=aH} = \frac{2}{3\pi^2 M_{pl}^4} V \Bigg|_{k=aH} \tag{1.24}$$

where we have used the reduced Planck mass, $M_{pl} \equiv 1/\sqrt{8\pi G}$. Simlarly, we can derive a relationship between the spectral indices of the perturbations and the derivatives of the inflaton potential

$$n_s - 1 = M_{pl}\left[2\left|\frac{V''}{V}\right| - 3\left(\frac{V'}{V}\right)^2\right] \tag{1.25}$$

$$n_t = M_{pl}^2 \left(\frac{V'}{V}\right)^2 \tag{1.26}$$

The CMB again provides an observable signature of these perturbations. Focusing first on the scalar perturbations, the initial density perturbations will result in acoustic oscillations of the baryon-photon fluid present before recombination on scales that have re-entered the horizon.

Decomposing a temperature anisotropy map, such as the WMAP measurement shown in Figure 1.2(b), into spherical harmonics

$$\Delta T(\hat{n}) = \sum_{lm} a_{T,lm} Y_{lm}(\hat{n}) \tag{1.27}$$

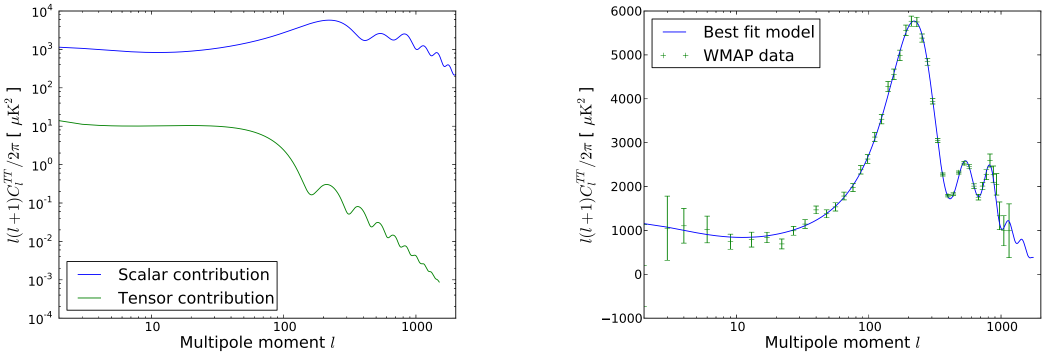

(a) Contribution to the temperature anisotropy spectrum from scalar and tensor perturbations

(b) Measured temperature anisotropy from the WMAP satellite and best fit model spectrum. Data and error bars from [31].

Figure 1.5: Contributions to the temperature anisotropy spectrum and the measured total temperature anisotropy spectrum. All theoretical power spectra computed using the CAMB software package [32].

the angular power spectrum is then given by

$$C_l^{TT} = \langle a_{T,lm} a^*_{T,lm} \rangle \tag{1.28}$$

Inflation predicts the resulting angular power spectrum will be a series of acoustic peaks created by the baryon-photon fluid oscillations and unique to the initial conditions set by inflation and the energy content of the universe while the oscillations are occuring [33, 34, 35, 36]. An example spectrum of temperature anisotropies due to scalar perturbations is shown in Figure 1.5(a). Features such as the angular scale of the first peak, the relative peak heights and positions and the scale of the damping tail of the primary anisotropies are sensitive probes of both the initial conditions set by the inflationary perturbations and the energy content of the universe while the acoustic oscillations were occurring. Tensor modes produced by inflation would also contribute to these primary anisotropies, but only on large scales [37] as also shown in Figure 1.5(a). Measurements of the primary temperature anisotropies already limit this tensor contribution.

The spectrum measured by the WMAP satellite is shown in Figure 1.5(b) along with the best fit cosmological model. This spectrum alone encompasses a large amount of our knowledge of the universe, constraining a slew of parameters to a high degree of accuracy. The clear measurement of the first few acoustic peaks allowed us to conclude that our universe is spatially flat, dominated by dark energy, and that adiabatic perturbations are the dominant mode of structure formation [31].

The ratio of tensor to scalar modes, given by

$$r \equiv \frac{P_t}{P_s} = -8n_t \tag{1.29}$$

is currently constrained to $r < 0.21$ at the 2σ level from measurements of the temperature anisotropies along a large range of angular scales [38]. The constraint is further improved to $r < 0.17$ if other data on baryon acoustic oscillations (BAO) and H_0 are included. This tensor contribution is too small to be measured from the temperature spectrum alone. The polarization of the CMB provides a unique way to help measure r and characterize the tensor perturbation spectrum.

1.3 Polarization of the CMB

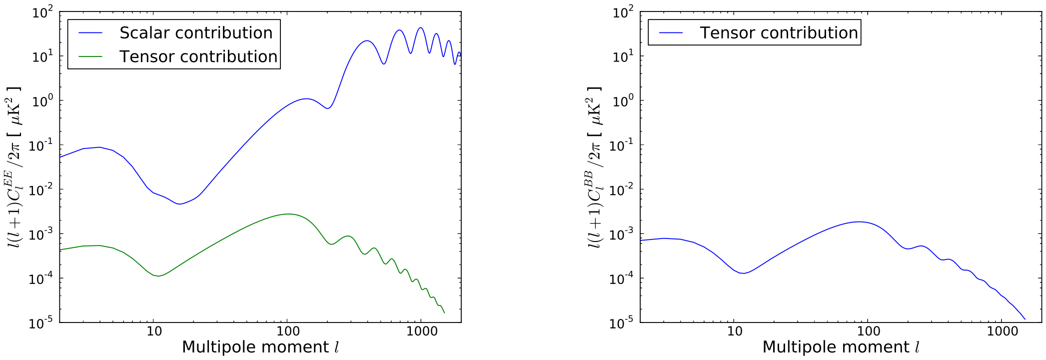

(a) Contribution to the E-mode polarization spectrum from scalar and tensor perturbations

(b) Primordial contributions to the B-mode polarization spectrum uniquely comes from tensor perturbations.

Figure 1.6: Contributions to the polarized spectra

Polarization of the CMB is generated by the polarization dependence of Thomson scattering. The total scattering cross-Section is given by

$$\frac{d\sigma}{d\Omega} = \frac{3\sigma_T}{8\pi}|\hat{\epsilon}' \cdot \hat{\epsilon}|^2 \tag{1.30}$$

with σ_T the Thomson cross-section and $\hat{\epsilon}'$ and $\hat{\epsilon}$ the incoming and outgoing polarizations, respectively. It can be shown that polarization is generated only when a local quadrupolar anisotropy is present in the radiation field [39]. When this requirement is met, a net linear polarization is generated.

The measured polarization field can be parametrized by the Stokes parameters, I, Q, U, V, which characterize the total and polarized intensities in a coordinate system defined with respect to the instrument. With an orthogonal coordinate system defined, the electric field amplitudes E_x and E_y along with the phase difference between these orthogonal components, ϕ fully describes the incident radiation. The Stokes parameters are then given by

$$\begin{bmatrix} I \\ Q \\ U \\ V \end{bmatrix} = \begin{bmatrix} \langle E_x^2 + E_y^2 \rangle \\ \langle E_x^2 - E_y^2 \rangle \\ \langle 2E_xE_y \cos\phi \rangle \\ \langle 2E_xE_y \sin\phi \rangle \end{bmatrix} \tag{1.31}$$

where the time averages are carried out over times that are long compared to the inverse frequency of the radiation and the radiation is assumed to be nearly monochromatic. The Stokes parameter V represents circular polarization and is generally ignored when discussing polarization of the CMB since Thomson scattering at last scattering only generates linear polarization. The Q and U Stoke's parameters that characterize this linear polarization transform like a spin-2 field when rotating through an angle ψ

$$(Q \pm iU)(\hat{n}) = e^{\mp 2i\psi}(Q \pm iU)(\hat{n}) \tag{1.32}$$

We can therefore decompose the polarization field on the sky using a spin-2 basis for the complex polarization

$$(Q \pm iU)(\hat{n}) = -\sum_{lm} (a_{E,lm} \pm i a_{B,lm})\, {}_{\pm 2}Y_{lm}(\hat{n}) \tag{1.33}$$

where ${}_{\pm 2}Y_{lm}(\hat{n})$ are the spin-2 spherical harmonics [40, 41]. This allows us to characterize the polarization field in terms of its rotationally invariant, spin-0 E and B-mode fields and their respective angular power spectra

$$E(\hat{n}) = \sum_{lm} a_{E,lm} Y_{lm}(\hat{n}), \quad B(\hat{n}) = \textstyle\sum_{lm} a_{B,lm} Y_{lm}(\hat{n}) \tag{1.34}$$

$$C_l^{EE} = \langle a_{E,lm} a^*_{E,lm} \rangle, \qquad C_l^{BB} = \langle a_{B,lm} a^*_{B,lm} \rangle \tag{1.35}$$

As is the case with the temperature of the CMB, the physics of the early universe is encoded in the angular power spectra. Different physical effects produce both a different local quadrupolar pattern and a different spatial distribution for the polarized field at recombination [42]. The global symmetries of these effects determine how they contribute to the even parity E-mode and odd-parity B-mode spectra.

Scalar perturbations produce an $m = 0$ local quadrupole oriented parallel to the wave vector $\hat{k}$ of a plane wave perturbation. Physically, this quadrupole is due to the bulk velocity of the baryon-photon fluid at decoupling. This even parity effect leads to a contribution to only the E-mode polarization spectrum. For a given spatial mode of wavenumber k, the quadrupole is of order $kv_\gamma/\dot{\tau}$, where v_γ is the bulk photon velocity, or dipole in the temperature distribution, and $\dot{\tau} \equiv n_e \sigma_T a$ is the differential Thomson optical depth. Since the dipole is of the same order of magnitude as the monopole responsible for the temperature anisotropies, the E-mode spectrum resulting from scalar perturbations is simply suppressed by a factor of $k/\dot{\tau}$. The dipole itself is out of phase with the monopole, so the two spectra are also expected to be out of phase. Both of these effects can be seen in Figure 1.6(a) when compared to the temperature anisotropy spectrum previously showed in Figure 1.5(a).

Tensor modes, however, produce an $m = 2$ local quadrupole oriented in the plane defined by $\hat{k}$ and therefore contribute nearly equally to both E and B-mode polarization spectra, as shown in figures 1.6(a) and 1.6(b). The level of these contributions is directly proportional to r, meaning the contributions to the E-mode polarization from tensor perturbations is small compared to that due to scalar perturbations. For the B-mode polarization, however, the tensor perturbations are the only primordial source that is expected to contribute. A B-mode spectrum detection could then provide a unique, separable detection of the tensor perturbations, allowing a direct measurement of the tensor spectrum amplitude A_t and the tensor-to-scalar ratio r.

1.3.1 Probing inflation

A measurement of the B-mode polarization spectrum would allow us to probe inflation and the physics of the early universe in a new way. As seen by Equation 1.24, in the case of slow-roll inflation, the tensor perturbation spectrum is proportional to the inflaton potential V, leading to the following relation between r and the energy scale of inflation

$$V^{1/4} = 1.06 \times 10^{16}\text{GeV} \left(\frac{r}{0.01}\right)^{1/4} \tag{1.36}$$

A detectable tensor amplitude with $r \approx 0.01$ would suggest that inflation occurred at an energy scale of 10^{16} GeV, near the scale of Grand Unified Theories (GUT). This might allow inflation to provide some insight on the physics at these scales. Measurements of higher order derivatives of the potential found in the spectral indices n_s and n_t would allow the possibility for the potential itself to be reconstructed, providing an incredible observational constraint on the underlying physics driving inflation and physics at GUT scales [30].

Even if single field, slow-roll inflation is not the correct model, measurements of r, n_s, and n_t provide significant constraints. The consistency relation $r = -8n_t$ is valid only for single field slow-roll. In the case of multiple fields involved in slow-roll inflation, this is modified to

$$r = -8n_t \sin^2 \Delta \tag{1.37}$$

where $\sin^2 \Delta$ relates the balance of adiabatic perturbations and isocurvature perturbations that are generated by couplings to the other fields. Similarly, inflation that breaks the slow-roll condition with a non-canonical kinetic term modifies the consistency relation to

$$r = -8n_t c_s \tag{1.38}$$

where the sound speed is now capable of significantly deviating from $c_s = 1$. A breaking of the consistency relation is therefore compatible with either of these two scenarios and can provide evidence against single field, slow-roll inflation. Coupled with effects on other observables such as the level of non-gaussianity in the perturbations, a measurement of significant tilt in the tensor perturbation spectral index would help to distinguish between these different possibilities [30].

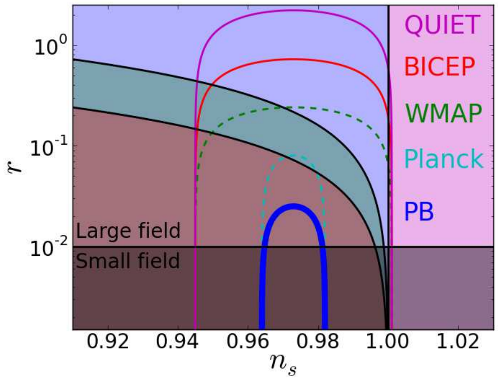

Figure 1.7: Constraints on the $r - n_s$ parameter space of inflationary models for several experiments.

Expressing the tensor to scalar ratio in terms of the number of e-folds of inflation $N = \ln(a_e/a_0)$

$$r(N) = \frac{8}{M_{pl}^2}\left(\frac{d\phi}{dN}\right)^2 \tag{1.39}$$

allows us to relate r to the excursion of the field during inflation:

$$\frac{\Delta\phi}{M_{pl}} \geq 1.06 \times \left(\frac{r}{0.01}\right)^{1/2} \tag{1.40}$$

Single field slow-roll models can then be divided in two classes depending on whether the field excursions are larger or smaller than the Planck mass. Even a measurable upper limit of $r < 0.01$ would effectively rule out all large field models. Such models have $r \sim \mathcal{O}(n_s - 1)$, resulting in $r > 0.01$ given current constaints on n_s.

The parameter space of r and n_s is shown highlighting certain regions in Figure 1.7. Also shown on the plot are the 2σ experimental constraints from various experiments. POLARBEAR, the experiment described in this thesis, will enable a 2σ detection of $r = 0.025$. With this sensitivity, a significant majority of large field slow-roll models can be either detected or ruled out, as seen by the contour in Figure 1.7.

1.3.2 Probing large scale structure

While the tensor perturbations are the only *primordial* source of B-mode polarization, there are other sources to consider. Lensing of the CMB by the intervening clusters of galaxies between the surface of last scattering and observers today can mix E-mode into B-mode polarization. This effect presents a limitation on our ability to measure the B-modes due to inflationary gravitational waves, but there is much science to be found in the lensing B-modes themselves.

The lensed CMB temperature and polarization can be expressed in terms of a remapping on the unlensed CMB by a deflection angle $\nabla\phi$:

$$\begin{aligned} T(\hat{n}) &= T(\hat{\mathbf{n}} + \nabla\phi(\hat{\mathbf{n}})) && (1.41) \\ (Q \pm iU)(\hat{\mathbf{n}}) &= (Q \pm iU)(\hat{\mathbf{n}})(\hat{\mathbf{n}} + \nabla\phi(\hat{\mathbf{n}})) && (1.42) \end{aligned}$$

The deflection angle is given by the gradient of the projected gravitational potential,

$$\phi(\hat{\mathbf{n}}) = -2 \int_0^{z_{rec}} \frac{dz}{H(z)} \Psi(z, D(z)\hat{\mathbf{n}}) \left(\frac{D(z_{rec}) - D(z)}{D(z_{rec}) D(z)} \right) \tag{1.43}$$

where $D(z)$ is the comoving distance to redshift z in a flat cosmology and $\Psi(z, \hat{\mathbf{x}})$ is the Newtonian potential [43, 44]. In the Limber approximation, the power spectrum of the gravitational potential is then given by

$$C_l^{\phi\phi} = \frac{8\pi^2}{l^3} \int_0^{z_{rec}} \frac{dz}{H(z)} D(z) \left(\frac{D(z_{rec}) - D(z)}{D(z_{rec}) D(z)} \right)^2 P_\Psi(z, k = l/D(z)) \tag{1.44}$$

Lensing of the temperature anisotropies effectively smooths out the peaks on small angular scales, mixing different l modes. This effect on the temperature spectrum has already been measured by both ACT and SPT [11, 45].

In the case of the polarized CMB, lensing actually sources a B-mode polarization not present in the unlensed spectra. The spectrum of the induced B-mode can be

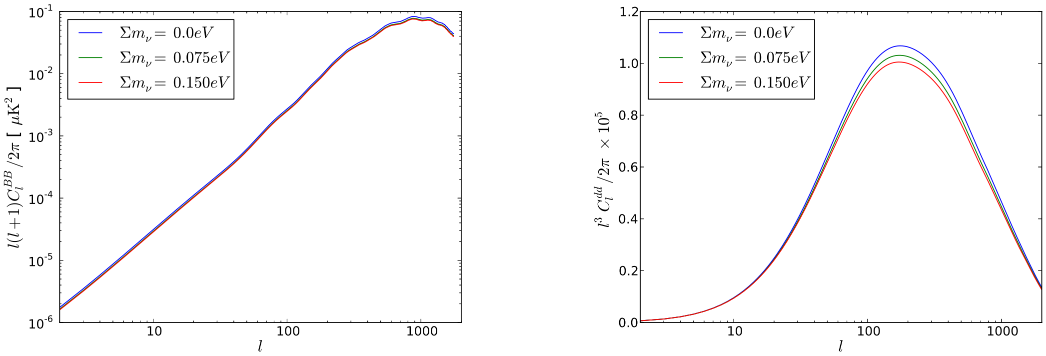

(a) The effect of neutrino masses on the lensed B-mode power spectrum, C_l^{BB}.

(b) The effect of neutrino masses on the resulting deflection power spectrum C_l^{dd}.

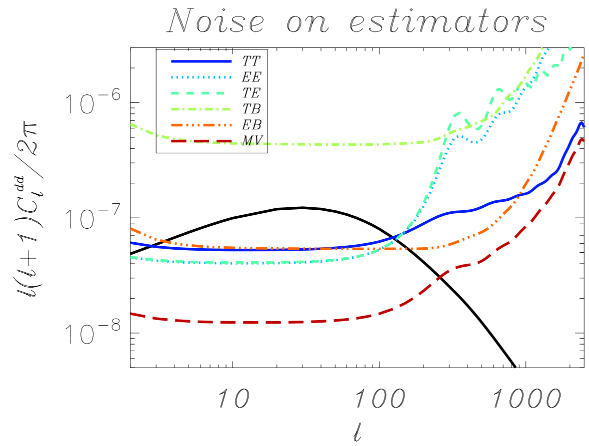

(c) A fiducial C_l^{dd} shown along with the different contributions to the minimum variance estimator of the power spectrum for an experiment with similar sensitivities to POLARBEAR. Note that TT, EE, TE and TB all have roughly equal contribution. Figure from [46].

Figure 1.8: Resulting lensed B-mode spectrum and line-of-sight potential spectrum for several values of Σm_ν.

expressed in the flat sky approximation and to leading order in the gradient approximation as

$$C_l^{BB} = \int \frac{d^2L}{(2\pi)^2} W^2(\mathbf{l}, \mathbf{l} - \mathbf{L}) C_{l-L}^{\tilde{E}\tilde{E}} C_L^{\phi\phi} \tag{1.45}$$

where $\mathbf{l} = (l\cos\varphi_l, l\sin\varphi_l)$, $W(\mathbf{l}, \mathbf{l}') = \mathbf{l}' \cdot (\mathbf{l} - \mathbf{l}') \sin 2(\varphi_l - \varphi_{l'})$ is the mode coupling weighting and $C_l^{\tilde{E}\tilde{E}}$ is the unlensed E-mode spectrum [47] . The B-mode spectrum due to lensing is therefore just the convolution of the unlensed E-mode spectrum with the power spectrum of the lensing potential. This leads to the small scale B-mode polarization generated being a unique probe of large scale structure formation at moderate redshifts ($z < 5$).

One parameter that influences this era of structure formation is the sum of the neutrino masses, Σm_ν. A larger sum of neutrino masses suppresses the growth of structure on scales smaller than the Jeans length for neutrinos [48]. This effect is seen in lensing B-mode signal itself and in the lensing deflection angle power spectrum, shown in figures 1.8(a) and 1.8(b). Since gravitational lensing also affects the temperature and E-mode polarization spectra, a minimum variance estimator constructed using all spectra can enable a reconstruction of the underlying deflection field high signal-to-noise [49]. The contributions to this minimum variance estimator from the various auto and cross spectrum are shown in Figure 1.8(c) for the predicted sensitivity and angular resolution of the POLARBEAR experiment. When combined with data from the Planck satellite mission, POLARBEAR will have a 1σ error of 75 meV on the sum of the neutrino masses. Even when not combined with the larger sky coverage of Planck, POLARBEAR will still provide a 1σ error of 150 meV independently.

1.4 Strategies for polarization measurements

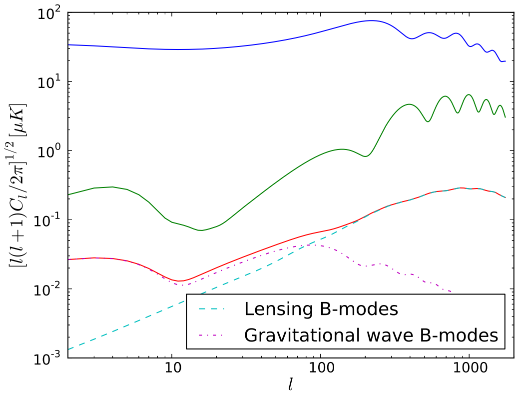

Figure 1.9: Angular power spectrum of polarization anisotropies compared to the temperature anisotropies. The B-modes due to lensing and inflationary gravitational waves with $r = 0.025$ are both shown along with the total B-mode signal.

As we've already noted, detection of the CMB is a challenge and the progress already made is something to appreciate. The RMS of the CMB temperature is a few tens of μK when convolved over degree scales, or ∼20 parts per million of the 2.725 K mean [50]. The measured E-mode spectrum, suppressed by Thomson scattering as shown in Section 1.3, is 20 times lower than that, while the B-mode spectrum is predicted to be at least another order of magnitude below the E-modes. All three spectra are shown together in Figure 1.9. Detection of these small signals clearly requires an increase in overall instrument sensitivity over the previous generation of experiments as well as substantial effort in understanding and limiting the systematic signals inherent to the experiment.

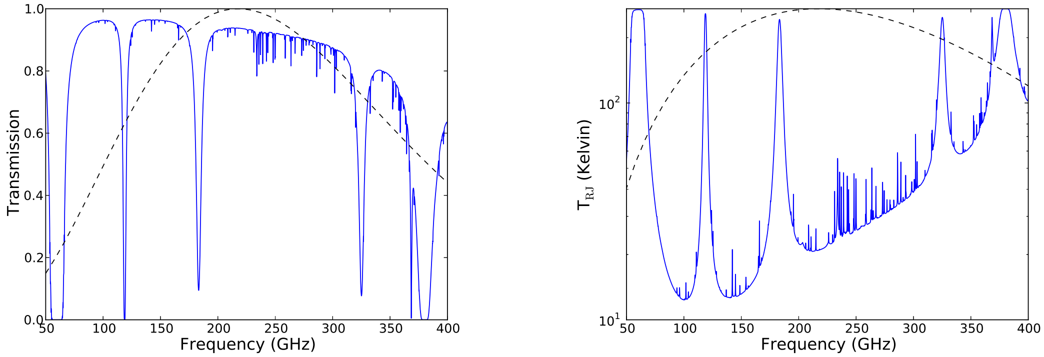

(a) Transmission through the atmosphere at 30 degrees from zenith assuming 1 mm pwv. The spectral dependence of the temperature anisotropies is also shown, scaled in amplitude.

(b) Raleigh-Jeans temperature of the sky at 30 degrees from zenith assuming 1 mm pwv.

Figure 1.10: Atmospheric transmission and sky temperature for 1mm pwv at an angle of 30 degrees from zenith. The windows at 90GHz, 150GHz, and $>$ 200 GHz allow observations of the CMB to be made from the ground.

A wide variety of experiments have fielded, including those that are ground-based, deployed on balloon flights and on satellites in space. Luckily, the spectrum of atmospheric absorption in the microwave region includes several windows with relatively high transmittance in which observations can be made from the ground, as shown in Figure 1.10(a). Beyond that, the atmosphere is believed to have a low level of polarization [51, 52]. This means that if methods can be developed to accurately subtract out the common mode intensity signal, the atmosphere should not be a limiting foreground for ground based polarization measurements. Ground-based experiments are limited in the sensitivity possible due to the additional photon noise of the atmosphere and in the sky coverage they have available to them. As seen in 1.10(b), the sky temperature even at the world's best millimeter observation sites is several times larger than the CMB temperature. While balloon and space-based experiments can remove both these limits, a ground-based experiment with enough sensitivity should be able to provide a detection of either the B-mode signal or the celestial foreground signal that limits that detection on the medium to small angular scales that can be probed with a partial sky measurement. The strategy taken by many researchers in the field has been to use ground-based experiments to push the limits in sensitivity and systematic error control, with the hope of a B-mode detection being possible. Ground-based experiments also serve as a useful testbed for technologies to be used in future balloon and satellite missions, where the associated risks and costs are significantly higher. To date, the most sensitive polarized measurements of the CMB on degree scales have been made from the ground by the BICEP experiment [17].

Ground, balloon and space-based CMB experiments have all used a variety of telescope designs and other optical elements to couple the microwave sky onto detectors. The main goal of these elements of the experiment is to focus microwave radiation at the intended angular resolution onto detectors while providing adequate shielding from background sources such as the Earth and Sun. In the case of a ground-based experiment, shielding from 2π of ground as well as any features of the terrain above the horizon must be considered. Beam sidelobes must also be low enough so that the signal they pick up from the ground or celestial objects is not large enough to limit the experiment's sensitivity. For polarization measurements, the optical elements must also accurately preserve the polarization information from the sky.

Detection of the focused microwave radiation then occurs with one of two methods: coherent or incoherent detection. Coherent detection preserves the phase information of the radiation, allowing for experiments that take advantage of the correlation between different signal paths made before detection. They can also use phase-switching elements as a means of signal modulation. Both interferometers[14, 22] and correlation polarimeters [21, 15] have successfully measured the E-mode polarization signal of the CMB.

Incoherent detectors directly detect the intensity of the incident radiation. While phase information is lost, incoherent detectors such as bolometers have the advantage of providing low noise and high sensitivity over a large range of frequencies. Bolometers measure the temperature rise of an absorbing element due to the incident radiation. Several experiments have also measured the E-mode polarization with bolometric detectors, usually tens to a few hundred of individual horn-coupled detectors employed on a focal plane [16, 17, 18, 19, 20]. The most promising recent developments with bolometer technology has been the use of micro-fabrication techniques to create arrays of hundreds of detectors [53, 54].

1.4.1 Limits on sensitivity

The sensitivity of individual detectors have advanced to the point where they are limited only by background photon loading. The capability to produce large format focal planes lithographically therefore provides a natural way to move forward with sensitivity. More photons per unit time can be collected by optimally sampling the largest possible throughput using thousands of simultaneous detectors. Microfabrication techniques have also been utilized to create polarization sensitive antennas as well as band filtering microwave elements, all on chip [54, 55, 56]. Such developments have greatly simplified the construction of polarization sensitive focal planes with thousands of detectors.

Efforts at Berkeley have focused on development of such large format arrays of polarization sensitive antenna-coupled bolometers. POLARBEAR is the first experiment to utilize the results of this research effort. We'll discuss the details of the detector architecture used in POLARBEAR at length in Section 2.2. With a properly designed detector and an optimized focal plane, the photon background noise provides a fundamental limit in sensitivity for ground-based experiments. This limit drives choices such as site location, where the effective temperature of the atmosphere in the observation band should be minimized, and sets the requirements for receiver design, where every effort must be taken to minimize the effective temperature of the receiver as seen by the detectors in comparison to the sky.

For a detector with a beam limited to area A and solid angle Ω, the power detected from a blackbody source is given by [57]

$$P_{opt} = \int_0^\infty A\Omega\eta(\nu)B(\nu,T)d\nu \tag{1.46}$$

Where $\eta(\nu)$ is the frequency dependent efficiency of the optical system, encompassing the transmission of the optical system, the absorptivity of the detector and the emissivity of the source, and $B(\nu,T)$ is the Plank spectral brightness, given by

$$B(\nu,T) = \frac{h\nu^3}{c^2\exp(h\nu/kT) - 1} \tag{1.47}$$

For a single-moded or diffraction limited detector that is sensitive to one polarization, $A\Omega = \lambda^2$, giving the result

$$P_{opt} = \int_0^\infty \eta(\nu)P_\nu d\nu = \int_0^\infty \eta(\nu)\frac{h\nu d\nu}{\exp(h\nu/kT) - 1} \tag{1.48}$$

For a detector with a narrow bandwidth spectral response, $\Delta\nu$, centered at ν_c we can carry out the integral to find the load on the detector from each optical element of temperature T

$$P_{opt} \approx \eta h\nu_c\Delta\nu n_{occ} = \eta\Delta\nu n_{occ}kT\beta_c = \eta\Delta\nu kT_{eff} \tag{1.49}$$

We've used the occupation number of photons per mode,

$$n_{occ} = [\exp(h\nu_c/kT) - 1]^{-1} = [\exp(\beta_c) - 1]^{-1} \tag{1.50}$$

and defined the effective Raleigh-Jeans temperature for a source $T_{eff} = \beta_c n_{occ} T$. We've also defined the band averaged fractional throughput η. In the literature, η is often called the optical efficiency. However, there are systems such as POLARBEAR where the beam is purposefully truncated at a cold aperture stop to improve sidelobe performance. The optical efficiency is then usually reported as the fractional throughput divided by the beam truncation loss. This distinction is being made for clarity. As we've defined it here, the fractional throughput η quantifies the percentage of the power seen by a detector from a source at the input of the receiver compared to what would be seen if the detector had perfect efficiency to that same source.

In the case of a Raleigh-Jeans source where $h\nu_c \ll kT$ and $\beta \ll 1$, Equation 1.49 simplifies to

$$P_{opt} = \eta \Delta\nu kT \tag{1.51}$$

The receiver and other optical components of the instrument should be engineered so that the total effective Raleigh-Jeans temperature of the instrument as referenced to the sky, often called the 'dewar load', remains below the effective temperature of the atmosphere. As we'll discuss in more detail in Section 2.3.5, for a large aperture experiment, achieving this goal while effectively limiting thermal loads on cryogenic stages from infrared radiation is quite a challenge. Filters must be engineered that demonstrate both high rejection of out of band radiation via either absorption or reflection and very low loss in band.

We can calculate the fractional throughput and dewar load expected for an optical system by looking at the loss and corresponding load contribution from every optical element. Such an estimate is generally limited by knowing the physical properties of the individual elements as well as being able to fully simulate the system accurately enough to get good estimates for both the temperatures of the elements themselves, in the case of absorptive filters, or the final effective termination temperature, in the case of reflective filters. Table 1.1 shows the results of such an estimate for the expected configuration of the POLARBEAR receiver in Chile based on best guesses for material losses and element and termination temperatures. In practice, the dewar load must be measured and modifications made if the load is found to limit the sensitivity of the instrument.

1.4.2 Beam asymmetries and systematic errors

While kilopixel bolometer focal planes and a well designed cryogenic receiver will address the need for increased sensitivity, another fundamental challenge to polarized CMB measurements is the mitigation of systematic errors. Since the B-mode polarized signal is expected to have such a low amplitude relative to both the E-mode polarization and the total intensity, non-idealities in the instrument itself can easily produce spurious signals that swamp the B-modes. Significant effort has been put

Table 1.1: Table of fractional throughput and dewar load contribution estimates for the POLARBEAR receiver.

Element	Termination temperature	Loss or reflection	Cumulative fractional throughput	T_{RJ} referred to window (K)
Load resistor mismatch	0.5	0%	100%	0
Miscrostrip filter	0.25	8.2%	100%	0
Antenna mismatch	0.25	0%	91.8%	0
Antenna backlobe	0.25	9.0%	91.8%	0
Lenslet surface reflection	0.25	15.0%	83.5%	0
Collimating lens	7	5.0%	71.0%	0.36
Aperture stop truncation	6	13.0%	67.5%	0.68
Aperture lens	7	5.0%	58.7%	0.3
Metal mesh reflection	7	2.0%	55.8%	0.1
Metal mesh absorption	7	2.0%	54.6%	0.1
Field lens	7	5.0%	53.6%	0.3
Metal mesh reflection	7	2.0%	50.9%	0.1
Metal mesh loss	20	2.0%	49.9%	0.4
4K IR shaders	20	2.0%	48.9%	0.4
HWP reflection	25	2.0%	47.9%	0.5
HWP loss	70	2.0%	46.9%	1.6
Metal mesh reflection	50	2.0%	46.0%	1.1
Metal mesh loss	90	2.0%	45.1%	2.0
Teflon filter absorption	90	4.0%	44.2%	3.8
Teflon filter reflection	100	1.6%	42.4%	1.6
77K IR shaders	80	5.0%	42.4%	4.0
300K IR shader	100	1.0%	40.3%	1.0
300K Zotefoam window	300	1.0%	40%	2.9
Total			40% $\eta\Delta\nu$ =12GHz	21.2

into understanding these instrument systematics and optimizing system designs to either minimize these effects or provide a means to characterize and remove them.

Systematic signals can be divided into two categories: those that leak intensity into polarization and those that mix polarization states. Such effects can be modeled generically by constructing the Muller matrix that transforms the Stokes vector on the sky into that observed by the detector [58, 59]. The individual elements of this matrix must be found for a specific instrument.

For the case of a bolometric polarimeter such as POLARBEAR, where polarization is measured by using two bolometers sensitive to orthogonal polarization states, a useful intuition can be gained by considering the properties of the differential beam for each pixel. Modeling each detector beam with an elliptical Gaussian profile

$$B(x,y) = \frac{1}{2\pi\sigma_x\sigma_y} \exp\left[-\frac{(x-\rho_x)^2}{2\sigma_x^2} - \frac{(y-\rho_y)^2}{2\sigma_y^2}\right] \tag{1.52}$$

with individual detector ellipticities given by $e = (\sigma_x - \sigma_y)/(\sigma_x + \sigma_y)$, the relevant differential beam properties are defined in table 1.2.

Effect	Definition
Differential gain	$g = g_1 - g_2$
Differential beam width	$\mu = \frac{\sigma_1 - \sigma_2}{\sigma_1 + \sigma_2}$
Differential pointing	$\rho = \rho_1 - \rho_2$
Differential ellipticity	$e = \frac{e_1 - e_2}{2}$
Differential rotation	$\epsilon = \frac{1}{2}(\epsilon_1 + \epsilon_2)$

Table 1.2: Definitions of terms used in differential beam property discussions.

As seen from the differential beam patterns for each effect, shown in Figure 1.11, these couple to the temperature and polarization fields on the sky by convolving them with a monopole, dipole or quadrupole beam pattern. The result is that instrumental effects causing either differential gain, differential beam size, differential pointing or differential ellipticity will lead to leakage between temperature and polarization, while differential rotation will mix polarization states.

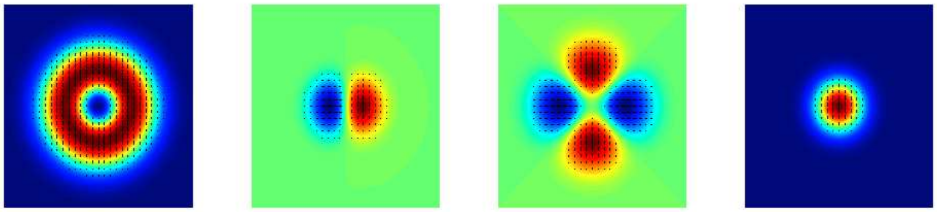

Figure 1.11: Differential beam patterns from the differential beamwidth, differential pointing, differential ellipticity and differential gain, respectively from left to right. Figure from [60].

How these different effects contribute to systematic errors in power spectrum estimations can be calculated analytically by expanding the beams and convolving with the sky maps in Fourier space [60, 46]. The result is dependent both on the inherent differential beam properties of the receiver and on the properties of the scan strategy employed. In table 1.3, we summarize the contributions as calculated in [60].

Effect	ΔC_l^E	ΔC_l^B
Differential gain	$g^2 f_1 \star C_l^T$	$g^2 f_1 \star C_l^T$
Differential beamwdith	$4\mu^2 (l\sigma)^4 f_1 \star C_l^T$	$4\mu^2 (l\sigma)^4 f_1 \star C_l^T$
Differential pointing	$c_\theta^2 C_l^T J_2^2(l\rho) + J_1^2(l\rho) C_l^T \star f_2$	$s_\theta^2 C_l^T J_2^2(l\rho) - J_1^2(l\rho) C_l^T \star f_2$
Differential ellipticity	$I_1^2(z) c_\phi^2 C_l^T$	$I_1^2(z) s_\phi^2 C_l^T$
Differential beam rotation	$4\epsilon^2 C_l^B$	$4\epsilon^2 C_l^E$

Table 1.3: Contributions of various differential beam asymmetries to systematic errors in the E-mode and B-mode angular spectra. $c_\phi \equiv \cos 2\phi_1 - \cos 2\phi_2, s_\phi \equiv \sin 2\phi_1 - \sin 2\phi_2, c_\theta \equiv \cos 2\theta, s_\theta \equiv \sin 2\theta$. I_n and J_n are the modified and cyclindrical Bessel functions, respectively. The parameter $z = (l\sigma)^2(1+\mu)^2 e$ while g, μ, ρ, e and ϵ are the beam properties defined in table 1.2. The f_n are terms that depend on scan strategy.

For a given proposed scan strategy and desired instrument sensitivity, constraints on the level of acceptable differential beam asymmetries can be found. Modulation of the polarization angle on the sky through methods such as sky rotation, boresight telescope rotation, and optical elements such as half-wave plates can all be utilized along with an optimized scan strategy to ease constraints on beam asymmetries by minimizing the f_n parameters. In Figure 1.12, we show the contribution from different beam asymmetry effects compared to the B-mode spectrum. The beam asymmetry values used are those necessary to make a detection of the B-mode polarization due to inflationary gravitational waves with $r = 0.025$. As seen in the figure and shown in table 1.4, the most stringent requirement comes from the differential gain of the instrument. This instrumental polarization effect leaks the temperature anisotropy spectrum directly into the polarization spectra with an effective beam on the same scale as the instrument's beam. With sky rotation and a method to modulate the polarization, this requirement is reduced by more than two orders of magnitude. In Figure 1.12 note that for a smaller beam experiment, the other beam asymmetry effects only become an issue for characterizing smaller angular scales of the spectrum due to the smaller effective beams from these effects.

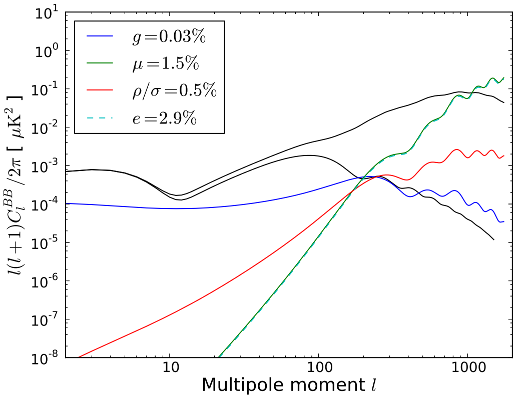

Figure 1.12: Contribution of various differential beam asymmetries to systematic errors in C_l^B for an experiment with 4' FWHM beams. The levels of each individual differential beam asymmetry is shown in the legend and the scan strategy is assumed to be optimally poor.

1.4.3 Scan strategies

The choice of scan strategy not only plays an important role in mitigating systematic errors due to beam asymmetries as discussed in the previous Section, but also in mitigating many other sources of systematic error. In the case of a ground-based experiment, certain scan strategy choices allow for better characterization and removal of errors related to scan-synchronous signals such as those created by pickup of ground signal. A scan strategy that approaches a pixel on the resulting map from many angles provides a method to understand and correct for systematic errors produced from time stream filtering of atmospheric noise or scan-synchronous contributions [61]. This is especially true for polarization measurements where such cross-linking also averages down spurious polarization signals.

More fundamentally, the patch size chosen limits the maximum angular scale that can be probed and the noise on the measurement due to cosmic variance. How the patch is scanned coupled with the low frequency noise performance of the detectors will limit the largest angular scale that can be probed.

For a patch on the sky of angular extent $\Delta\Theta$, the maximum angular scale that can be probed is given by $l_{min} \approx 180°/\Delta\Theta$. For a given C_l, assuming uniform coverage of the entire scan patch, the error on the measurement is given by

$$\Delta C_l^{TT} = \sqrt{\frac{2}{(2l+1)f_{sky}}}\left(C_l^{TT} + w_T^{-1}W_l^{-1}\right) \tag{1.53}$$

where w_T is the temperature sensitivity given by

Effect	Requirement for r=0.025 (no mitigations)	Requirement for r=0.025 (with sky rotation & HWP)
Differential Gain	0.03%	9%
Differential Pointing	0.5%"	2%
Differential Beam Width	1.5%	< 100%
Differential Ellipticity	2.9%	2.9%
Differential Beam rotation	0.52°	0.52°

Table 1.4: Requirements on differential beam properties to allow a detection of $r = 0.025$.

$$w_T^{-1} = \frac{4\pi f_{sky} s^2}{t_{obs}} \tag{1.54}$$

$$W_l^{-1} = e^{l(l+1)\sigma_b^2} \tag{1.55}$$

In the above equations, t_{obs} is the total observing time of the experiment, $s \equiv \mathrm{NET}/\sqrt{N_{det}}$ is the sensitivity for an instrument with N_{det} detectors, each with a noise equivalent temperature of NET, f_{sky} is the fraction of sky covered and σ_b is the beam width of the instrument [61, 62, 63]. The first term in Equation 1.53 corresponds to the sample variance that occurs from the limited samples we have for a given scale, otherwise known as cosmic variance. The second term is due to the instrument noise. For the case of a polarization measurement to measure the spectra C_l^{EE} or C_l^{BB}, w_T in Equation 1.53 should be replaced with the polarization sensitivity which is given by $w_p^{-1} = 2 \times w_t^{-1}$ in the case of a bolometric experiment.

To observe the first low-l peak due to inflationary gravitational waves at $l \sim 6$ where the gravitational lensing B-mode has become subdominant, near full-sky coverage is needed. This is difficult to accomplish from the ground due to limitations in accessible sky and the required sensitivity for a reasonable observation campaign. To attempt to observe the second inflationary gravitational wave peak near $l \sim 100$, a much smaller fraction of the sky can be observed. Instrument sensitivity can then be focused on that smaller patch, resulting in a deeper map in the same observation time [64]. The patch size in this case needs to only be large enough to enable a clean separation of E and B-modes to be made when using efficient power spectrum estimators [65, 66]. New estimators that do not mix E and B-modes have been introduced that remove this constraint entirely [67]. These 'pseudo-C_l' estimators allow the patch size to be chosen to solely maximize sensitivity to the angular scale of interest. Depending on the level of r and the sensitivity of the instrument, the experiment might also be required to 'de-lens' the B-mode spectrum near $l \sim 100$ by simultaneously measuring the lensing B-mode at smaller angular scales.

Departures from a purely white spectrum of detector noise further complicate estimating sensitivity. For a given angular mode l the detector frequency that sky signal will appear in depends linearly on the scan speed of the instrument

$$f \propto v_{scan} \times l \tag{1.56}$$

Slow drifts in the stability of the instrument as well as slowly varying optical signals such as atmospheric fluctuations contribute to low frequency noise with a $1/f$ characteristic spectrum. This leads to significantly higher noise for the largest angular scales that end up buried in the $1/f$ spectrum for a given scan speed. In the case of a polarization measurement, the $1/f$ noise due to the atmosphere fluctuations and other correlated sources of drift can be mitigated to some level. Since two detectors will be differenced for a bolometric detector to measure the Q and U linear polarization parameters, common-mode drifts are naturally removed. The choice of scan strategy can also help to mitigate $1/f$ noise effects from the atmosphere for temperature measurements [61, 68]. Even with these mitigations to common-mode $1/f$ effects, there is still a source of low frequency noise remaining inherent to the detectors themselves that is not necessarily correlated between detector pairs.

One way to reduce this remaining noise penalty on larger angular scales is to simply scan the telescope faster. The limitation here is generally provided by the physical constraints of the telescope or telescope vibrations coupling into detectors via microphonic or thermal variations. Various methods of modulating the sky signals can be used to raise the "science band" of the instrument that sky signals fall in away from the $1/f$ end while maintaining reasonable scan speeds. For temperature measurements, experiments often quickly 'chopped' the signal using oscillating mirrors near the instrument output. For mid-latitude sites, the rotation of the sky with respect to the instrument provides another natural, though slower, method of modulation. A similar modulation can be introduced using boresight rotation of the entire instrument, as has also been employed.

1.4.4 Polarization modulation

While sky rotation provides the cleanest method to modulate polarization since the modulation is introduced independent of the instrument, there are other means one can use, especially if faster modulation is desired. In the case of polarization, optical elements can be used to rotate the polarization pseudo-vector relative to the instrument's detectors. A common technique is to utilize a stepped or continuously rotating half-wave plate (HWP) [69, 70, 71].

Any birefringent crystal that can be cut so the ordinary and extraordinary axes lie perpendicular to the optical axis can be used to introduce a phase change between the two perpendicular polarizations. The resulting phase difference is given by

$$\Delta\phi = \frac{2\pi d(n_e - n_o)\nu}{c} \tag{1.57}$$

where n_e and n_o are the indices of refraction along the extraordinary and ordinary axes, respectively, ν is the frequency of light and d is the thickness of the wave plate. For a given frequency ν, the plate thickness can be chosen so that $\Delta\phi = \pi$ and linear polarization remains preserved while the orientation of the polarized vector can be changed by rotating the wave plate. For a rotation through an angle θ, the polarization pseudo-vector will be rotated by an angle 2θ. With a total power detector sensitive to one linear polarization, a HWP rotating at a frequency f then results in a signal that is modulated by $4f$.

Continuously rotating a HWP therefore provides another way to move the polarization signal well above the $1/f$ knee of the detectors. Other advantages include a measurement of both Q and U in each pixel as the HWP rotates without the need to rely on a neighboring pixel oriented 45° from the first, separation from scan-synchronous signals, and reduced systematic errors from improved cross-linking. A continuously rotating HWP also complicates the instrument in many ways. Accurate demodulation is now needed to extract sky signals and if a cold HWP is desired to minimize its contribution to loading, a cryogenic bearing needs to be implemented.

A simpler approach can be taken with a stepped HWP. While this doesn't provide the Q/U measurement in a single pixel or the higher frequency science band advantages, it does allow improved studies of systematic errors and can be coupled with the scan strategy to approach ideal cross-linking in polarization maps. It also avoids some of the systematic errors that need to be considered with a continuously rotating HWP since they can be more easily calibrated out with a stepped system.

It should be noted that in practice, measurements are made of a frequency dependent source with an instrument having a finite bandwidth around a center frequency. This leads to imperfect polarization efficiency and other systematic effects that need to be considered with half-wave plates. Broader band polarization modulation is possible by using several half-wave plates stacked at specific orientations relative to each other [72, 73].

1.4.5 Foregrounds

Perhaps the most fundamental limit to a measurement of the polarization of the CMB is the presence of foreground signals. Our own galaxy provides foreground signals from three distinct sources: synchrotron radiation, free-free emission, and emission from dust grains. The level of each of these foreground signals varies spatially across the sky, their intensities have different spectral dependencies, and the level of polarization can also vary across the sky. For experiments making full-sky maps, the

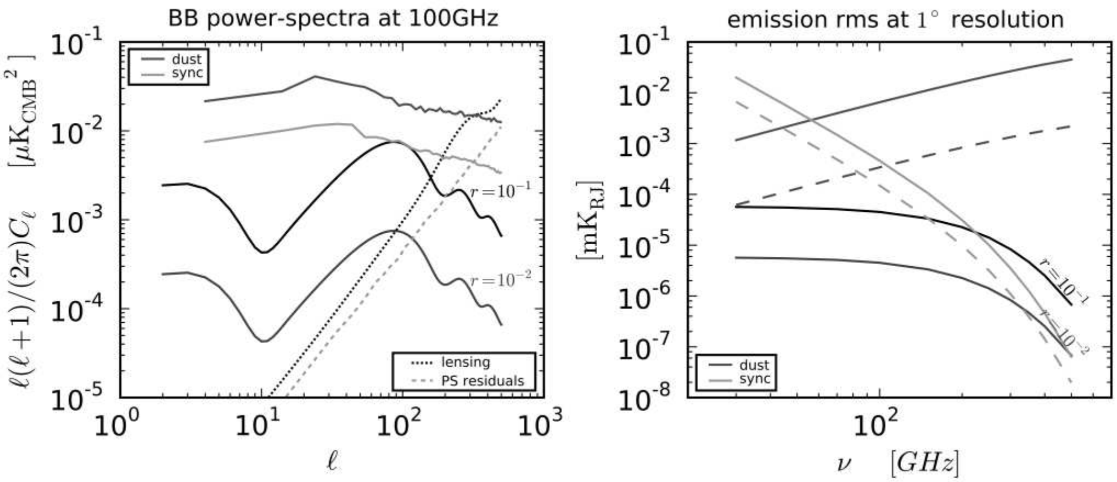

(a) The left panel shows predicted polarized foreground levels from dust and synchrotron in the cleanest 55% of the sky compared to the B-mode polarization. The right panel shows the spectral dependence of synchrotron and dust polarized foregrounds compared to that of the B-mode polarization. Figure from [74]. See the original source for details on the foreground model used.

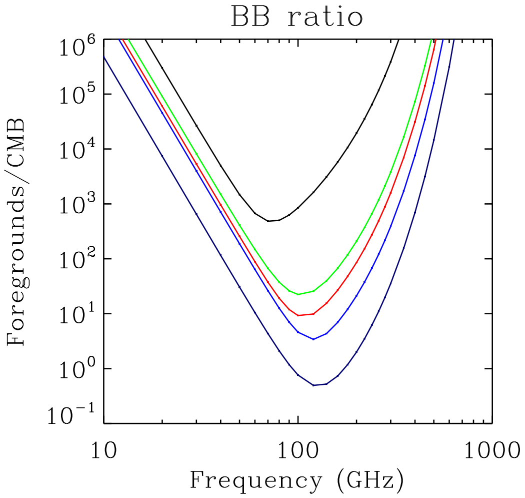

(b) The ratio of foreground power to B-mode power as a function of observation frequency and sky fraction. Figure from [75]. See the original source for more details on the foreground model.

Figure 1.13: (a) Angular and spectral dependence of dust and synchrotron polarized foregrounds. (b) Polarized dust foreground level spectral dependence for several patch sizes.

unpolarized foregrounds are a substantial contribution to the microwave power. The different spectral dependencies of the foreground components allow multiple frequency observations to be utilized in characterizing and removing them. This becomes an even more difficult challenge when trying to measure the polarization of the CMB since the ratio of polarized foregrounds to polarized CMB signal is expected to be much greater [74, 75]. In the case of the inflationary B-mode signal, both dust and synchrotron emission dominate over the full sky even for the cleanest 55 % of the sky as shown in Figure 1.13(a).

When making maps on smaller sections of the sky, it's possible that foregrounds can be subdominant. This depends on the polarized fraction of the dust component, which is not particularly well characterized. For the cleanest 10 × 10 degree patch on the sky, the minimum of the ratio between polarized foregrounds and an inflationary B-mode signal occurs at $\sim$ 150 GHz assuming a 5% polarized dust fraction and a tensor-to-scalar ratio of $r = 0.01$ [75], as shown in Figure 1.13(b). Dust is the dominant foreground above 100 GHz, so this ratio could improve if the polarized fraction is in fact less than 5% for dust. For measuring the smaller scale lensing B-modes, foregrounds should be subdominant on cleaner, small patches of the sky.

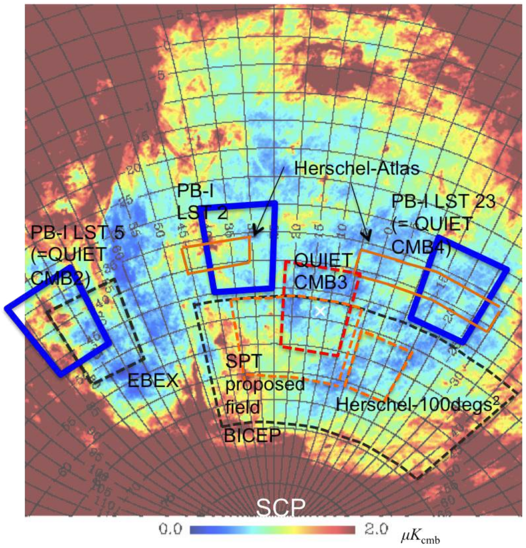

Figure 1.14: The modeled intensity of the dust foreground in the clean 'southern hole' of the sky. Planned observation patches for POLARBEAR are shown along with observation patches from several planned and fielded experiments. Figure courtesy of Tomotake Matsumura.

The approach of several experiments has been to measure the polarized microwave sky at 150GHz in these cleaner regions of the sky with the hope of detecting the inflationary B-mode signal for a large enough r and small enough polarization fraction. The so called ‘southern hole’ of the microwave sky is shown in Figure 1.14 along with the observation patches selected for several previous and current experiments. The planned patches for POLARBEAR are shown in blue. Note that they overlap with two patches mapped by the QUIET experiment and by the proposed EBEX experiment sky patch to utilize these measurements at complementary frequencies to characterize and remove foregrounds. The POLARBEAR patches also overlap with patches from the Herschel survey. This would allow POLARBEAR to utilize the IR galaxy survey and carry out cross-correlation studies between the galaxy surveys and the CMB polarization.

1.4.6 The state of the field

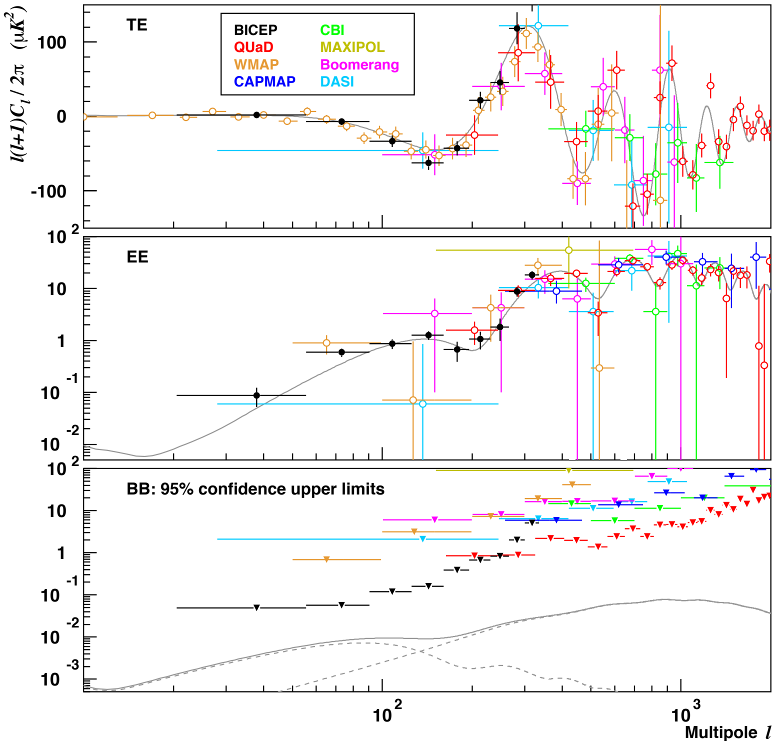

Figure 1.15: A compilation of existing polarization measurements from [17].

A wide variety of experiments have now measured the E-mode polarization spectrum as well as the cross correlation between temperature anisotropies and the E-modes. As shown in Figure 1.15, errors on the E-mode polarization are still far from being cosmic variance limited and no B-mode polarization has yet been detected. Experiments have recently focused on measuring the large-scale polarization and the current best limit from the BICEP experiments limits $r < 0.7$ [17]. As mentioned earlier, a better constraint on r currently exists from temperature data combined from large and small scales, limiting $r < 0.21$ [38]. The most recent results on the small angular scale B-modes from the QUAD experiment [18] were not sensitive enough to detect the expected B-mode lensing signal.

The PLANCK satellite that recently finished collecting data is expected to improve these limits considerably. PLANCK's $5'$ beams and detector sensitivity should allow a detection of the small scale B-mode due to lensing. However, PLANCK is not sensitive enough to either significantly improve constraints on r or to map the lensing deflection field.

There are currently several experiments similar to BICEP in concept that are making deeper maps of the polarized CMB at degree scales in an attempt to detect the B-mode polarization due to inflationary gravitational waves. In addition to these large scale measurements, the 10-meter South Pole Telescope has recently been upgraded with a polarization-sensitive receiver to enable characterization of the B-mode at medium and small angular scales and the ACT 6-meter telescope will be upgraded in the near future, with plans to characterize the small angular scale B-mode polarization, exclusively. As we'll discuss in the next chapter, POLARBEAR is a unique instrument in the current landscape of CMB polarimeters.

Chapter 2

The POLARBEAR Experiment

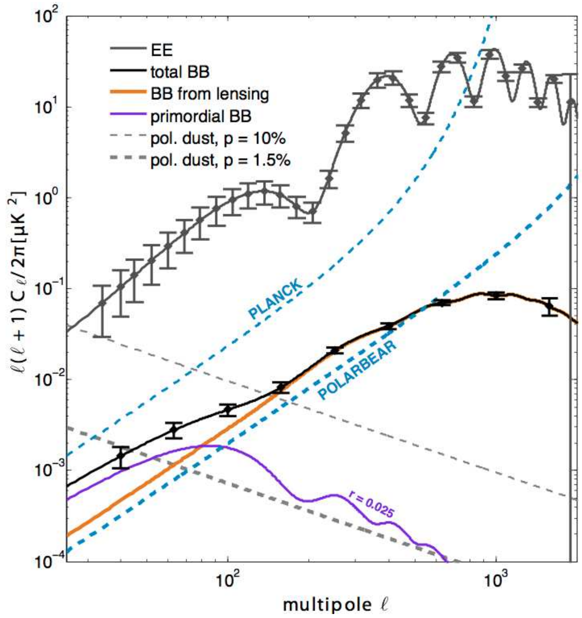

Figure 2.1: Predicted error bars for the POLARBEAR experiment. Figure courtesy of Josquin Errard.

POLARBEAR was designed to have both the sensitivity and angular resolution to detect the expected B-mode polarization due to lensing at small angular scales, while still being able to further limit constraints on or possibly make a detection of the B-mode polarization caused by inflationary gravitational waves. As discussed in Section 1.4, there are many challenges to making these measurements and several different approaches. POLARBEAR takes the approach of observing a foreground clean,

Table 2.1: POLARBEAR instrument specifications

NET_{det}	$480\ \mu\mathrm{K}\sqrt{s}$
N_{det}	1274
Beam FWHM	$4'$
f_{sky}	1.7 %
Efficiency	18 %
Observing time	2 years
Temperature map depth	$6.3\ \mu\mathrm{K} - \mathrm{arcminute}$

small patch of the sky with a medium angular resolution telescope from the ground. Systematic errors due to beam asymmetries are mitigated by the small beam size of the experiment. Further control over systematic errors is addressed by both a stepped cryogenic half wave plate and a scan strategy that utilizes the sky rotation from a mid-latitude site. Nearly an order of magnitude increase in sensitivity is accomplished over the previous generation of instruments observing these angular scales by utilizing a kilo-pixel focal plane architecture in a cryogenic receiver. The projected sensitivity of the instrument is shown in Figure 2.1 where we plot the predicted error bars on the E-mode and B-mode polarization spectra. The assumptions that go into this calculation are shown in table 2.1.

In this chapter, we discuss the details of the POLARBEAR instrument. We begin with a discussion of the Huan Tran telescope in Section 2.1. The Huan Tran telescope (HTT) was designed to give the required angular resolution and allow scan speeds fast enough to optimally map the angular range of interest. The telescope also has the flexibility to allow future upgrades to the camera. We discuss the design of the kilo-pixel focal plane architecture used in POLARBEAR in Section 2.2, highlighting the detector technology used as well as the readout and practical concerns involved with tuning and operating the system. In Section 2.3, we present the POLARBEAR receiver, giving an overview of the cryogenic system and highlighting the challenges in reaching our design goals. Section 2.4 gives a brief overview of software systems used to integrate the experiment.

2.1 The Huan Tran Telescope

The Huan Tran Telescope (HTT) is an off-axis Gregorian design that satisfies the Mizuguchi-Dragone condition. An advantage of off-axis telescopes is that they have clear apertures, lacking secondary support structures obstructing the beam that are required for on-axis telescopes. These structures can scatter or diffract signal from the ground into the main beam and severely limit performance. The Mizuguchi-Dragone condition sets the tilt between the symmetry axes of the parent conics for the primary and secondary mirrors in an offset dual reflector antenna. The resulting antenna has a rotational symmetric equivalent paraboloid, giving low cross polarization and astigmatism over a large diffraction-limited field of view [76, 77]. A Gregorian design has the advantage of a smaller secondary when compared to the alternative crossed design and allows easier baffling to prevent far sidelobes due to scattering at the receiver window. One disadvantage is that the Gregorian design suffers from a smaller diffraction-limited field of view than the equivalent crossed-dragone design [78].

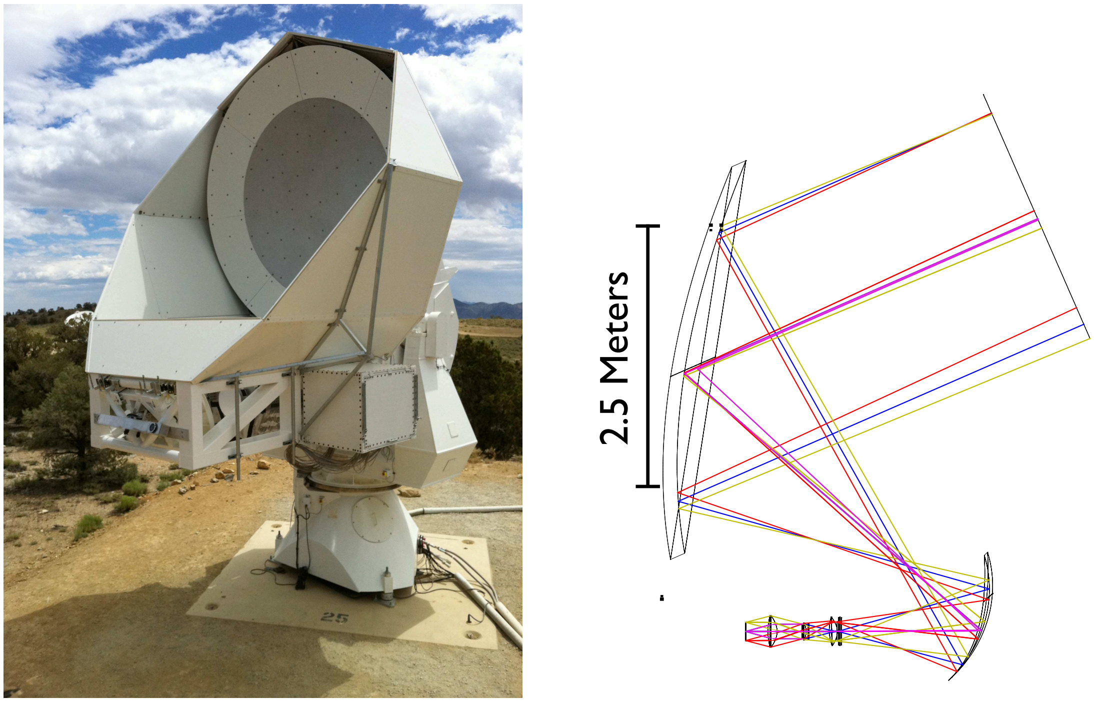

(a) The Huan Tran Telescope as assembled at the Cedar Flat site in the eastern Sierras.

(b) A ray-tracing schematic of the telescope optics. The 2.5 meter primary focuses onto the secondary mirror and cold optics reimage the telescope focus to a flat, tele-centric focal plane.

Figure 2.2: The Huan Tran Telescope

A ray-tracing schematic of the HTT's optical design is shown in Figure 2.2(b). HTT has a 2.5 meter primary mirror that is precision machined from a single piece of aluminum to a 53 μm rms surface accuracy. High surface accuracy and the monolithic design of the mirrors limit loss due to both diffuse scattering [79] and knife-edge diffraction in the case of segmented mirrors. Our 2.5 meter primary gives a 4 arcminute beam at 150GHz, allowing the experiment to probe out to $l \sim 2500$ and cover the peak of the lensing B-mode spectrum at $l \sim 1000$.

Note the primary mirror focus serves as an effective location for an aperture to keep stray light from entering the system incident on the secondary at high angles. The secondary mirror itself is machined to a 37 μm rms surface accuracy.

The telescope focus lies just in front of the first reimaging lens of the receiver shown in the schematic. For a more detailed view of the optical path once inside the receiver, see Figure 2.10. The field, aperture, and collimating lenses serve to reimage the curved focal plane of the telescope to a flat, telecentric focal plane that can be coupled to planar, micro-fabricated detector arrays. The reimaging optics were designed to give the telescope a 2.3° diffraction-limited field of view for a 19cm focal plane.

The telescope was built by VertexRSI[1] (now a part of General Dynamics). The specifications given to Vertex for the telescope performance are summarized in table 2.2 along with the performance we've currently achieved. Measurements of the current performance will be discussed further in Chapter 4 where we present results of the Cedar Flat deployment. A photo of the telescope fully assembled at Cedar Flat is shown in Figure 2.2(a)

Table 2.2: Telescope performance specifications and current performance

Description	Specification	Current performance
Maximum Az/El Velocity	$4°/s$	$4°/s$
Maximum Az/El Acceleration	$2°/s^2$	$2°/s^2$
Azimuth Travel	±200°	±200°
Elevation Travel	+40° to +90°	+40° to +90°
Tracking error	10 arcmin	10 arcsec
Pointing reconstruction error	10 arcsec	12 arcsec rms

2.2 A kilopixel focal plane architecture with TES detectors

As mentioned in Section 1.4.1, detector technologies have advanced to the point where sensitivity is limited only by photon noise due to background loading. Higher sensitivity measurements of the polarization of the CMB thus require more photons be collected per unit time. The most straightforward way to accomplish this is to design an experiment with many simultaneous detectors. Efforts at Berkeley over the past decade have focused on developing the technologies necessary for a kilopixel focal plane architecture. We've developed multiple transition edge sensor (TES) bolometer coupled technologies that leverage micro-fabrication techniques to produce large

---

[1] http://www.gdsatcom.com/vertexrsi.php

arrays of detectors. TES detectors utilize the sharp superconducting transition of materials to provide sensitive optical power to electrical current detection with excellent linearity and gain stability.

The APEX-SZ and SPT-SZ experiments used TES detectors coupled to spider web absorbers below conical feedhorn arrays to make measurements of the CMB intensity at small angular scales [80, 81, 82, 83, 84]. I contributed to early development of the APEX-SZ focal plane architecture by designing the flexible circuit board technology used to couple the filtering inductors and capacitors to device wavers and by designing the focal plane structural and wiring assembly. Many of the lessons learned in that design were brought over to the focal plane designs of both SPT and POLARBEAR.

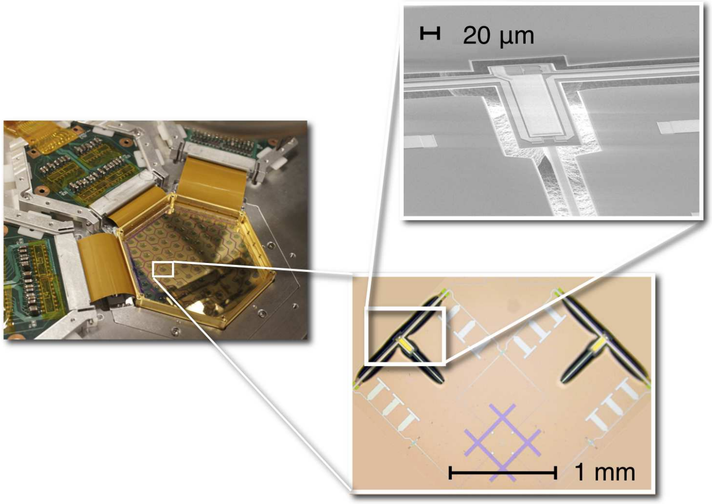

Figure 2.3: A POLARBEAR device wafer. The top left image shows a device wafer installed in its wafer holder below a lenslet array. The bottom right inset shows an image of a single pixel and the top right inset further magnifies, showing an SEM image of the bolometer island. Images courtesy of Kam Arnold.

For POLARBEAR, the focal plane architecture consists of antenna-coupled TES detectors [55]. Radiation is coupled onto microstrip using polarization sensitive dual-slot dipole antennas [85]. Silicon lenslets and a silicon spacer directly above the antennas provide a simulated elliptical lens, defining the beam directivity and narrowing the Gaussian beam width inherent to the antenna [86, 87]. On-chip band filtering is then done using resonant structures before power is dissipated at a load resistor located on a thermally isolated island. A TES thermistor sits on this island and converts changes in optical power to modulated current through the AC biased thermistor. Each pixel in a POLARBEAR detector module contains two orthogonal polarizations. Figure 2.3 shows a single device wafer with 91 pixels. Details on the optimization, design and construction of these device wafers can be found in [88]. Seven wafers are used in the POLARBEAR focal plane for a total of 1274 detectors paired in 637 pixels.

Readout for these TES arrays has also been developed in parallel. Current through a low impedance, voltage-biased TES detector can be read out using a superconducting quantum interference device (SQUID) by converting the current to magnetic flux with an inductor coil. The SQUID converts the magnetic flux produced at the input coil to a voltage across its junctions. The SQUID voltage can then be read out by standard room temperature electronics. Linearity in the squid response can be accomplished over a large bandwidth by utilizing a feedback loop to keep the flux at the maximum transimpedance point. This readout method easily scales to large format detector arrays since the wide bandwidth of the SQUID readout allows the currents from many AC biased detectors to be summed and read out on a single SQUID [89, 90, 91, 92, 93, 94]. A multiplexing technology such as this frequency multiplexing scheme is necessary for a successful kilopixel architecture both from the cryogenic standpoint of limiting the heat load due to room temperature wiring down to milliKelvin stages and from the practical standpoint concerning cost and ease of assembly.

A schematic of the frequency domain multiplexing (fMux) architecture developed at Berkeley is shown in Figure 2.4(b). Alternative multiplexing technologies have been developed by other research groups that employ time-domain multiplexing [95]. Both technologies have been successfully deployed in experiments and there are tradeoffs between the two designs. While both address the need for a lower wirecount to mitigate thermal loads and simplify assembly, one advantage of the fMux scheme is that it only requires a single cold SQUID array amplifier for each multiplexed set of detectors. Time-domain technologies currently use a SQUID on each detector as a switch in addition to a SQUID array amplifier per multiplexed set of detectors, driving up the overall cost and system complexity. The major disadvantage of the fMux architecture as currently designed comes from the complications that arise when working with high frequency bias currents and stray impedances within the system and the resulting possibility for instability, as well as instabilities due to bandwidth limitations.

For our frequency domain multiplexing scheme, we send a series of carrier bias currents at different frequencies, referred to as a comb, down a single pair of bias lines. Inductors and capacitors wired in series with each TES detector pick out a single, resonant frequency in the comb for each detector's bias. Sky signal then modulates the current flowing through the detector, which is read out as side-bands in the carrier signal.

More details on both the TES detector technology and the demodulation of sky signal will be discussed further in sections 2.2.2 and 2.2.3 of this thesis. For a more extended discussion of the Berkeley developed frequency multiplexer technology, see [96, 97].

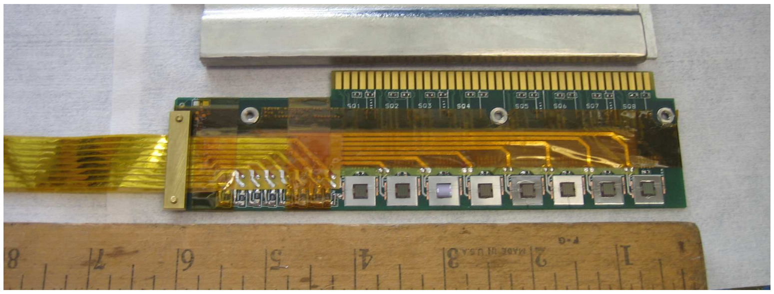

(a) Photo of an assembled squid amplifier readout card

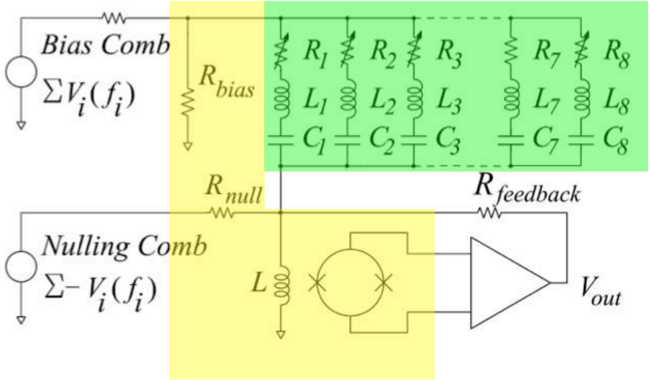

(b) Schematic of the frequency multiplexed readout scheme developed at Berkeley.

Figure 2.4: The components shaded in yellow in (b) reside on the 4 Kelvin squid amplifier readout card shown in the photograph of (a). The shaded green region encompasses the components cooled to 0.25 milliKelvin. These include the bolometers and the inductors and capacitors used for resonant circuits in the AC biasing scheme, housed on the wafer modules described in detail in Section 2.2.1.

2.2.1 Wafer module design

Mechanically holding the POLARBEAR device wafers provided a more difficult challenge than the device wafers made for both the APEX-SZ and SPT experiments. For both of those experiments, the devices were built on the same side of the silicon wafer as the spider-web absorbers. In fabricating the wafers, silicon was etched away from the same side of the wafer that radiation would be incident upon to release both the absorbing spider-webs and the bolometer islands. This meant the entire back-side of the silicon wafer could easily be used to mechanically constrain the wafers. An Invar wedge was used behind the device wafer, bonded to the silicon using Apiezon-N thermal grease. Invar has the advantage that it is well matched to the thermal expansion coefficient of silicon, giving negligible differential thermal contraction between the wafer and the holder. For each wafer module, connections to the flexible circuit boards holding the resonant filters for multiplexing (LC boards) were made by wirebonds on the same side of the devices and along a single edge for each of the six wedges that comprised the focal plane. Readout components were then easily arranged around the focal plane perimeter.

For POLARBEAR's device wafers, radiation is incident on dual-slot dipole antennas that are etched out of a Niobium ground plane. The 'sky-side' of the wafer is opposite the 'device-side' where TESs, resonant structures and microstrip lines are fabricated and where silicon is again etched away to release the thermally isolated bolometer islands. We could therefore not attach anything to either side of the silicon wafers outside of a small perimeter without either blocking incoming radiation or damaging released devices. Furthermore, electrical contact to the Niobium ground plane had to be made by whatever device holder was developed to complete the Faraday cage necessary to provide a clean RF environment for detectors and cold readout components. Connecting to the wafers is further complicated since POLARBEAR's device wafers are hexagonal rather than triangular wedges to better tile the circular focal plane. The increased pixel count per wafer meant wire bonds to LC boards had to be made along 3 edges of that same small perimeter used to mechanically hold the devices. The use of too much space outside the device wafer footprint to make these connections or for LC board components would require sacrificing costly focal plane real estate and losing overall instrument sensitivity.

An Invar holder and LC board design were developed that addressed these issues. As shown in Figure 2.5(a), contact is made to the Niobium ground plane of the wafer along the 1mm edge that also provides mechanical support. A thin Invar clip, 0-80 screws, and lock washers are used to maintain pressure on the combined lenslet and device wafer stack. Wirebonds are made to three flexible circuit boards that are attached to the Invar wafer holder with rubber cement. The flexible LC boards are fed through small slots in the Invar holder. A wafer in the process of having wirebond connections made to LC boads is shown in Figure 2.5(b). A blackened plate then covers the device-side of the wafer, providing a cold, milliKelvin termination point for the antenna backlobes. and protecting the wirebonds. LC boards can then be folded one at a time and attached to the back surface of the module. A completely assembled detector module with an alumina lenslet array attached and full readout using 3 folded LC boards is shown in figures 2.5(c) and 2.5(d). This compact configuration allows the readout components to all lie within the device wafer footprint and adds a minimal amount of space for hardware necessary to mechanically constrain the module. Modules are then installed in the focal plane using the 3 remaining accessible edges at the back of the module. The focal plane assembly will be discussed in Section 2.3.2.

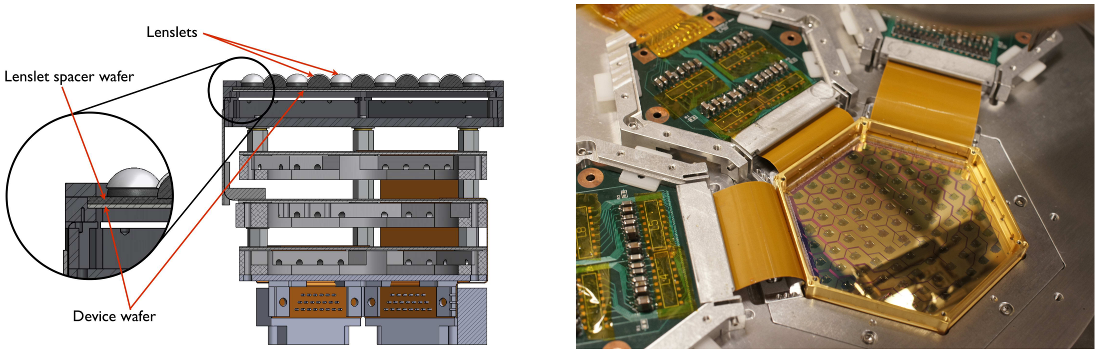

(a) CAD rendering of a wafer holder

(b) An unfolded wafer module.

(c) A wafer module as seen from the sky-side. The lenslet array as well as the Invar array holder and readout support hardware can be seen from this view.

(d) A wafer module as seen from the readout side. Here, we can clearly see the three folded LC boards below the device wafer. The flexible LC boards unfold, allowing access to wirebond to the device wafer.

Figure 2.5: A wafer module assembly

2.2.2 Electro-thermal feedback and bolometer operation

There are several advantages to TES detectors that arise from the sharpness of the superconducting transition. A simple bolometer electro-thermal circuit is shown in Figure 2.6. Voltage-biasing a TES provides electro-thermal feedback (ETF) since the bias power depends on the detector's temperature-dependent resistance $P_b = V^2/R(T)$. When additional optical power is deposited on the detector, the bolometer island heats up, raising the resistance and therefore lowering the bias power. This feedback compensates for the optical power, keeping the total power and the bolometer temperature effectively constant. The strength of this feedback is parametrized by the ETF loopgain $\mathcal{L} = P_b\alpha/GT$, where $G = dP/dT$ is the differential thermal conductance along the weak link between the bolometer island at $\sim T_c$ and the thermal bath and $\alpha = d\log R/d\log T$ parametrizes the steepness of the superconducting transition.

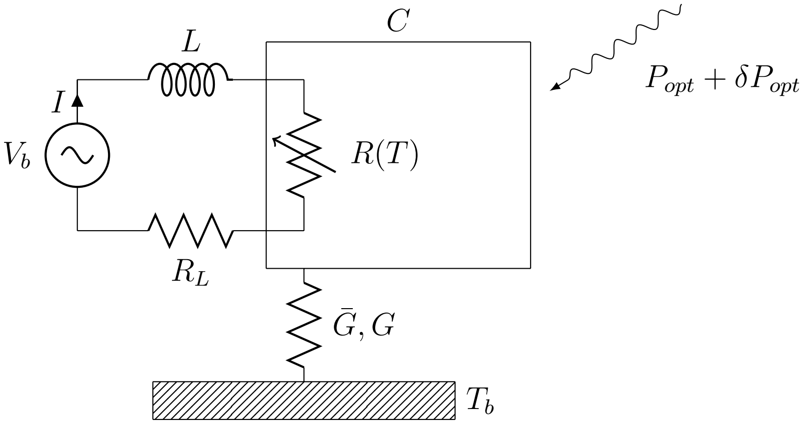

Figure 2.6: The electrothermal circuit of a bolometer. Parasitic series reactances and inductances R_L and L are shown for illustration.

Other advantages to TES bolometers can be illuminated by solving for the response to small signals [98, 99, 100]. In the case of a simple DC bias, the power flow is given by

$$\begin{aligned} P_{opt} + \delta P_{opt} e^{i\omega t} + P_b - (V_b^2 \alpha / R T_c) \delta T e^{i\omega t} \\ = \bar{G}(T_c - T_b) + G \delta T e^{i\omega t} + i\omega C \delta T e^{i\omega t} \end{aligned} \tag{2.1}$$

where P_{opt} is the background optical load, δP_{opt} the sky signal at angular frequency ω, $\bar{G}$ is the average thermal conductance of the weak link, and C the heat capacity of the bolometer. Equating the static terms gives us

$$P_{opt} = \bar{G}(T - T_b) - P_b = P_{sat} - P_b \tag{2.2}$$

where we've introduced the saturation power $P_{sat} \equiv \bar{G}(T_c - T_b)$. Since the measured bias power would go to zero as $P_{opt} \to P_{sat}$, the saturation power is the maximum optical power that can be detected by a bolometer with detector properties $\bar{G}$ and T_c.

Equating time varying terms allows us to solve for the responsivity

$$S_i \equiv \frac{\delta I}{\delta P_{opt}} = -\frac{1}{V_b} \frac{\mathcal{L}}{1 + \mathcal{L} + i\omega\tau_0} = -\frac{1}{V_b} \frac{\mathcal{L}}{\mathcal{L} + 1} \frac{1}{i\omega\tau} \tag{2.3}$$

where we've used the ETF loopgain and the intrinsic thermal time constant of the detector $\tau_0 = C/G$. In the last equality, we see that the detector has an effective time constant $\tau = \tau_0/(\mathcal{L} + 1)$. Electro-thermal feedback provides an enhancement to the detector time constant by a factor of $(\mathcal{L}+1)$. Beyond that, in the high loopgain limit for signals slower than the timeconstant τ, the responsivity $S_i \sim -1/V_b$.

These results can also be extended to the case of an AC biased bolometer such as those used in POLARBEAR[2]. With a voltage bias given by

$$V(t) = V_p \cos \omega_c t \tag{2.4}$$

where ω_c is the carrier frequency and $V_p = \sqrt{2} V_{RMS}$ is the peak voltage amplitude, we can similarly use energy conservation to solve for the response to small changes in power

$$\delta I = -\frac{\sqrt{2}\delta P_{opt} \cos \omega_c t}{V_{RMS}} \frac{\mathcal{L}}{1+\mathcal{L}} \frac{1}{1+i\omega\tau} \tag{2.5}$$

and the loopgain is now given by

$$\mathcal{L} = \frac{\alpha V_{RMS}^2}{RTG} = \frac{\alpha P_b}{TG} \tag{2.6}$$

Assuming the ability to frequency-lock and phase-lock demodulate, the responsivity of an AC biased detector differs from the DC case since

$$S_i \equiv \frac{\delta I}{\delta P_{opt}} = -\frac{\sqrt{2}}{V_{RMS}} \frac{\mathcal{L}}{1+\mathcal{L}} \frac{1}{1+i\omega\tau} \tag{2.7}$$

As we'll show in Section 2.2.3, the output of the digital frequency domain multiplexer to a modulated current of the form

$$I(t) = s(t) \cos \omega_c t \tag{2.8}$$

is given by

$$y(t) = \frac{A_c}{2} s(t) = \frac{X}{\sqrt{2}} s(t) \tag{2.9}$$

where X is the overall conversion factor between the RMS carrier current amplitude and the DC counts returned by a demodulator at frequency ω_c. Looking back at Equation 2.5, we see it follows this form with

$$s(t) = -\frac{\sqrt{2}\delta P_{opt}}{V_{RMS}} \frac{\mathcal{L}}{1+\mathcal{L}} \frac{1}{1+i\omega\tau} \tag{2.10}$$

The output of the multiplexer to sky signals which modulate the current through the bolometer is given in units of ADC counts by

$$y(t) = \frac{-\delta P_{opt} A_c}{\sqrt{2} V_{RMS}} \frac{\mathcal{L}}{1+\mathcal{L}} \frac{1}{1+i\omega\tau} = -X \frac{\delta P_{opt}}{V_{RMS}} \frac{\mathcal{L}}{1+\mathcal{L}} \frac{1}{1+i\omega\tau} \tag{2.11}$$

---

[2] The extensions to AC biased responsivity in this section were worked out in collaboration with Bryan Steinbach. The original derivations can be found in [101].

In practice, bolometers must be tuned to a point in the transition with sufficient loopgain that the responsivity remains nearly constant with changing optical loads due to the atmosphere over a range of elevations. Significant effort was involved in understanding the biasing circuitry and the digitial multiplexer readout system sufficiently to enable tuning of thousands of detectors. One detail about our biasing and readout scheme that we haven't discussed to this point is the nulling circuitry. To limit the dynamic range required of the SQUID and readout system, a 'nulling' signal for each detector that is completely out of phase with the bias carrier signal is summed with the modulated carriers before the resulting signal is fed through the SQUID input coil, as shown in Figure 2.4(b). The SQUID dynamic range is then only required to be large enough to accommodate the small signal variations seen in the sidebands. This also creates a virtual ground at the summing point of the circuit. In the first deployments of the fMux system with SPT and APEX-SZ, detectors on a comb were tuned serially by turning off the nulling current for a single detector and stepping its bias voltage down, reading out the bolometer current using the DC value returned by the demodulator. The resulting IV curve was then used to determine how far in the transition the detector was biased. This method proved to be an inaccurate method for biasing because the virtual ground at the summing point is lost with the absence of adequate nulling. The resulting non-zero input impedance to the SQUID coil in series with the TES means that the apparent TES resistance inferred from the measured IV curve will be lower than the final resistance upon nulling by twice the series impedance [102]. Detectors were found to latch superconducting upon nulling after tuning because of this effect.

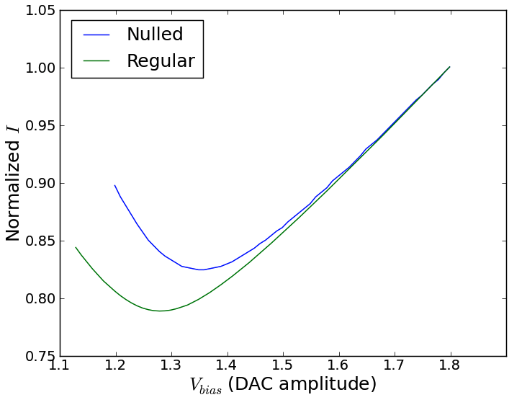

Figure 2.7: Comparison of zero nuller demodulator readout IV curve to nulled IV curve.

This issue was addressed in POLARBEAR by developing algorithms to bias the detectors while nulling is maintained. Small voltage bias steps are taken and nulling re-established at each step with the measured demodulated output. The current through the bolometer is then given by the required nuller value rather than readout by the nearly zeroed output of the demodulator. The series impedance presented by the input coil is also effectively zeroed at each bias step. The resulting IV curve provides an accurate representation of the real voltage and current across the TES in the absence of other parasitics in the bias circuit. A comparison of the IV curves produced by the two methods is shown in Figure 2.7. Another advantage of this technique is that it allows the detectors in a comb to be biased in a more parallel way since small bias steps can be taken simultaneously and nulled serially without surpassing the available dynamic range of the SQUID.

Once biased into the transition, the loopgain can be estimated several ways. The most direct method is to measure the time-constant of the bolometer and compare it to the measured time-constant at the 'turnaround' point in the transition where $dI/dV = 0$ and $\mathcal{L} = 1$. The bolometer time-constant can be measured by looking at the transfer function of the bolometer response to signals as a function of frequency. The most end-to-end test is to measure this response using optical signals. A method was also developed that allowed time-constants to be characterized in dark test receivers using electrical signals input onto the carrier lines of the bolometer [103]. The result of such a measurement is shown in Figure 2.8.

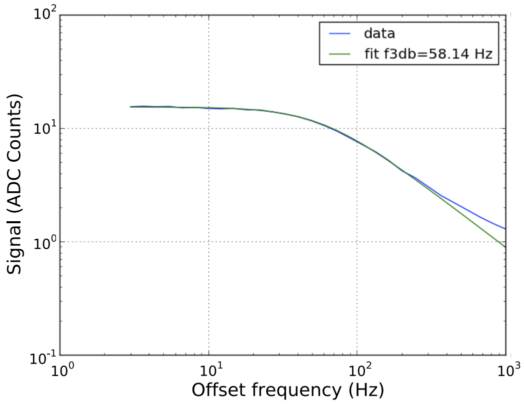

Figure 2.8: An example measurement of τ by measuring the response of the detector as a function of frequency with electrical signals.

For moderate loopgains, an estimate of the loopgain can also be made directly from the IV curve. The result is given by [104]

$$\mathcal{L} = \frac{\partial V/\partial I - V/I}{\partial V/\partial I + V/I} \tag{2.12}$$

Figure 2.9 shows a sample IV curve and the loopgain calculated from it using the above equation. Since this loopgain estimate doesn't require a separate measurement, this method was most commonly used to estimate loopgain when needed during dark and lab tests.

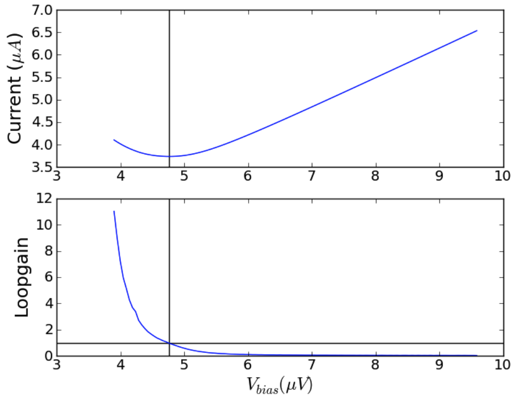

Figure 2.9: Current and loopgain as a function of voltage bias for a TES going into its transition.

2.2.3 Digital frequency domain multiplexer transfer functions and SNR

To understand the transfer functions of various physical signals and noise terms, we present here a discussion of the digital frequency domain multiplexer and how modulated currents are output by the system. We closely follow the notation and derivations found in [105] to outline the functionality of the digital frequency domain multiplexer (dfMux) demodulator. Each AC voltage bias, or carrier signal on a comb of bolometers is of the form shown in Equation 2.4.

Input signals to the demodulator take the form

$$x(t) = s(t)\cos(\omega t + \theta) + n(t) \tag{2.13}$$

where sky signal appears in the modulated current through the bolometers $s(t)$ and $n(t)$ is a noise current term. The demodulator functions simply by mixing the input $x(t)$ against a reference signal $c(t) = A_c \cos\omega_c t$ at the carrier frequency ω_c resulting in the mixer output

$$\begin{aligned} y(t) &= x(t)c(t) = A_c\left[s(t)\cos(\omega t+\theta)+n(t)\right]\cos(\omega_c t) \\ &\approx \frac{A_c}{2}s(t)\left[\cos\left[(\omega-\omega_c)t\right]\cos\theta-\sin\left[(\omega-\omega_c)t\right]\sin\theta\right] \\ &\quad +A_c n(t)\cos(\omega_c t) \end{aligned} \tag{2.14}$$

We've dropped the terms in the final line of Equation 2.14 at frequencies $\pm(\omega+\omega_c)$ that are removed by low pass filtering the mixer output. Note that we're lumping all current to ADC conversion factors in the mixer normalization A_c.

In the case of a demodulator phase-locked and frequency-locked to its input signal so that $\omega=\omega_c$ and $\theta=0$, and with zero noise, the output is given by

$$y(t)=\frac{A_c}{2}s(t) \tag{2.15}$$

the demodulator can be calibrated using a known input signal of unit amplitude $x(t)=cos(\omega_c t)$. The conversion factor between RMS input amplitude and DC demodulator output in counts is then given by

$$X=\frac{A_c}{\sqrt{2}} \tag{2.16}$$

When phase lock is not achieved, the output is simply attenuated by

$$y(t)=\frac{A_c}{2}s(t)\cos\theta \tag{2.17}$$

For frequencies off from the carrier frequency, the output oscillates at the beat frequency

$$y(t)=\frac{A_c}{2}s(t)\cos\left[(\omega-\omega_c)t\right] \tag{2.18}$$

Noise terms can be broadly divided into two categories: those that are due to modulations of the current through the bolometer caused by power flucuations, and those that are additive terms of the form $n(t)$ in Equation 2.13.

For power fluctuations that modulate the carrier, we can use the responsivity from Equation 2.11 to convert between the variance in power σ_p^2 and the variance in the demodulated output σ_y^2 in units of ADC counts

$$\sigma_y=\frac{X}{V_{RMS}}\sigma_p \tag{2.19}$$

where we've taken the high loopgain limit for the responsivity of Equation 2.11 and are limiting ourselves to considering noise within the band defined by the detector time constant.

The variance resulting in the demodulated ouput from a white current noise term term $n(t)$ can be found by similarly calculating the output of the demodulator,

$$n_y(t) = n(t) A_c \cos(\omega t) \tag{2.20}$$

The result can be found by Fourier transforming and using the convolution theorem with the result

$$\sigma_{BB} = \frac{A_c}{\sqrt{2}} \sigma_n \tag{2.21}$$

where σ_n is the white noise variance.

The total demodulated variance is then just the quadrature sum of these two terms

$$\sigma_{ADC} = \sqrt{(\sigma_{BB})^2 + (\sigma_y)^2} = X \sqrt{\sigma_n^2 + \left(\frac{\sigma_P}{V_{RMS}} \right)^2} \tag{2.22}$$

The response to sky signal returned by the demodulator in ADC counts can be found from Equation 2.11 in the high loopgain limit to be

$$y(t) = -X \frac{\delta P_{opt}}{V_{RMS}} \tag{2.23}$$

The signal-to-noise ratio is given by

$$\mathrm{SNR} = \frac{y(t)}{\sigma_{ADC}} = \frac{\delta P_{opt}}{V_{RMS} \sqrt{\sigma_n^2 + \left(\frac{\sigma_P}{V_{RMS}} \right)^2}} = \frac{\delta P_{opt}}{\mathrm{NEP}} \tag{2.24}$$

where in the last equality, we've substituted the overall noise equivalent power (NEP) for the quadrature sum of the current variances times the voltage bias. The NEP gives the incident power necessary to achieve a signal to noise of 1 in a 1 Hz bandwidth. The NEP is related to the power variance by

$$\int |\mathrm{NEP}|^2 df = \sigma_p^2 \tag{2.25}$$

where the integral is carried out over all frequencies. Note that the equivalence between variances in the time domain and noise equivalent powers can also be made over an explicit bandwidth contributing to the variance. Making this distinction, the NEP can be related to the variance contribution from a given bandwidth. We can also be express the NEP in terms of the noise equivalent counts (NEC) at the demodulated output

$$\mathrm{NEP}^2 = [V_{RMS} \times \sigma_n]^2 + \sigma_P^2 = V_{RMS}^2 \left[\frac{\mathrm{NEC}}{X} \right]^2 \tag{2.26}$$

2.2.4 Detector noise

Detector noise is usually discussed in terms of the NEP defined in the previous section, referred to the detector input. The NEP for bolometric detectors can be broken down into several uncorrelated terms that add in quadrature

$$\begin{aligned}\mathrm{NEP}^2 &= \mathrm{NEP}_\gamma^2 + \mathrm{NEP}_G^2 + \mathrm{NEP}_{Johnson}^2 \\ &\quad + \mathrm{NEP}_{readout}^2 + \mathrm{NEP}_{excess}^2\end{aligned} \tag{2.27}$$

The first term corresponds to the photon noise due to background loading inherent in any photo-detector. Ideally, the thermal environment for the detectors will be optimized so that the loading is dominated by power from the atmosphere, and so the photon noise is set by the site location. Detectors and readout should be designed so that all other noise terms in Equation 2.27 remain subdominant to this fundamental limit.

The photon noise can be calculated by considering fluctuations in power due to the variance in the number of photons per mode [57]. The result for the case of a single-moded detector with a narrow band is

$$\mathrm{NEP}_\gamma = \sqrt{2h\nu P_{opt} + P_{opt}^2/\Delta\nu} \tag{2.28}$$

where $P_{opt} = \eta P_{source}$ is the power incident on the detector due to optical power from a given source in the system with an efficiency to the detector η. This can be found by summing all contributions from components in the optical path and the sky, each contributing according to Equation 1.49.

The next term in Equation 2.27 is the thermal carrier noise. This noise arises from the fluctuations in power associated with energy fluctuations in the propagation of thermal carriers such as phonons or electrons across the thermal conductance $G \equiv dP/dT$ between the TES at temperature T_c and the thermal bath at T_b [57]. Thermal carrier noise can be calculated by solving for the power fluctuations caused by energy fluctuations of the thermal circuit shown in Figure 2.6. The result is given by

$$\mathrm{NEP}_G = \sqrt{\gamma 4 k_b T^2 G} \tag{2.29}$$

where γ is a factor that accounts for the conductance as a function of temperature across the thermal link. The result is dependent on the index of the link conductivity $k(T) \propto T^n$ [104]

$$\gamma = \frac{n+1}{2n+3}\frac{1-(T_b/T_c)^{2n+3}}{1-(T_b/T_c)^{n+1}} \tag{2.30}$$

The thermal conductance can similarly be found if the link conductivity index is known and is given by

$$G = \frac{dP}{dT} = \frac{(n+1)P_{sat}T_c^n}{T_c^{n+1} - T_b^{n+1}} \tag{2.31}$$

The third term in Equation 2.27 is the Johnson noise. Johnson noise is caused by the thermal motion of electrons in a resistor at a given temperature. We can calculate the NEP due to Johnson noise for any resistor at a temperature T by considering the current noise produced by the resistor as a voltage noise source in a closed circuit loop of total resistance R_{loop}.

$$\mathrm{NEI}_{Johnson} = \frac{1}{R_{loop}}\sqrt{4k_bTR} \tag{2.32}$$

With electrothermal feedback present, it can be shown that the bolometer Johnson noise is suppressed by the loopgain, $\mathcal{L}$ [104], giving us for a TES in the transition at temperature $\sim T_c$

$$\mathrm{NEI}_{Johnson} = \frac{1}{\mathcal{L}}\frac{1}{R_{loop}}\sqrt{4k_bT_cR(T_c)} \tag{2.33}$$

We can then use the responsivity to get the noise equivalent power due to Johnson noise referred to the input of the detector

$$\mathrm{NEP}_{Johnson} = \frac{\mathcal{L}+1}{\mathcal{L}^2}\frac{V_{rms}}{\sqrt{2}}\frac{\sqrt{4k_bT_cR(T_c)}}{R_{loop}} \tag{2.34}$$

The final two terms in Equation 2.27 account for the noise due to the readout and excess noise terms, respectively. Readout noise can be estimated from properties of SQUIDs, room temperature readout components, and various digitization noise contributions. It can also be measured directly either by reading out a resistor with known noise properties, or in the case of our system, looking at demodulation frequencies far from the bolometer comb. The excess noise term generally lumps together all other noise contributions from non-standard sources. For POLARBEAR's detectors, the only excess noise term is due to $1/f$ noise from various drifts in the system.

A summary of these different contributions is shown in table 2.3 for a bolometer and receiver with the POLARBEAR design goals shown in table 2.4.

Often, rather than quote NEPs, experimenters talk about the noise equivalent temperature (NET), which gives the temperature fluctuation around some mean temperature T_{obs} that can be observed by a detector for 1 second with a signal to noise of 1. This is easily calculated from the NEP

$$\mathrm{NET} = \frac{1}{\sqrt{2}}\frac{\mathrm{NEP}}{dP_{opt}/dT_{obs}} \tag{2.35}$$

Table 2.3: Expected noise contributions from dominant noise terms given the example bolometer properties in table 2.4.

Noise component	NEP Contribution ($aW/\sqrt{Hz}$)	NET Contribution (mK $\times\sqrt{s}$)
Photon noise	45	0.33
Phonon noise	30	0.22
Readout noise	32	0.24
Total	63	0.47

Table 2.4: Design goal bolometer properties for operating POLARBEAR in Chile.

Bolometer property	Value
$\eta\Delta\nu$	12 GHz
Dewar load	21 K
Sky temperature	12 K
Optical power P_{opt}	6 pW
Bias power P_b	10 pW
Total operating power P_{tot}	16 pW

where the $\sqrt{2}$ factor comes from converting between a Nyquist sampled frequency domain noise measure to the corresponding time domain measure of variance. We can use Equation 1.49 to solve for dP_{opt}/dT_{obs} for a single-moded detector with a narrow band of response centered at frequency ν_c

$$\frac{dP_{opt}}{dT_{obs}} = k\eta\Delta\nu\beta^2 n_{occ}^2 e^{\beta} \tag{2.36}$$

For the case of $T_{obs} = T_{cmb} = 2.725K$ and an observation center frequency of $v_c = 150\text{GHz}$, this gives

$$\frac{dP}{dT_{cmb}} = 0.576 \times k\eta\Delta\nu \tag{2.37}$$

and the temperature fluctuation on the CMB that can be measured in one second is given by

$$\text{NET}_{cmb} = \frac{\text{NEP}}{0.576\sqrt{2} \times k\eta\Delta\nu} \tag{2.38}$$

In table 2.3, we also give the contributions to the NET given the NEP contributions and $\eta\Delta\nu$ for our design goal bolometer and receiver properties.

2.3 The POLARBEAR receiver

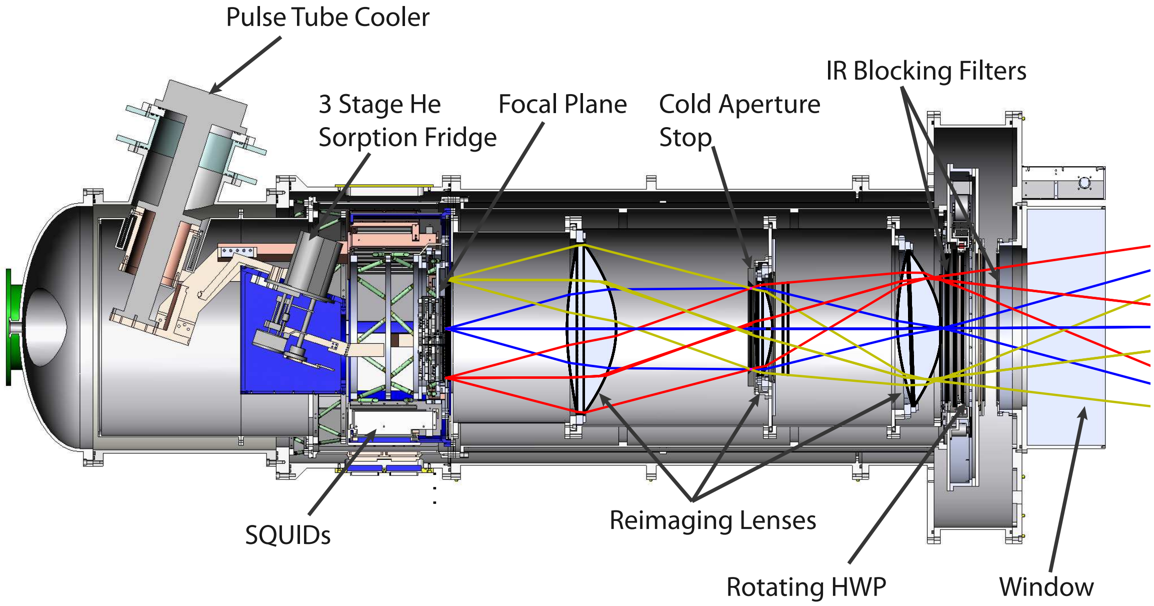

Figure 2.10: A cross-section of the POLARBEAR receiver.

2.3.1 Receiver design goals and challenges

There are several overarching design goals for the POLARBEAR receiver:

- Create a cryogenic environment that allows our focal plane to cool to ~ 0.25 Kelvin with a > 20 hour hold-time.
- Sufficiently cool the receiver and enclosed optical elements to bring the effective dewar temperature referred to the sky below the expected atmosphere temperature in Chile
- Cool the SQUIDs used for the multiplexed readout below their transition temperature to $\sim$6 Kelvin

All of these are effectively requirements to minimize the noise of the instrument. Bringing the focal plane below 0.25 Kelvin makes the thermal carrier noise a subdominant term when compared with expected thermal background loading noise from the Chilean atmosphere. Similarly, to keep the instrument truly background limited, the dewar itself must contribute a subdominant term to the overall thermal background noise when compared to the sky. Cooling the SQUIDs is not only necessary for their functionality, but also to achieve maximum transimpedance and high gain in the multiplexed readout.

The major challenge in achieving these cryogenic goals arises from the size of the receiver required to hold a 19 centimeter focal plane and the necessary cold reimaging optics. An overview of the POLARBEAR receiver is shown in cross-section in Figure 2.10. As can be seen in the figure, the cold reimaging lenses run more than half the length of the receiver. Radiative loads along the entire surface area of the optics tower quickly dominate and surpass reasonable cooling powers if conventional metals are used. Temperature gradients between refrigerator coldheads and optical elements closest to the sky can easily become large enough to cause dominating background loading contributions if care is not taken in selecting materials, designing thermal straps, minimizing loads and creating adequate thermal joints.

Early design choices to duplicate several elements of the receiver from the APEX-SZ experiment further complicated the design. As seen in Figure 2.10, the cryogenic coolers used were placed towards the rear of the receiver, far from the elements such as filters, lenses and squids that have the most stringent temperature requirements. This design choice was driven by the desire to use the midsection of the APEX-SZ receiver where wiring from 300 Kelvin enters the system. Given the complexity of this component of the receiver and how it relates to our readout system, the motivation was to save on both costs and re-design efforts. The tradeoff is that significantly more effort needed to be put into the design of the resulting long thermal straps for both the 4 Kelvin and 50Kelvin stages. Beyond that, the APEX-SZ midsection was chosen before the POLARBEAR focal plane design was finalized. The result was a very compact space to work with to house the large focal plane and accompanying SQUID cryogenic circuitry.

2.3.2 Focal plane structural design

The challenge of fitting the POLARBEAR focal plane and required wiring and cryogenic readout components in the small available space was addressed with a compact focal plane structural support system. We extended the design philosophy to keep all readout elements within the optical element footprint that was employed in the wafer holder design presented in Section 2.2.1. Allowing ease of assembly and maintaining modularity were both important design goals as well.

The extremely compact design also required stringent checks on clearances between wiring and other components at various temperature stages to mitigate the possibility for thermal shorts due to touches. It was decided that the best way to address this requirement was to design a structure that could be fully assembled on the bench, where inspection could be easily carried out. Structural and wiring connections between all thermal stages from the 4 Kelvin mainplate to the milliKelvin

(a) The focal plane assembled up to the 250 milliKelvin stage.

(b) The focal plane assembled up to the 350 milliKelvin stage.

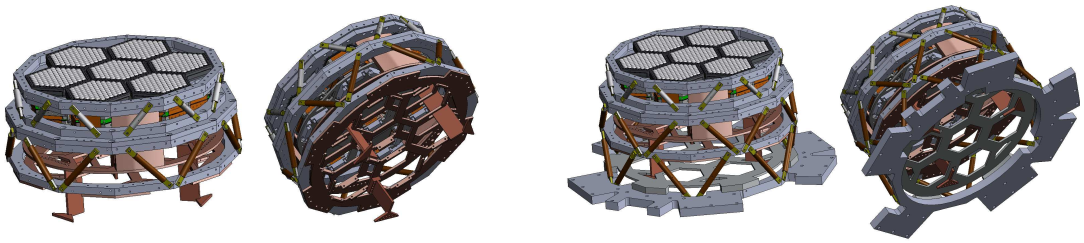

(c) The focal plane assembled up to the heat exchanger stage.

(d) The focal plane assembled up to the 4 Kelvin stage.

Figure 2.11: The focal plane assembly procedure

focal plane would be made before the entire 4 Kelvin focal plane assembly ‘insert’ is installed in the receiver. The steps in assembling the focal plane structure are shown in Figures 2.11(a) - 2.11(d).

Cables at 4 Kelvin are routed from below the focal plane to the perimeter, allowing final connections to SQUID electronics installed in the receiver to be made after the full assembly is installed. Connections to the milliKelvin heat straps also need to be made at this point, which is complicated by the large focal plane, the distance to the milliKelvin coldheads, and their relative inaccessibility. This was addressed by incorporating rigid heat straps attached to the focal plane assembly and flexible straps that remain docked to the 4 Kelvin mainplate until the focal plane insert is installed. The rigid straps for each thermal stage are clearly seen in the assembly procedure outlined in Figures 2.11(a) - 2.11(d). Figure 2.12(c) shows how the docked straps are installed in the 4 Kelvin stage and attached to milliKelvin cold heads below. The docked straps are held in place by dowel pins and a precision machined flat plane surface. After the focal plane insert is installed, as shown in Figure 2.12(d), the rigid straps rest $\sim$ 1/8 inch above the docked straps. Access ports above each of the 3 strap locations at the focal plane allow a custom made tool to be used to engage screws and lift the docked straps off their 4 Kelvin mounts.

Structurally, the design was modeled off a similar design that was made for the

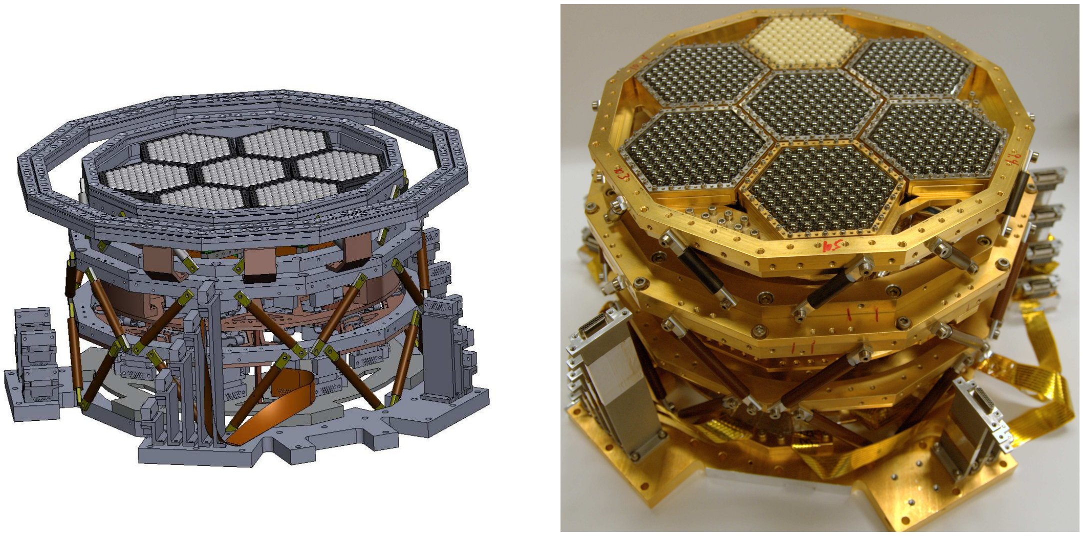

(a) CAD rendering of the focal plane assembly

(b) A photograph of the fully assembled focal plane, support structure and milliKelvin wiring

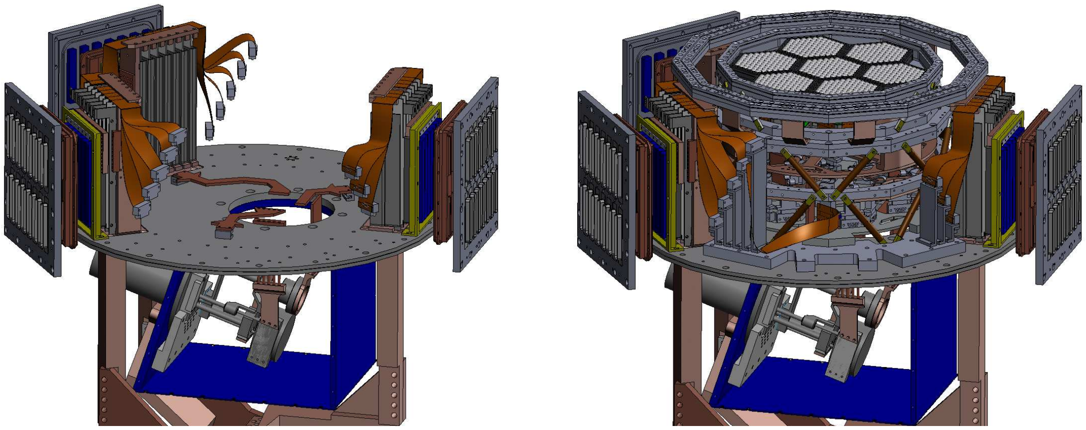

(c) CAD rendering of the midsection with milliKelvin 'docked' straps

(d) CAD rendering of the midsection after the focal plane structure has been installed

Figure 2.12: The fully constructed focal plane assembly and the installation procedure for the mK insert.

focal plane of the APEX-SZ receiver. The structural elements are Vespel[3] SP1 and SP22 tubes arranged in a diagonal truss structure. The tube lengths were chosen at each thermal stage to keep conductive loads below the required level while maintaining adequate structural stiffness. Finite element analysis simulations of the fundamental

---

[3] http://www2.dupont.com/Vespel/en_US/

vibration modes were done to verify the structural stiffness for the APEX-SZ design with a minimum frequency requirement of 100 Hz and these results were verified to be within a factor of ∼2 with room temperature deflection tests. For the POLARBEAR design, while the tube lengths chosen were slightly longer, the number of tubes at each stage was also doubled. For this reason, we began machining and construction of the POLARBEAR focal plane structure without finite element analyses. The resonant frequencies were verified to be high enough with room temperature accelerometer measurements.

2.3.3 Cooling power and thermal loads

Cooling power for the POLARBEAR receiver is provided by two closed cycle refrigerators. Our base temperatures of 50 Kelvin and 4 Kelvin are provided by a pulse tube refrigerator.

Pulse tubes operate by allowing high purity He gas, which is compressed at room temperature, to expand and remove heat from the coldhead similar to a Stirling cooler cycle. A porous regenerator material with high heat capacity allows the temperature gradient between room temperature and the cryogenic coldhead to be maintained. Pulse tubes have the advantages of having no cold moving parts, allowing near continuous operation with little maintenance needed.

A commercial PT415 model from Cryomech, Inc.[4] is used. A photo of the coldhead and a schematic of the pulse tube system is shown in figures 2.13(a) and 2.13(b), respectively. The pulse tube coldhead used actually employs a remote motor to allow electrical and mechanical isolation of the receiver from the valve motor and compressor. The PT415 pulse tube used in the POLARBEAR receiver provides ~ 40 Watts of cooling power at 45 Kelvin on the first stage and ~ 1.5 Watts at 4.2 Kelvin on the 2nd stage. A more detailed measured load curve is shown in Figure 2.13(c).

Subkelvin cooling is provided by a three stage, Helium sorption fridge provided by Chase Research[5]. Cooling power is provided by pumping on condensed 4He and 3He in the various stages using charcoal pumps. Our particular fridge uses a sacrificial 4He cycle which condenses off the 4K stage mainplate to provide a < 1K condensation point for 3He used in the subsequent ‘Ultrahead’ and ‘Interhead’ stages. The interhead stage simply acts as a buffer to intercept thermal loads from wiring and structural members, allowing the Ultrahead to reach ~ 0.25K. A schematic and photo of our Helium sorption fridge is shown in Figure 2.14. The manual provided by Chase Research states that hold times of at least 24 hours are possible with loads of 80 μW on the interhead and up to 4 μW on the ultrahead giving operating temperatures of 375 mK and 250 mK, respectively. Additional cooling power is also available at the heat exchanger, with ~ 100 μW at an equilibrium temperature of ~ 1.5K.

---

[4] `http://www.cryomech.com/`

[5] `http://www.chasecryogenics.com/`

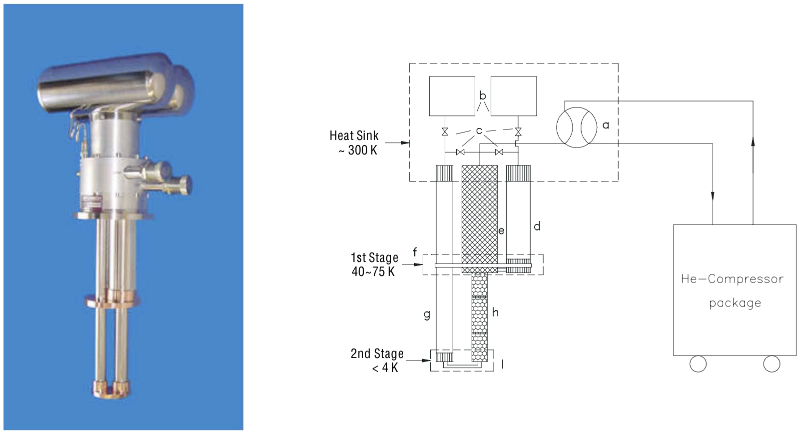

(a) A cryomech pulse tube cooler.

(b) A schematic of a pulse tube cooler system.

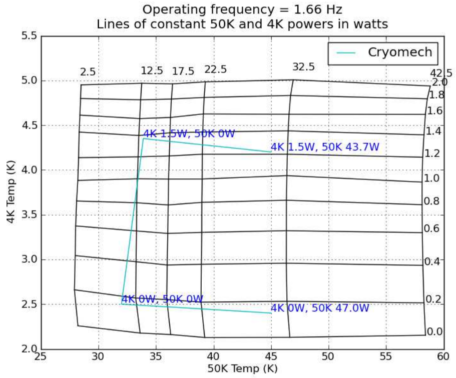

(c) Load curve for the POLARBEAR PT415. The curve provided by cryomech is shown along with the measured load curve with the pulse frequency re-optimized to 1.66Hz from the factor default 1.4Hz

Figure 2.13: Cryomech pulse tube cooler system.

Dominant sources of load on the 50 Kelvin and 4 Kelvin stages include conductive loading from structural supports, wiring, and RF shielding as well as radiative load from the 300 Kelvin vaccum shell on 50 Kelvin and the 50 Kelvin radiative shield onto the 4 Kelvin optics tower.

Contributions from conductive loads can be estimated using available data on thermal conductivity, $k(T)$, for the materials used. Using the equation for one di-

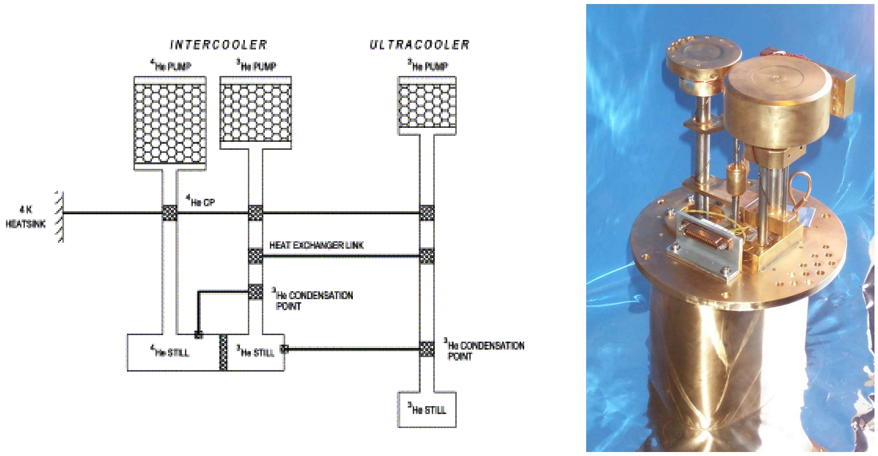

(a) A schematic of a 3 stage 'He10' fridge similar to ours from [106].

(b) A photograph of the Berkeley 'He10' fridge made by Chase Research Cryogenics.

Figure 2.14: The Chase Research 'He10' 3 stage Helium soprtion fridge.

Component	$A\int k(T)dT$ (W·in)	l (in)	Contribution (W)
G10 300K-45K	1.68	0.59	2.8
G10 45K-4K	.093	2	.046

Table 2.5: Load contributions from G10 supports on the two PTC stages.

mensional heat conduction, the load $\dot{Q}$ can be found

$$\dot{Q} = \frac{A}{l}\int_{T_1}^{T_2} k(T)dT \tag{2.39}$$

where A/l is the ratio of the cross-sectional area to the length of the conducting element. Conductivites for materials used in the POLARBEAR receiver are shown in figures 2.15(a) and 2.15(b) in both the milliKelvin and $> 1K$ temperature ranges.

For the 50K and 4K stages, a G10 rod drum structure was used to support and isolate the coldplates in the receiver. This design was duplicated from the APEX-SZ receiver design. The structures consist of 20 tubes with a 1/4 inch OD and 3/16 inch ID and appropriate lengths to keep loading minimal while providing enough stiffness. Fits from [109] for the thermal conductivity of G10 were used to calculate the loads, summarized in table 2.5.

Wiring from room temperature to 4 K consists of 18 twisted pairs of 4 mil manganin wire in Nomex weaves supplied by TekData. These weaves are specified by

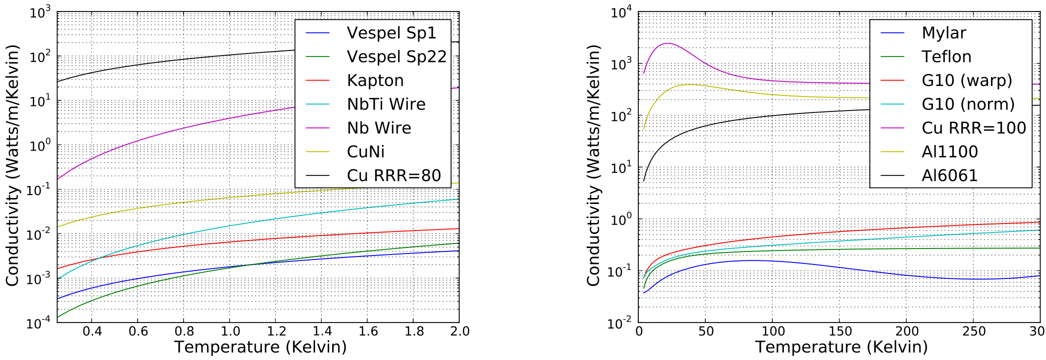

(a) Conductivities in the milliKelvin range.

(b) Conductivities in the 300K - 1 K temperature range.

Figure 2.15: Conductivities of materials used in the POLARBEAR receiver. From [107, 108, 109, 110, 111]

Tekdata to contribute a load of 70 mW for a 2 cm length between 300 K and 50 K and a load of 2 mW for a 5cm length between 50 K and 4 K. Each SQUID wiring module in our system has 14 weaves of lengths 1.25 inches and 2.4 inches for 50 K and 4 K, respectively, giving the expected contributions shown in table 2.6. There is also a housekeeping module with six weaves of lengths 1.8 inches and 2.8 inches to the 50 K and 4 K stages. The expected contribution from the housekeeping module is also shown in table 2.6.

Below spec field experience with the wiring modules in both APEX-SZ and SPT led us to attempt to verify their performance. Measurements of the conductivity of the weaves using a wet dewar at a variety of temperatures were carried out by Bryan Steinbach. His results are shown in tables 2.7 and 2.8. The first stage loading is about 50% larger than expectations but the second stage loading is to spec. One thing to note is that these measurements were done in a 4 Kelvin environment and the weave can actually see 50 Kelvin and 300 Kelvin in their actual application.

Component	$A\int k(T)dT$ (W·in)	L (in)	Contribution (W)
SQUID Module 300K-50K	0.8	1.25	0.64
SQUID Module 50K-4K	0.06	2.4	0.025
Housekeeping Module 300K-50K	0.34	1.8	0.19
Housekeeping Module 50K-4K	.026	2.8	0.009

Table 2.6: TekData specified load contributions from wiring on the two PTC stages.

Temperature (K)	$A\int_{4.2}^{T} k(T')dT'$ (W·in)	Contribution in SQUID module (W)
50	0.06	0.025
60	0.08	0.035
70	0.11	0.047
75	0.13	0.054
80	0.15	0.062
90	0.19	0.079

Table 2.7: Measured conductivity of wire harnesses, presented as conductivity per wire harness with $l = 2.4$ inches for second stage

These measurements therefore provide an upper limit for the conductivity since more power is necessary to achieve the same gradient if the absorptive weave comes into equilibrium with 4K rather than 50K radiation. However the load contribution from the wire harness due to radiation being absorbed on the nomex weave is not explicitly taken into account here, and its possible that this contribution can be substantial.

Temperature (K)	$A\int_{77.3}^{T} k(T')dT'$ (W·in)	Contribution in SQUID module (W)
90	0.07	0.06
115	0.22	0.18
140	0.4	0.32
165	0.58	0.47
190	0.77	0.61
215	0.93	0.75
240	1.06	0.85
265	1.17	0.93
280	1.2	0.96

Table 2.8: Measured conductivity of weave presented as conductivity per wire harness with $l = 1.25$ inches for first stage

These measurements along with both finite element modeling and measurements of gradients along the wiring intercepts allowed us to conclude that the discrepancies seen by earlier experiments were due to inadequate heat sinking to the 50 Kelvin stages. The original design, borrowed from the APEX-SZ receiver, used slats and frames made from the 6061 aluminum alloy to intercept the wire weaves. This alloy has relatively poor thermal conductivity and thermal gradients from the radiation shield to the intercept points were found to be on the order of 10 Kelvin. Beyond that, the intercept length along the wires was not sufficient to provide a proper

Component	$A\int k(T)dT$ (W·in)	L (in)	Contribution (W)
SQUID Module 300K-75K	1.2	1.25	0.96
SQUID Module 75K-4K	0.13	2.4	0.054
Housekeeping Module 300K-75K	0.51	1.8	0.28
Housekeeping Module 75K-4K	0.056	2.8	0.02

Table 2.9: Expected contributions from wire harnesses given measured weave conductivities.

thermal sink. This was addressed by replacing the aluminum parts with OFHC copper ones and by increasing the intercept length by a factor of 3. Lab measurements of the new wire harnesses found that the performance matched expectations given the weave conductivity measurements in tables 2.7 and 2.8. The total conductive loading contribution from the wiring modules is summarized in table 2.9.

Radiative loads on the 50K shields were a cryogenic challenge for the POLARBEAR receiver. Radiative loads between any two surfaces can be found by using the Stefan-Boltzman law, which gives the power radiated by a surface with emissivity ϵ area A and temperature T as

$$\dot{Q} = \sigma \epsilon A T^4 \tag{2.40}$$

For any two gray, diffuse surfaces with emissivities ϵ_1, ϵ_2 at temperatures T_1, T_2 the amount of radiant energy emitted by one surface and seen by the other must be taken into account. The result, which can be found in any textbook on radiant energy transfer (i.e. [112, 113]) is

$$\dot{Q} = \frac{\sigma\left(T_1^4 - T_2^4\right)}{(1-\epsilon_1)/\epsilon_1 A_1 + (1/A_1 F_{12}) + (1-\epsilon_2)/\epsilon_2 A_2} \tag{2.41}$$

where F_{12} is known as the configuration or view factor and gives the fraction of radiant energy from surface 1 that is seen by surface 2. Viewing factors can be calculated by integrating over solid angle and surface area, giving

$$F_{12} = \frac{1}{A_1}\int_{A_1}\int_{\Omega_1} \frac{\cos\theta_1}{\pi} d\Omega_1 dA_1 = \frac{1}{A_1}\int_{A_1}\int_{A_2} \frac{\cos\theta_1\cos\theta_2}{\pi S^2} dA_1 dA_2 \tag{2.42}$$

where we've used the definition of the differential solid angle subtended by area element dA_2 a distance S away

$$d\Omega_1 = \frac{dA_2 \cos\theta_2}{S^2} \tag{2.43}$$

Geometry	Viewing Factor	Radiative load
Two large concentric cylinders	$F_{12} = 1$	$\dot{Q} = \frac{A_1\sigma(T_1^4 - T_2^4)}{1/\epsilon_1 + (A_1/A_2)(1/\epsilon_2 - 1)}$
Two large parallel plates of equal area	$F_{12} = 1$	$\dot{Q} = \frac{A\sigma(T_1^4 - T_2^4)}{1/\epsilon_1 + 1/\epsilon_2 - 1}$

Table 2.10: View factors and radiative loads from relevant geometries

Viewing factors and resulting radiant loads for several geometries that are useful to consider for a cryostat like the POLARBEAR are summarized in table 2.10

A summary of the 50 Kelvin stage shield areas is shown in table 2.11. Using only polished aluminum for all cold surfaces with an emissivity of 0.1 as shown in table 2.12 would result in a radiative load contribution of about 100 Watts, exceeding the thermal budget of our pulse tube.

Shield section	Area (m^2)	MLI effective flux (W/m^2)	Load contribution (W)
Cryogenics end shields	0.64	6	4
Midsection shield	0.42	18	7.6
Optics shell	1.34	6	8
HWP enclosure	0.48	7	3.4
Total	2.88	7.99	23

Table 2.11: Areas, MLI effective heat flux and load contributions from different sections of the cryostat

Multilayer insulation (MLI) provides a way to mitigate these excessive thermal loads by inserting many quasi-isolated radiation shields in between the two temperatures. In the ideal, fully isolated case, the load would drop proportionally with the number of layers added. In practice, there is some non-negligible conduction between the different layers in a blanket that is highly dependent on the assembly procedure and the resulting blanket contact pressure, interstitial vacuum pressure and materials used.

A more thorough discussion of MLI is presented in Section 2.3.4. We present here the resulting performance for MLI blankets used in the POLARBEAR receiver. Blankets were both made in the lab and purchased from commercial vendors [6] with varying results. Total effective intensities and loads are presented in table 2.11.

---

[6] The optics shell blanket was purchased from Aerospace Fabrication, LLC `http://www.aerospacefab.com`

Material	Emissivity at 77K	Emissivity at 4K
Aluminum As Found	0.12	
Aluminum Anodized	0.8	0.75
Aluminum Oxidized	0.49	0.074
Aluminum Mechanically Polished	0.1	0.058
Aluminum Electropolished	0.75	0.36
Copper As Found	0.12	0.062
Copper Mechanically Polished	0.06	0.023
Copper Electropolished	0.35	

Table 2.12: Emissivities of common metals used in cryostats at 77 Kelvin and 4 Kelvin from [112].

RF shielding of the bolometers and SQUIDS in the cryogenic space is provided by creating a continuous Faraday cage to the 300 Kelvin vacuum shell. This is accomplished using sheets of aluminized Mylar. Both the deposited aluminum and the mylar substrate contribute to the thermal loading on the 50 Kelvin and 4 Kelvin stages.

For the subkelvin stages, we used Vespel SP1 and SP22 for structural support and thermal isolation between 4K and 0.35K and 0.35K and 0.25K, respectively. SP22 is used at the lower temperatures since it has a lower conductivity in that temperature range, as seen in Figure 2.15(a).

Tubes with a thickness of 30 mils and an outer diameter of 0.325 inches leading to a cross-sectional area of $A = 1.46 \times 10^{-2}$ in^2 were used for all stages. We used 12 tubes at each stage, giving the load contributions summarized in table 2.13.

Stage	$A \int k(T)dT$ (W $\cdot$ in)	l (in)	Loads (W)
Hex	5.01e-06	1.875	3.21e-05
IC	2.89e-06	1.50	2.32e-05
UC	1.20e-08	0.50	2.88e-07

Table 2.13: Summary of loads from structural supports on milliKelvin stages.

Wiring between the SQUIDs at ~ 4 Kelvin and the milliKelvin stages is provided by copper striplines and a Niobium Titanium twisted pair cable. The superconducting NbTi cable provides a thermal break between the various stages. The twisted pair wires each have a cross-sectional area of $A = 1.2 \times 10^{-5}$ in^2 of NbTi and a 6 micron CuNi cladding with a cross-sectional area of $A = 2.95 \times 10^{-6}$ in^2. Calculations of the expected loads were done assuming 21 conductors per pigtail and assuming the nomex weave of the pigtail is thermally equivalent to another conductor. The total loads would then be due to $22 \times 21 = 462$ conductors. Loads due to the wiring are summarized in table 2.14.

Stage	$A\int k(T)dT$ (W · in)	l (in)	Loads (W)
UC	7.98e-08	0.75	1.06e-07
IC	2.52e-05	2.5	1.0e-05
Hex	5.59e-05	1.0	5.59e-05

Table 2.14: Summary of loads from wiring on milliKelvin stages. The integrated conductivity includes a contribution from a copper cladding.

Again, aluminized mylar completing the Faraday cage from 4 Kelvin to the millikelvin stages contibutes to the loading and must be taken into account.

Contributions to the total loads on all stages from all of these sources are summarized in table 2.15. Note that we are well within our cooling power budget given the capacity of our pulse tube cooler and Helium sorption fridge.

Table 2.15: Total load summary on all stages

Component	50K	4K	Hex	IC	UC
Structural support	2.8 W	0.046 W	3.2e-5	2.32e-5	2.88e-8
Wiring	3.2 W	0.182 W	5.59e-5	1.0e-5	1.06e-7
RF shielding	1.2 W	0.2 W	–	1.15e-5	3.57-8
Radiative	23 W	0.2 W	–	–	–
Total	30.2 W	0.628 W	8.79e-5	4.47e-5	1.71e-7

2.3.4 Multilayer insulation

Modeling multilayer insulation is a difficult task since performance is highly dependent on factors like contact pressure and interstitial gas pressure. Since every installation is unique and requires different edge treatments, blanket penetrations, etc., performance is almost always significantly worse than modeled. Many empirical models based on measurements of MLI blankets have been made by the aerospace industry for the purposes of better modeling of insulation of rocket fuel tanks.

Most models break down the total load contribution into contributions from an effective radiative contribution, gas conduction through the residual gas between layers, and conduction along the insulator used to space layers. A good summary of multiple models is presented in [114]. For illustrative purposes, we will use a frequently referenced model known as the Keller model [115], developed by researchers at Lockheed. In this model, the radiative contribution is given by

$$\dot{Q}/A = \frac{C_r \epsilon}{N_l}\left(T_h^{4.67} - T_c^{4.67}\right) \tag{2.44}$$

and that from conduction along the insulating material by

$$\dot{Q}/A = \frac{C_s \bar{N_l}^{n_s} T_m}{N_l + 1} (T_h - T_c) \tag{2.45}$$

where N_l is the number of layers, $\bar{N_l}$ is the layer density in layers per centimeter, $T_m = (T_h - T_c)/2$ the mean temperature, ϵ the individual layer emissivity, and C_s, C_r, n_s are all dependent on the materials used and fit from experimental data. Fits from various configurations presented in [115] are summarized in table 2.16 with units such that heat flux results are in Watts per meter squared.

MLI type	C_r	C_s	n_s
Unperforated DAM, Tissuglass	8.03×10^{-11}	4.43×10^{-11}	3.91
Unperforated DAM 'preconditioned' silk net	5.39×10^{-11}	8.95×10^{-8}	2.56
Unperforated DAM as received silk net	5.39×10^{-11}	2.11×10^{-9}	3.56
Perforated (pattern S-604) DAM preconditioned silk net	7.07×10^{-10}	7.30×10^{-8}	2.63

Table 2.16: Parameters for the conduction and radiative terms of the Keller model [115] for various MLI blanket constructions. Units are such that resulting heat fluxes are in W/m^2

The contribution due to conduction via interstitial gas was often ignored in many studies of near-ideal blanket construction where tests are done on simple, flat stack blankets, and the gas pressure within the blanket layers can easily approach the pressure in the vacuum vessel. Studies found that in practical applications with blankets wrapped around cylinders and other, more complex assemblies, the interstitial gas pressure can actually be many orders of magnitude larger than the pressure in the vacuum vessel [116, 115] and that conduction via gas can therefore easily be a dominant contributor to the load. The Keller model again provided an empirical prediction of the form

$$\dot{Q}/A = \frac{C_g p_{ins} \left(T_h^{m+1} - T_c^{m+1}\right)}{N_l} \tag{2.46}$$

where p_{ins} is the interstitial gas pressure, and C_p and m depend on the residual gases in the system and outgassing properties of MLI components. Fits from [115] for He and N_2 residual gas are shown in table 2.17.

Gas	C_g	m
He	4.89×10^4	-0.74
N_2	1.46×10^4	-0.48

Table 2.17: Parameters for gas conduction terms in the Keller model [115] for both residual He and N_2 gases. Units are such that resulting heat fluxes are in W/m^2

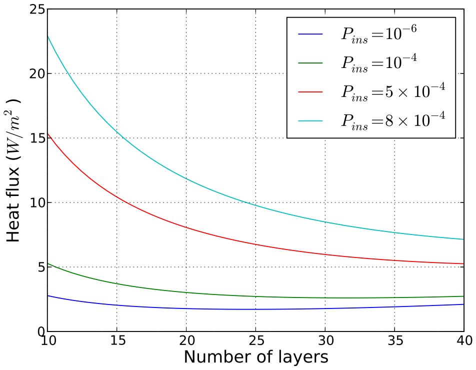

Figure 2.16: Heat flux as a function of the number of MLI layers for several interstitial pressures.

We can add all three contributions with estimates for our blanket layer density, surface emissivity, and interstitial gas pressure to get an estimate for the radiative load contribution. Figure 2.16 shows the radiative loads for several interstitial pressures. Most of our blanket performances of ∼6 Watts/meter^2 for 30 layers as summarized in table 2.11 can be explained by interstitial pressures on order of $\sim 6 \times 10^{-4}$ Torr. This would not be a surprising value since the vacuum of the vessel is only $\sim 1 \times 10^{-5}$ Torr as read out at the optics end vacuum gauge.

The abnormally high flux seen by the midsection shields can be due to many things. The midsection blanket was made of Cryolam, an aluminized mylar with a fiberglass-like backing as the insulating element. This is known to have poorer performance when compared to the double aluminized mylar (DAM) and Dacron netting used in later blankets we developed in lab and purchased from outside vendors. Also, this blanket was wrapped relatively tight in comparison to the other blankets and rolled continuously so that conduction along the blanket itself limits performance more than if layers were physically separated. A large fraction of the area is also exposed to allow the SQUID wiring harnesses to penetrate, which could also exacerbate edge effects that reduce effectiveness of the MLI.

2.3.5 Thermal filtering

Limiting the radiative loads between cryogenic stages along the optical chain is another engineering challenge. For POLARBEAR's $\sim$ 30 cm window without any filtering in place, radiative loading from the 300 Kelvin world outside the vacuum space would add $\sim$ 30 Watts of loading onto the 50 Kelvin stage. The zotefoam used to provide a low-loss vacuum window actually improves upon this since its relatively poor conductivity leads to a reduced temperature of the vacuum side of the window through radiative cooling. The resulting window temperature of $\sim$ 150 Kelvin, gives only $\sim$ 2 Watts of loading. While we have enough margin on the 50 Kelvin stages to deal with this load, this quickly becomes an issue for radiative loading on subsequent cryogenic stages and for contributions to the dewar load.

The majority of CMB experiments designed in the past decade have used filters designed by the Cardiff group to solve this problem. These filters use metal structures deposited on substrates to create high and low pass resonant filters [117]. Inductive grid patterns are used for high pass filters, and capacitive grids for low pass. The patterns can also be combined to form band pass filters. Multiple grids are generally stacked together to create higher-order filters with sharper frequency cut-off features. Structures are deposited on dielectrics such as polypropylene and mylar and have been made both as air-gap filters, spaced using metal rings, or as hot-pressed filters spaced with dielectrics such as polypropylene that can be fused together.

The current generation of filters produced by the Cardiff group have been hot-pressed filters and are commonly referred to as 'metal-mesh' filters. These are favored both for their increased robustness compared to the delicate air-gap filters, and for lower absorption above 30 cm^{-1} of the polypropylene substrate used for hot press filters compared to the mylar substrate used in air gap filters. Polypropylene is a difficult substrate to use in air gap filters due to the requirements for vacuum annealing, but it is an ideal material for a hot-pressed style filter [117].

Figure 2.17 shows the configuration of filters used in the POLARBEAR receiver. The 12 icm filter is attached to the 50 Kelvin stage to reject shorter wavelength radiation from loading the 4 Kelvin stage. The 15 icm filter is attached at the entrance to the 4K optics tube to help reject harmonics that leak through the 50 Kelvin 12 icm filter and provide further rejection of shorter wavelengths heating the cryogenic stages and heating optical elements such as lenses. Finally, the 8.7 icm filter is placed at the aperture stop skyward of the aperture lens. Spectra for the metal mesh filters used in the POLARBEAR receiver are shown in Figure 2.18(a).

Early work on integrating the POLARBEAR receiver quickly found issues with the standard Cardiff filter stacks being used. The polypropylene substrate used for metal mesh filters has high absorptivity in the 5 - 20 μm spectral region, corresponding to temperatures between 70 and 300 Kelvin. Without strong rejection of this radiation using optical elements in front of the metal-mesh filter, power is absorbed and large gradients develop along the metal mesh filters due to the poor thermal conductivity of

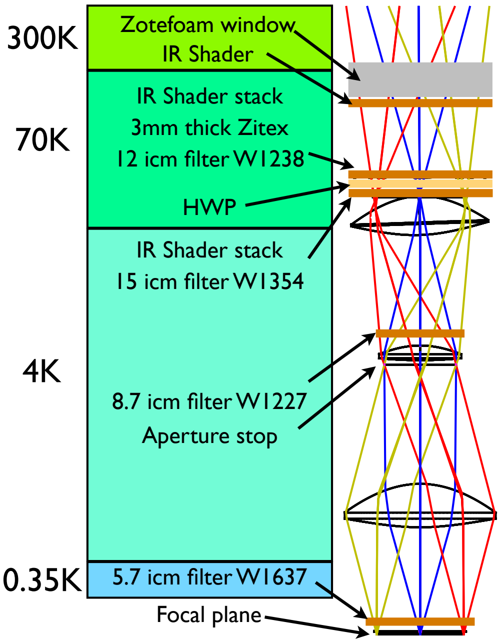

Figure 2.17: The final configuration of filters used in the POLARBEAR receiver. See the discussion in the text for details on the IR shaders used and the need for the Zitex porous teflon filter.

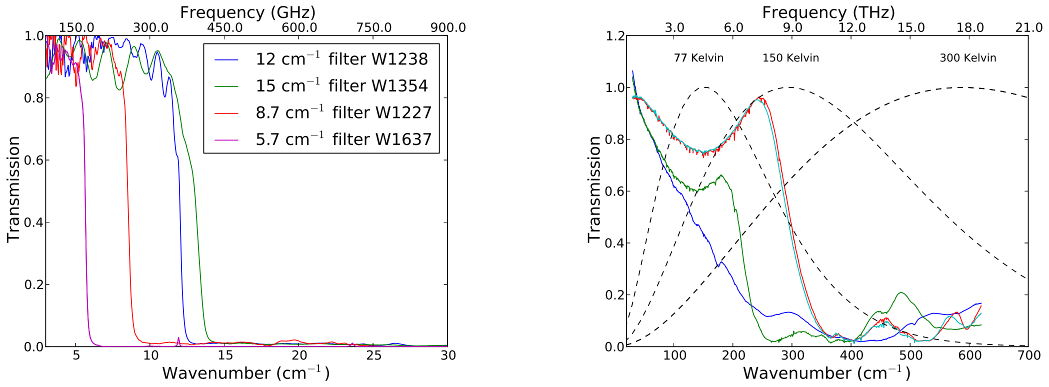

(a) Spectra for the metal mesh filters used in POLARBEAR.

(b) Sample IR shader spectra shown with the blackbody curves for several sample temperatures (all normalized to 1) for reference.

Figure 2.18: Filter spectra for metal mesh (a) and IR shader (b) filters used in POLARBEAR.

the polypropylene. The high emissivity of polypropylene in this same spectral region results in the hot filter reemitting and causing high thermal loads on subsequent cryogenic stages. The hot filter also dominates the resulting dewar load. Efforts were made to address these issues by the Cardiff group by using filters with thin, low absorption substrates and low pass filter metal structures deposited [118], referred to as IR shaders. Examples of IR shader spectra can be found in Figure 2.18(b). The original filter stack had one such IR shader in front of each metal mesh filter. This was insufficient to achieve the required cryogenic environment. As seen in table 2.18, a single IR shader still allowed the metal mesh filter attached to the 50 Kelvin radiation shield to have an 88 Kelvin gradient from its edge to center. As we'll discuss shortly in Section 2.3.6, thermal gradients along the 50 Kelvin radiative shields allow the filter edge to be thermally sunk to only ∼ 80 Kelvin. This would result in the filter center at a temperature nearly in equilibrium with the zotefoam window, providing highly ineffective filtering.

Filter configuration skyward of metal-mesh filter	ΔT from filter center to edge
1 IR shader	88 K
1 IR shader and 4 layers of thin mupor	78 K
1 IR shader, 4 layers of thin zitex, 1 thick mupor sheet	27 K
5 IR shaders, 1 thick mupor sheet	28K

Table 2.18: Several IR filtering configurations were used. We present here the resulting gradient from the filter center to edge.

This was addressed in POLARBEAR with the addition of a 3mm thick sheet of porous teflon[7]. Porous teflon with a 5-10 micron pore size proves to be a very effective IR blocker since it has high transmission in the millimeter range and strong rejection of wavelengths shorter than 100 μm due mostly to scattering off the teflon spheres that are sintered together to make the porous material [119]. Since the IR rejection is dominated by scattering rather than absorption and the millimeter absorption and emissivity of teflon are low, the contribution of porous teflon filters to the dewar loading is very small compared to that due to metal mesh filters.

As shown in table 2.18, the addition of a single 3mm thick layer of Mupor significantly reduced the gradient along the 50 Kelvin metal-mesh filter to less than 30 Kelvin. The addition of 4 new Cardiff IR shaders in the final configuration used for Cedar Flat did not improve the cryogenic environment beyond that achieved with the single Mupor sheet.

---

[7] The porous teflon used goes by the brand name of Mupor (`http://www.interstatesp.com/mupor_standard_sizes.html` and size PM1030 was selected to be similar to the commercial product Zitex G, a material that has been well characterized in the millimeter and infrared range but is no longer available.

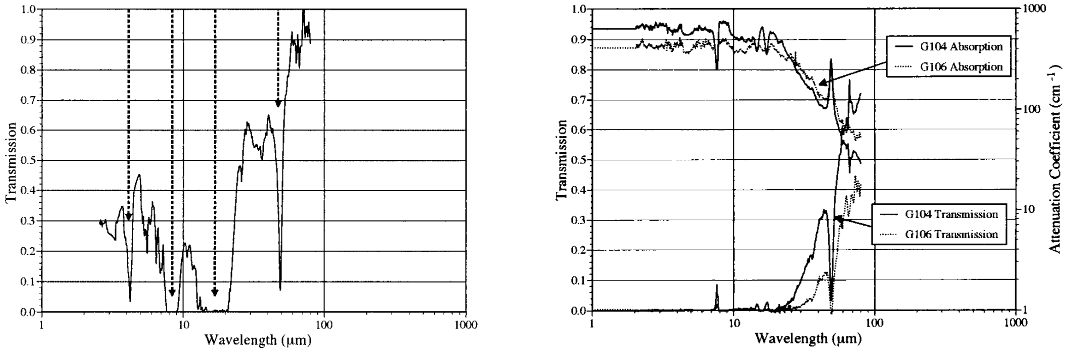

(a) Bulk teflon transmission

(b) Transmission of porous teflon (Zitex G104 and 106).

Figure 2.19: Transmission of bulk and porous teflon. Figures from [119].

2.3.6 Mitigating thermal gradients

Thermal gradients along receiver elements conducting nominal loads can still cause cryogenic issues if care is not taken in designing heat straps, selecting materials and properly intercepting loads. For example, even after significant effort was put into mitigating the radiative load from 300 Kelvin onto the 50 Kelvin shells using multi-layer insulation, the resulting gradient from the ∼12 Watts along an AL6061 optics tube would be ∼30 Kelvin. This would only provide a ∼100 Kelvin cold surface for the metal-mesh filters to be clamped to. Even with adequate thermal filtering skyward of the 50K metal mesh filters as described in the previous section, the resulting average filter temperature would be too warm and contribute to excessive cryogenic loads on 4 Kelvin and subsequent stages.

To mitigate the thermal gradient along the 50 Kelvin optics shell, we designed a dual-shell system. This design was motivated by those of liquid cryogen-based receivers, where the cold gas boiling off from the liquid cryogen is used to cool an independent radiative shield. This results in a radiative environment that is significantly colder than that presented by the 300 Kelvin vacuum shell directly, and a dramatically reduced load.

In the case of our cryogen-free receiver, a similar advantage is provided by allowing an outer shell, attached at the same cold point as the inner shell, to intercept the 300 Kelvin radiative load. We used a thinner, light-weight AL6061 shell for the outer shell. Given the ∼12 Watts of loading from 300 Kelvin, a substantial gradient will develop across this outer shell, warming it to ∼180 Kelvin at the warm end compared to the ∼70 Kelvin cold end in the POLARBEAR receiver. Despite this remaining gradient, there is a dramatic reduction in the radiative load on the inner shell given the T^4

scaling of the incident load. This results in a < 5 Kelvin gradient between the cold and warm ends of the inner shell, providing a colder attachment point for metal mesh filters and the HWP and a lower radiative load on the subsequent 4 Kelvin stage.

Thermal gradients also needed to be addressed to help cool the SQUID readout cards. While the improvements made to the wiring intercepts described in Section 2.3.3 dramatically reduced the loading on 4K, the temperatures on the SQUID cards remained marginal since the majority of the load was still introduced at either warmer points in the receiver along the optics tube or at the wiring from 50 Kelvin. With the 4 Kelvin pulse tube coldhead a significant distance away from the SQUID cards, this was addressed by adding separate heat straps to cool each of the 3 SQUID card banks separately from the main heat strap that attaches to the Simon Chase 4K condensation point and also carries the load from the optics tower. These heat straps were annealed by heating to ~900°C to repair lattice defects. The resulting RRR improved by a factor of ~ 3 over the bulk OFHC copper RRR of ~ 100. It should be noted that a greater improvement of RRR is possible by oxygen annealing [120]. This can result in RRRs as high as several thousand. An appropriate vacuum oven was not found to carry out such annealing for these larger straps and the higher RRR was not necessary for this particular application.

Similarly, heat straps were designed to help mitigate the gradient along the distance between the 50 Kelvin coldhead and the 50 Kelvin plate. For these heat straps, annealing was not required as the conductivity in the 50 Kelvin temperature regime does not show a strong dependence on RRR [109, 121].

With properly engineered heat straps, the dominant component of the thermal gradient between a coldhead and elements in the receiver can become the strap interfaces. There is much research into optimizing heat strap interfaces at various temperatures and not always agreement between different parties. For several references see [122, 123, 124, 125, 126]. We followed the following practices for our interfaces:

- **Sub Kelvin:** Surfaces were machined to 32 micro-inch precision. If possible, parts were gold plated with soft Type III gold. For parts that were not gold plated, nitric acid was used to clean the copper oxide just before installation. No greases were used and brass screws were used with copper parts to assure high pressure joints when cold.

- **4 Kelvin:** Surfaces were machined to 32 mico-inch precision. If possible, parts were gold plated with soft Type III gold. For parts that were not gold plated, nitric acid was used to clean the copper oxide just before installation. A thin layer of Apiezon N grease was used as a gap filler. For copper parts, brass screws were used unless the screw size was small enough that we were concerned the desired torque on the screw would break it. In these cases, and when aluminum parts were used, we employed stainless steel screws with appropriate Belleville washers to compensate for differential thermal contraction.

- **50 Kelvin:** The same practices used for 4 Kelvin components were used for 50 Kelvin components.

2.3.7 Cryogenic performance

The results from several relevant runs are shown in tables 2.19 and 2.20, with temperature locations indicated in figures 2.20(a) and 2.20(b). CF1 is the engineering run carried out at the Cedar Flat site in California, PCF7 the final test run in the lab with the fully configured receiver before the Chilean deployment, and CH1 the first cooldown in Chile. An important distinction between the CF1 run and the PCF7 and CH1 runs is that the CF1 run used only one of the three possible wire harnesses. The addition of the other two wire harnesses to accommodate the full focal plane readout changed the 4 Kelvin loading substantially and required significant modifications to be made. The end result of several improvements to the 4 Kelvin heat straps was better overall performance during the final CH1 run compared to the CF1 run, despite the larger load. Both CF1 and CH1 showed improved performance over similarly configured lab runs. We believe that this is mostly due to colder ambient temperatures of the vacuum shells, though some improvements might be attributed to the better vacuums achieved with the drier environments that the receiver was reassembled in. Note that for the CH1 run, a diurnal variation of ~ 2 Kelvin was seen on the 50 Kelvin stages due to the more extreme ambient temperature changes at the site. In the tables, we report the higher temperature of the daily cycle.

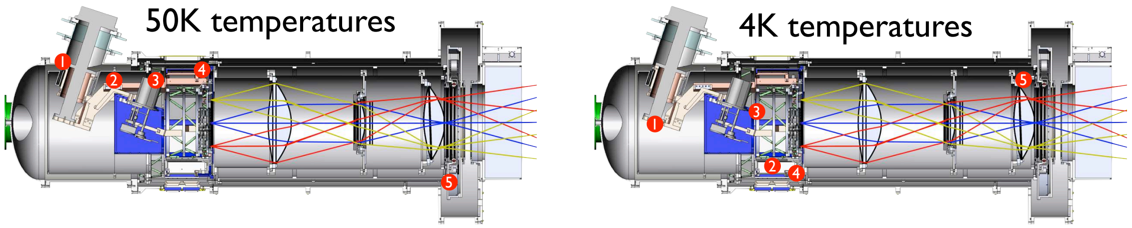

(a) Locations of 50 Kelvin stage temperatures listed in table 2.19.

(b) Locations of 4 Kelvin stage temperatures listed in table 2.20.

Figure 2.20: Locations in the receiver of various temperatures reported in tables 2.19 and 2.20.

The resulting 4 Kelvin and 50 Kelvin temperatures coupled with our thermal filtering allowed us to successfully cycle our Helium sorption fridge and achieve the desired hold times and base temperatures. As shown in Figure 2.21, hold times of > 20 hours were achieved.

Table 2.19: 50 Kelvin stage temperatures for various runs.

Label Number	Description	CH1	PCF7	CF1
1	50K coldhead	40K	46K	45K
2	50K tower strap cold	44K	50K	50K
3	50K tower strap warm	46K	55K	54K
4	50K wire harness	60K	73K	70K
5	HWP baseplate	–	–	88K

Table 2.20: 4 Kelvin stage temperatures for various runs.

Label Number	Description	CH1	PCF7	CF1
1	4K coldhead	3.2K	3.2K	3.2K
2	Squid card	3.6K	3.7K	4.5K
3	4K mainplate	3.7K	4.0K	4.1K
4	Midsection	3.9K	4.3K	5.2K
5	Lens flange	–	–	6.4K

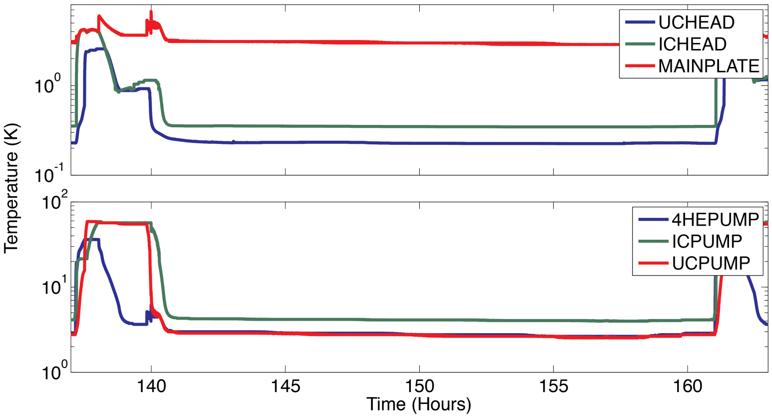

Figure 2.21: An example milliKelvin fridge cycle and resulting settled milliKelvin stage temperatures.

2.4 Systems integration

Several systems have to be integrated for the POLARBEAR experiment to function. There are three main functionalities that are required.

- **Telescope control**: We need to be able to command the telescope to move in azimuth and elevation.

- **Receiver operation**: The 1344 detectors and 168 SQUIDS need to be tuned in an efficient, timely manner. Detectors and readout systems also need to be monitored and tuning parameters adjusted throughout an observation. Control over other receiver subsystems such as cryogenics and HWP motion is also needed and often needs to be coordinated with detector tuning and telescope motion.

- **Data acquisition**: The telescope azimuth and elevation as well as detector timestreams, cryogenic temperatures, and other receiver and telescope housekeeping must be recorded to disk. A method to synchronize these different data products is needed. For the case of synchronizing telescope azimuth and elevation with detector timestreams, this is clearly a necessary step to producing maps of the sky. Other housekeeping timestreams should be synchronized to enable investigations of and corrections to drifts in the detector timestreams.

In this section, we describe the approaches used to address these goals and briefly describe the software packages that have been used.

2.4.1 Telescope control and data acquisition with GCP

An interface was provided by Vertex RSI to command and read out telescope positions as well as collect data from several telescope housekeeping systems. This interface is through the antenna control unit (ACU), which communicates using a command-response protocol over an RS232 serial interface. The general control program (GCP) was originally written for telescope control and data acquisition several decades ago and has since been adapted to function with other experiments and their respective control systems. GCP was modified to work with the South Pole Telescope which was also built by Vertex and uses the same ACU interface. This provided a plug-in solution for the POLARBEAR telescope to achieve telescope control and data acquisition of the various telescope systems read out by the ACU.

GCP achieves synchronous data collection by collating data from different data 'consumers' into synchronous frames. The other option for experiments where data synchronization is required is to record different data sources asynchronously with accurate enough timestamps to allow data to be aligned in analysis afterwards. GCPs frame-based data acquisition is dependent on a system clock known as the resource pulse synchronization signal (commonly called the RP pulse) to trigger synchronous data collection from various consumers. In our system, the RP pulse originates from a down-sampled clock signal off the dfMux motherboards. An absolute time reference is also transmitted between various systems using the IRIG-B standard that is generated with a GPS time source. The RP and IRIG-B distribution network for the POLARBEAR experiment is shown in Figure 2.22(a).

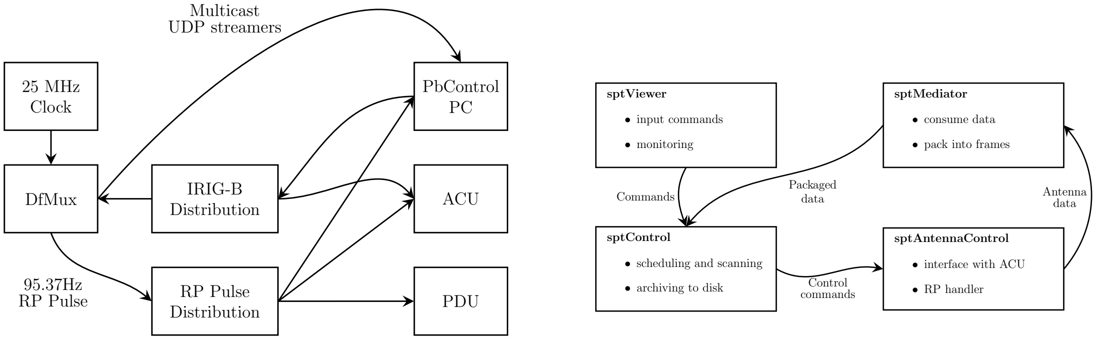

(a) Overview of the RP and IRIG-B distribution network for the POLARBEAR experiment.

(b) Overview of GCP's software sub-systems.

Figure 2.22: Data synchronization and acquisition using GCP.

An overview of the subsystems in the GCP software is shown in Figure 2.22(b). For POLARBEAR to function with GCP, we needed to create new consumers for detector timestreams, cryogenic readout, as well as any other desired systems.

2.4.2 Cryogenics control and data acquisition

Cryogenic readout and control of heaters for fridge cycling was provided by the ACBAR fridge controller and accompanying C and Python libraries. Jacob Howard rewrote the fridge controller control software to function with new system drivers enabling the software to be installed on newer systems. The Python software to interact with the controller was left unchanged, allowing us to use the same GCP consumer that the SPT experiment did. Another consumer was added by Chase Shimmin to allow acquisition of diode voltages from Lakeshore temperature monitors.

2.4.3 DfMux control and data acquisition

DfMuxMonitor

The DfMux provides access to the bolometer timestreams in the form of a multicast UDP streamer. Each motherboard streams all of its channels to a unique port on the network multicast IP using the UDP protocol. The streamers can be listened to by any devices attached to this network. Acquisition of readout-related housekeeping such as bolometer and SQUID bias parameters and motherboard component temperatures and debugging information can be achieved through CGI calls to the webserver running on each motherboard. Such CGI calls also allow control of the motherboards, enabling us to change the bias parameters of bolometers and SQUIDs.

To collect the data from all 42 dfMux motherboards in our experiment and package the non-sequential UDP packets appropriately for GCP, the DfMuxMonitor library was written. DfMuxMonitor was written by Jacob Howard with significant later modifications by Chase Shimmin and Haruki Nishino to enable integration with GCP. DfMuxMonitor uses the IRIG-B time stamp that arrives with each packet to sort the data appropriately and package it for a requested ordering of motherboards. To comply with the frame-based packaging of GCP, packets were required to arrive within a timed window to be included in the current frame.

PyPolarbear

To control all 1344 bolometers (1274 of those optical) and all 168 SQUIDs in the system, the PyPolarbear software package was written to help parallelize operation. PyPolarbear was originally written by Jacob Howard, with significant modifications made by many members of the collaboration, most notably Chase Shimmin, Bryan Steinbach, David Boettger and myself. The software provides an interface layer to the underlying pyWTL libraries provided by McGill University and the on-motherboard algorithm manager that they developed. PyPolarbear packages user commands for different motherboard algorithm managers and then sends requests to the boards. The software then waits for algorithms to finish executing and parses the returned data, creating plots to help the operator understand the system state. Simpler system commands can also be executed directly on the user selected list of motherboards, squids, or bolometers.

More recently, we've found that the algorithm manager is not a stable system due to memory leaks and fundamental problems with the on-board kernel used. PyPolarbear is currently being replaced with a new system called dfMuxLite that spawns many separate Python threads rather than interface with the algorithm manager to allow parallelized operation of many motherboards. DfMuxLite was written by Nicholas Harrington and Bryan Steinbach.

PbWaferview

Understanding the full system state is a difficult challenge with kilopixel arrays. To augment the information provided by PyPolarbear when the system is tuned, PbWaferview was written to provide more realtime information both during system tuning and as observations were occurring. This software package was written by David Boettger and can display several bolometer and SQUID parameters on a map of the array as well as timestreams and power spectra grouped by mux comb. This system has been helpful in both recognizing issues while optimizing system tuning and in carrying out observations on calibration sources.

Chapter 3

Pre-Cedar Flat Receiver Characterization

Once the baseline cyrogenic goals were met by reaching the desired base temperatures and hold times, we moved on to characterizing the optical performance and overall sensitivity of the POLARBEAR receiver in the lab. In Section 3.1, we discuss our efforts to measure the fractional throughput bandwidth product, $\eta\Delta\nu$ for various receiver configurations. As shown in Section 1.4.1, the dewar load can be a fundamental limit on the experiment's sensitivity that must be addressed. Unfortunately we did not have the necessary information on our detectors to investigate this directly, as we'll discuss in Section 3.1. Noise measurements of candidate detector wafers were carried out to help characterize and understand the detectors. These measurements were used to look for consistency with dewar load estimates. Results from noise measurements are presented in Section 3.2. Measurements of the spectral response of detectors were made and are described in Section 3.3. In sections 3.4 and 3.5, we discuss the near field beam map and polarization response measurements, respectively.

3.1 Fractional throughput and $\eta\Delta\nu$ measurements

A measurement of the fractional throughput is straightforward. If we have two loads of known temperature that can be placed at the window of the receiver, we can measure the power seen by the detectors in each case. Equation 2.2 can be rewritten with explicit terms for the optical power

$$P_{sat} = P_{opt} + P_b = P_{dewar} + \eta\Delta\nu kT + P_b \tag{3.1}$$

where P_b is the electrical bias power on the detector that we measure and we've separated the total optical power detected into optical power from the dewar thermal background P_{dewar} and from a beam-filling, Rayleigh-Jeans thermal source of temperature T outside the receiver. Solving for the dewar load P_{dewar}, we find

$$P_{dewar} = P_{sat} - P_b - \eta\Delta\nu kT \tag{3.2}$$

From Equation 3.2, we see that the fractional throughput bandwidth product can be found without prior knowledge of the saturation power. If the bath temperature and the dewar load remain constant for two different external thermal sources , both cancel out in differencing to find

$$\eta\Delta\nu = \frac{\Delta P_b}{k\Delta T} \tag{3.3}$$

The results from such a measurement are shown in Figures 3.1(a) and 3.1(b)

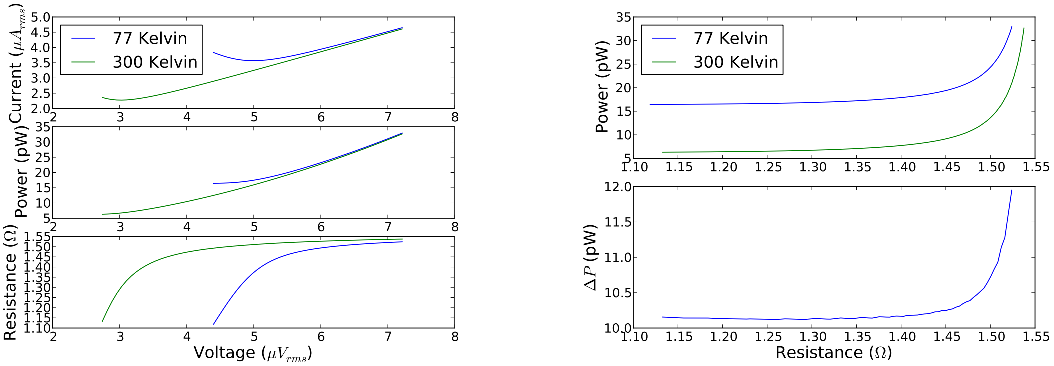

(a) Current, power and resistance versus voltage for the same bolometer looking at two different temperature loads

(b) Power versus resistance for the same bolometer at two different temperature loads and the resulting difference in power on the bolometer.

Figure 3.1: Resulting IV curves and ΔP versus R curves for a bolometer looking at 300 Kelvin and 77 Kelvin used to determine $\eta\Delta\nu$.

Once we find $\eta\Delta\nu$, the contribution to the optical power detected due to the dewar, or the 'dewar loading', can be found using Equation 3.2 *if* the saturation powers are known with sufficient accuracy.

With knowledge of the bandwith $\Delta\nu$ from spectral measurements, we can solve for the fractional throughput η once $\eta\Delta\nu$ is found. However, early in our efforts to characterize the fractional throughput of the POLARBEAR receiver, the bandwidth of our detectors was not accurately known. As we'll soon show in Section 3.3, spectra measured using a Fourier Transform Spectrometer (FTS) showed deep fringing that was dependent on the exact coupling of the receiver to the FTS output. These results did not seem to reflect the physical band pass of the instrument. Due to these initial issues, we started reporting the fractional throughput bandwidth product, $\eta\Delta\nu$ rather than the fractional throughput for an assumed bandwidth so as not to lose information in discussions.

3.1.1 Wafer XB1 fractional throughput

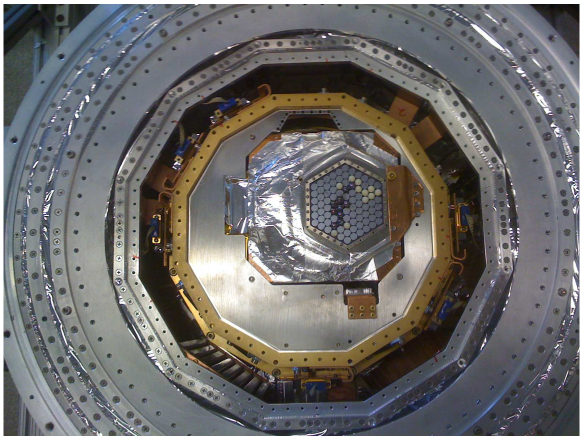

Figure 3.2: The XB1 test setup installed in the POLARBEAR receiver.

The first detector wafer to be characterized optically in the POLARBEAR receiver was wafer XB1 in the T-1 receiver configuration. This wafer had already been characterized earlier in a wet test dewar (POTC) that positioned the wafer directly below the window with thermal filters as the only optical elements. Wafer XB1 had both silicon lenslets and alumina lenslets installed on a silicon spacer wafer, as seen in Figure 3.2. The alumina lenslets were all missing anti-reflection coatings and a subset of the silicon lenslets were appropriately anti-reflection coated with thin PEI contact lenses (see [127] for details on the fabrication of these coatings) . The spectral band was also measured in POTC using the FTS, but as mentioned earlier, we didn't fully trust the bandwidth measurements at this point due to large scale, coupling-dependent fringing. For the sake of comparison, this distinction would only come into play if there were differences in the spectral response of the two receivers around the band of interest.

Table 3.1 shows the expected fractional throughput for an XB1 detector with an anti-reflection coated silicon lenslet in place given the optics of the T-1 receiver configuration. Note the 4% loss due to a load resistor mismatch, the narrower than designed band, and the loss due to a lack of antireflection coatings on the re-imaging lenses led to a relatively low expectation for the fractional throughput. This, coupled with the higher saturation powers of the XB1 bolometers allowed us to operate in the low transition without a neutral density filter in place.

Table 3.1: Estimate of XB1 fractional throughput in the POLARBEAR receiver for an anti-reflection coated silicon lenslet.

Element	Termination temperature	Element loss or reflection	Cumulative fractional throughput
Load resistor mismatch	0.5	4%	100%
Miscrostrip filter	0.25	90%	10%
Antenna mismatch	0.25	0%	86%
Antenna backlobe	0.25	9%	86%
Lenslet surface reflection	0.26	15%	79%
Collimating lens	6	12%	67%
Lyot truncation	6	11%	59%
Aperture lens	6	12%	52%
Lyot metal mesh filter	6	5%	46%
Field lens	6	12%	43%
4K metal mesh filter	6	5%	38%
4K IR shaders	20	2%	36%
HWP reflection	20	5%	35%
HWP loss	100	5%	34%
77K metal mesh filter	100	5%	32%
Teflon IR filter	100	4%	30%
77K IR shaders	150	5%	29%
300K IR shader	300	1%	28%
300K Zotefoam window	300	2%	27%
Total			27%

An interesting distinction was found between the fractional throughput measurement in the POLARBEAR receiver and the measurement in POTC as shown in Figure 3.3. First note that the anti-reflection coated silicon lenslet pixels match the expected level shown in table 3.1. The uncoated silicon lenslet pixels also agreed well when taking into account the expected reflection loss. The measurements in POTC showed no discernible differences between the two lenslet types. However, in the POLARBEAR receiver, the truncation of the beam at the cold aperture stop caused a decrease in the relative measured fractional throughput of the alumina lenslets compared to the silicon lenslets. This can be explained by the fact that the spacer wafer was not optimized for the index of alumina, giving pixels with the alumina lenslets wider than expected beams and allowing more power to be truncated at the stop. This effect would not have been observed in POTC since there is no beam truncation and the fractional throughput measurements were done with a setup that would have filled the entire beam in either case.

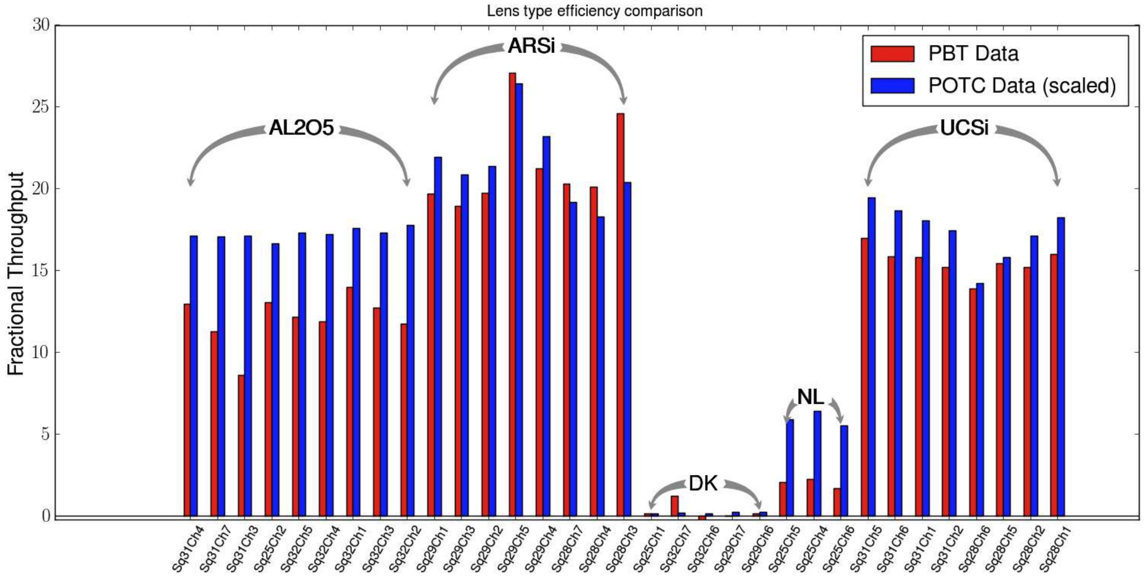

Figure 3.3: Comparison of XB1 fractional throughput in the Polarbear receiver and in the POTC wet test dewar.

Estimating dewar loading is a more difficult endeavor. Looking back at 3.2, we see that the dewar load can be found once we've measured $\eta\Delta\nu$.

$$P_{dewar} = P_{sat} - P_b - \eta\Delta\nu kT \tag{3.4}$$

However, to accurately measure the dewar load, we need to have an accurate measure of the saturation power for each bolometer. When this data was taken for the observation dewar, a dark run was not yet made to get the saturation powers on a per bolometer basis. Beyond that, we later found that the measurement of electrical power on the bolometers using our frequency domain multiplexed system depended on the parasitic inductance of the readout wiring. A measure of saturation powers in one setup could not be used in the calculation of dewar load in another setup without first fully characterizing the parasitics in both systems and correcting for them. Alternatively a dedicated dark run would need to be carried out using the same readout chain for the optical system being characterized. Given the constraints at the time, this was not done for XB1 in the POLARBEAR receiver.

3.1.2 Run T-0 fractional throughput

(a) The T-0 test setup consisting of wafer modules 8.2.0 and KT8 (closer to center) installed in the POLARBEAR receiver.

(b) The T-0 test setup after the neutral density filter has been installed above the focal plane.

Figure 3.4: The T-0 focal plane configuration.

Two wafer modules were installed in the receiver to be tested in the lab before the Cedar Flat deployment. These were wafers KT8 and 8.2.0, seen in Figure 3.4(a). Both wafers used anti-reflection coated alumina lenslets on silicon spacer wafers as the anti-reflection coating method for silicon lenslets was still being developed. The saturation powers of the bolometers on these wafers were previously measured in a dark dewar and found to be close to appropriate for observations with the Chilean atmosphere. With the use of different neutral density filters, these wafers could also be used in the lab to test against 300 Kelvin and 77 Kelvin loads, and to observe from our engineering run site in Eastern California.

The intention of this cryogenic run, named T-0, was to verify the cryogenic performance of the focal plane in a deployment-ready configuration, integrate a larger fraction of the readout system, and verify optical properties of the integrated receiver and detectors across the focal plane. A neutral density filter (NDF) that was 0.375 inches thick, resulting in a 20 percent expected transmission in our spectral band was used. The filter was machined from MF-110 magnetically loaded, machinable epoxy stock[1] and anti-reflection coated using a thin teflon sheet epoxied to both NDF surfaces. It was installed just above the milliKelvin stage anchored to the 4 Kelvin stage, as shown in Figure 3.4(b).

The fractional throughput bandwidth product was measured, again using beam filling loads at 300 and 77 Kelvin. The results are shown in Figure 3.5, with a mean

---

[1] http://www.eccosorb.com/products-eccosorb-mf.htm

Table 3.2: Estimate of 8.2.0 fractional throughput in the POLARBEAR receiver for the T-0 run.

Element	Termination temperature	Loss or reflection	Cumulative fractional throughput	T_{RJ} referred to window (K)
Load resistor mismatch	0.5	0%	100%	0
Miscrostrip filter	0.25	8.2%	100%	0
Antenna mismatch	0.25	0%	91.8%	0
Antenna backlobe	0.25	9.0%	91.8%	0
Lenslet surface reflection	0.25	15.0%	83.5%	0
Attenuating filter	5	80.0%	71.0%	15.9
Collimating lens	7	5.0%	14.2%	0.4
Aperture stop truncation	6	13.0%	13.5%	0.7
Aperture lens	7	5.0%	11.7%	0.3
Metal mesh reflection	7	2.0%	11.15%	0.1
Metal mesh absorption	7	2.0%	10.9%	0.1
Field lens	7	5.0%	10.7%	0.3
Metal mesh reflection	7	2.0%	10.2%	0.1
Metal mesh loss	20	2.0%	10.0%	0.4
4K IR shaders	20	2.0%	9.8%	0.4
HWP reflection	25	2.0%	9.6%	0.5
HWP loss	70	2.0%	9.4%	1.6
Metal mesh reflection	50	2.0%	9.2%	1.1
Metal mesh loss	90	2.0%	9.0%	2.0
Teflon filter absorption	90	4.0%	8.8%	3.8
Teflon filter reflection	100	1.6%	8.5%	1.6
77K IR shaders	80	5.0%	8.5%	4.0
300K IR shader	100	1.0%	8.0%	1.0
300K Zotefoam window	300	1.0%	8.0%	2.9
Total			8.0% $\eta\Delta\nu$ =3GHz	37.2

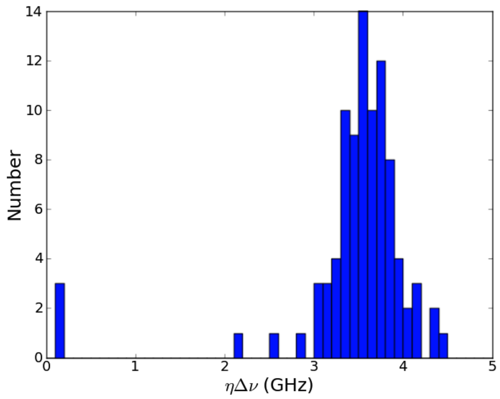

Figure 3.5: Measured $\eta\Delta\nu$ from the T-0 run on wafer 8.2.0.

$\eta\Delta\nu$ consistent with 3.75GHz. This corresponds to an efficiency of 12.5% given the measured 30Ghz bandwidth of test pixels from wafer 8.2.0. This result is significantly higher than the expectations shown in table 3.2 and wasn't well understood at the time. Later measurements that we will describe in Section 5.1.1 showed that our detectors were sensitive to out of band excess power. It is likely that the same effect was causing this inconsistently high $\eta\Delta\nu$ and inferred efficiency, though the necessary data was not available to verify this was the case.

3.2 Noise measurements

Early in-lab noise measurements focused on quantifying the low frequency performance of detectors readout with the dfMux and verifying the expected white noise level of detectors. As discussed in Section 1.4.3, the low frequency noise performance of detectors is crucial in determining the necessary scan strategy of the experiment to enable large scale measurements. For early work on the XB1 wafer, our efforts focused on understanding how correlated low frequency noise sources were within a pixel pair of detectors and how well the low frequency noise spectrum from a single detector measurement can be suppressed for a differenced pixel.

As discussed in Section 2.2.4, the expected white noise level can be found given the known optical power P_{opt} on the detector, the bias power P_b being used, the detector loopgain $\mathcal{L}$ and resistance at its bias point and the transition temperature T_c. To accurately get the optical power at the detector, the fractional throughput, dewar load and external load must be known. An alternative is to accurately know the saturation power, getting the total optical power as the difference between this and the measured electrical power on the bolometer. On its own, this does not provide any information on either the dewar load or the fractional throughput of the receiver. Accurate measurements or estimates of these properties were not available for the XB1 wafer testing, but testing on the wafers in the T-0 focal plane focused on validating the white noise level of the detectors.

3.2.1 XB1 noise measurements

Noise measurements were made by recording simultaneous timestreams for all active bolometers in the XB1 configuration with both 77 Kelvin and 300 Kelvin beam-filing loads at the receiver window. Measurements can be taken with bolometers overbiased to verify the expected noise contributions from Johnson noise and SQUID readout, and at various bias points in the transition to understand the loopgain and responsivity dependent noise effects.

Noise spectral densities are found from the timestreams by Fourier transforming the discretely sampled timestreams. The following discussion closely follows [128]. For a timestream $c(t)$ sampled at N points at a frequency f_{samp} giving values $c_0, \cdots, c_{N-1}$, we have the discrete Fourier transform

$$C_k = \sum_{j=0}^{N-1} c_j e^{2\pi ijk/N} \qquad k = 0, \cdots, N-1 \tag{3.5}$$

The mean squared amplitude of the signal over the sample time is given by

$$\frac{1}{N}\sum_{j=0}^{N-1} |c_j|^2 = \frac{1}{N^2}\sum_{k=0}^{N-1} |C_k|^2 \tag{3.6}$$

where we've used the discrete form of Parseval's theorem in the last equality. An estimate of the power in the signal at the $N/2+1$ frequencies that we've Nyquist sampled can be found by the periodogram estimate

$$\begin{aligned} P(f_0) &= |C_0|^2 \\ P(f_k) &= \left[|C_k|^2 + |C_{N-k}|^2\right] \qquad k = 1, \cdots, \left(\frac{N}{2} - 1\right) \\ P(f_c) &= |C_{N/2}|^2 \end{aligned} \tag{3.7}$$

where the frequencies are given by $f_k = kf_{samp}/N$, with running from 0 to $N/2$. For simplicity, we'll notate the above periodogram as P_k.

The discrete power spectral density (PSD), $\mathcal{P}_k$ should be normalized such that the integral of the PSD over a given frequency band gives the contribution to the mean squared amplitude of the timestream from that band. In the discrete case, considering summing over all frequencies, this gives

$$\frac{f_{samp}}{N}\sum_{k=0}^{N/2}\mathcal{P}_k = \frac{1}{N}\sum_{j=0}^{N-1}|c_j|^2 = \frac{1}{N^2}\sum_{k=0}^{N/2}P_k \tag{3.8}$$

where we've used Equation 3.6 and our chosen periodogram normalization. This leads to the following normalization for the PSD

$$\mathcal{P}_k = \frac{1}{f_{samp}N}P_k \tag{3.9}$$

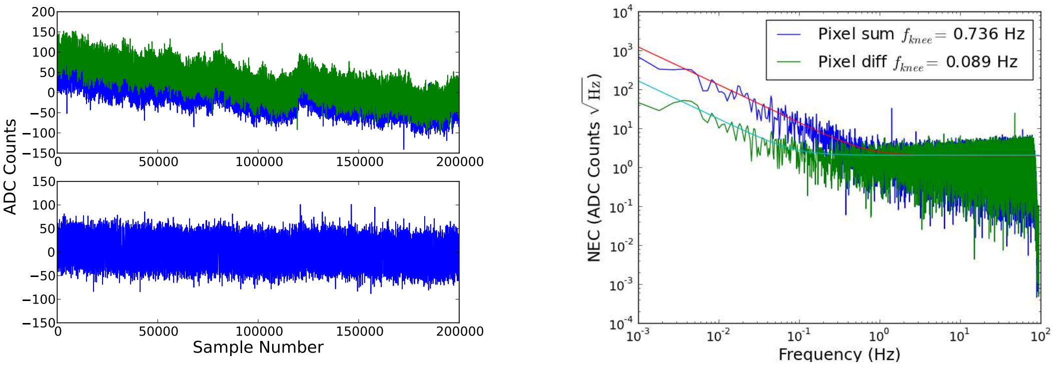

(a) Timestreams from two detectors within a pixel (upper panel) and the difference timestream (lower panel).

(b) NEC for a single detector (upper panel) and the NEC for the pixel differenced timestream.

Figure 3.6: Measurements of noise for a pixel pair of detectors on XB1.

The upper panel of Figure 3.6(a) shows the timestreams from two single detectors within a pixel, both biased $\sim 70\%$ into the transition. Normalizing the timestream gains within a pixel to each other and then summing and differencing the normalized timestreams in a pixel pair before Fourier transforming gives us the pixel sum and difference amplitude spectral densities. This allows us to see how well the low frequency noise can be suppressed and therefore attributed to common mode variations in wafer base temperature, readout comb voltages or optical power. Since a polarization measurement is made by differencing our detectors, the difference amplitude spectral density directly tells us how our low frequency noise limits large scale polarization measurements.

The noise equivalent counts (NEC), equal to $\sqrt{\mathcal{P}_k}$ from Equation 3.9 and in units of [Counts/$\sqrt{Hz}$] for the sum and difference of the two timestreams is shown in Figure 3.6(b). We fit the resulting spectra to the model

$$\mathrm{NEC}(f) = \mathrm{NEC}_{\mathrm{floor}}\sqrt{1 + \left(\frac{f_{knee}}{f}\right)^{\alpha}} \tag{3.10}$$

to quantify the low frequency noise. Note that f_{knee} is at 736 mHz for the pixel sum NEC, dominated by the slow variations clearly seen in the timestream. In the lower panel of Figure 3.6(a), we can see that the difference timestream has suppressed a substantial amount of these common mode variations seen in individual detectors. This is also reflected in the difference NEC in Figure 3.6(b), where the low frequency knee has been suppressed to 89 mHz.

3.2.2 T-0 noise measurements

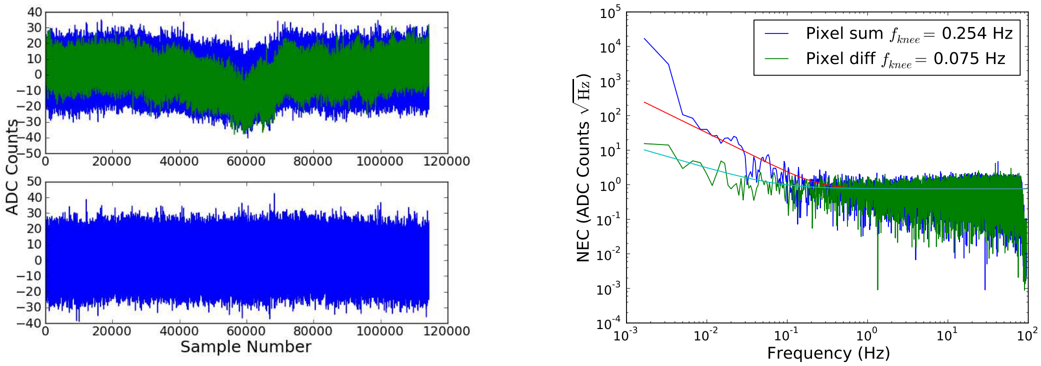

(a) Timestreams from two detectors within a pixel (upper panel) and the difference timestream (lower panel).

(b) NEC for a single detector (upper panel) and the NEC for the pixel differenced timestream.

Figure 3.7: Measurements of noise for a pixel pair of detectors in the T-0 run.

Noise properties of detectors were compared to expectations given the measured properties of the detectors. Measurements of $\eta\Delta\nu$ were made on a per-detector basis as described in Section 3.1. This value, along with detector properties derived from the detector IV curves and an estimate of the dewar load from table 3.2 were used to provide estimates for expected noise contributions. We show the measured detector properties and noise expectations for an example detector on wafer 8.2.0 in tables 3.3 and 3.4, respectively.

Table 3.3: Example measured bolometer properties.

Bolometer property	Value
Bias power P_b	16.5 pW
$\eta\Delta\nu$	3.3 GHz
Dewar load	37 K
Optical power P_{opt}	5.2 pW
Total operating power P_{tot}	21.6 pW

Table 3.4: Expected noise contributions from various noise terms given the example bolometer properties in table 3.3. Note that the readout noise is the measured value with demodulator gain = 2.

Noise component	Contribution ($aW/\sqrt{Hz}$)
Photon noise	44
Phonon noise	36
Readout noise	28
Total	63

Figures 3.7(a) and 3.7(b) show example timestreams and noise equivalent counts for a pixel pair of detectors, as discussed in the previous section. Note that the $1/f$ knee in the differenced timestream is suppressed to 75 mHz even for these optical pixels. The noise floor from similar fits to individual detectors was used in calculating the NEP of individual detectors.

The readout noise contribution was measured explicitly by measuring a timestream at a demodulation frequency of 200 kHz, far away from the bolometer comb. This estimate was used rather than the calculated expected readout noise contribution since the readout noise contribution is slightly higher than expected and we were interested in probing the bolometer properties and avoiding confusion in excess noise contributions. Histograms of the measured noise-equivalent current (NEI) and resulting NEP from the readout contribution are shown in Figures 3.8(a) and 3.8(b). The larger spread in NEP arises from the spread in detector responsivities.

In Figures 3.9(a) and 3.9(b), we show histograms of the measured NEP along with the ratio of measured over expected NEP for all active detectors. The distribution of measured values is found to peak around 20% higher than expectations, with the majority of detectors well within 40% of expectations.

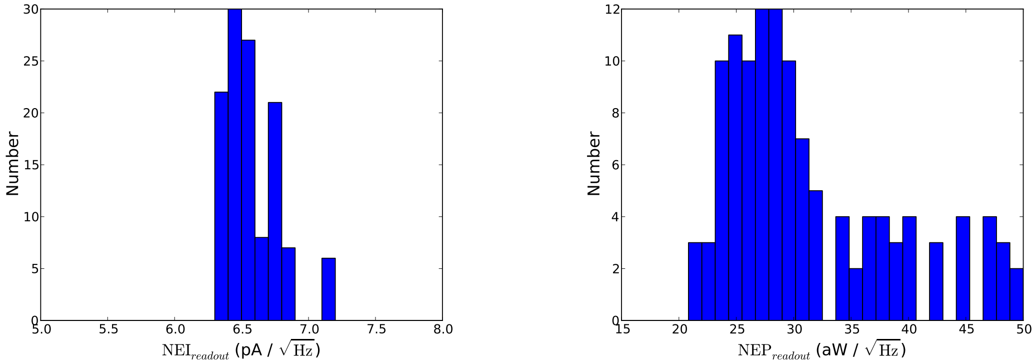

(a) Measured noise equivalent current (NEI) for SQUID readout at 200 kHz demodulation frequency

(b) The resulting readout NEP found by multiplying the measured NEI by the individual detector responsivities.

Figure 3.8: Measured readout noise equivalent current (NEI) and resulting contribution to detector NEP.

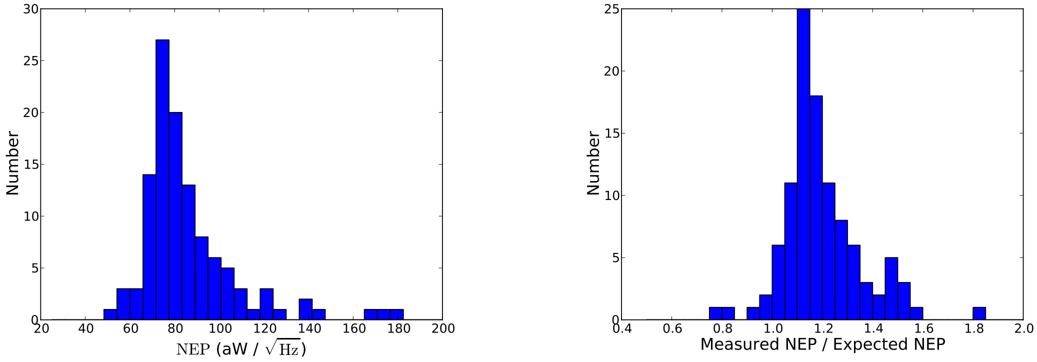

(a) Measured NEP for all active detectors in the T-0 run, looking at 77 Kelvin load.

(b) Ratio of measured to expected NEP for all active detectors in the T-0 run.

Figure 3.9: Measured versus expected NEP for the T-0 run.

3.3 Fourier transform spectroscopy

Fourier transform spectroscopy provides a useful technique to measure the band pass of our instrument. A Fourier transform spectrometer is simply constructed from a two-beam interferometer with a variable path length introduced on one of the two legs, as shown in Figure 3.10. For an ideal interferometer where half of the signal is

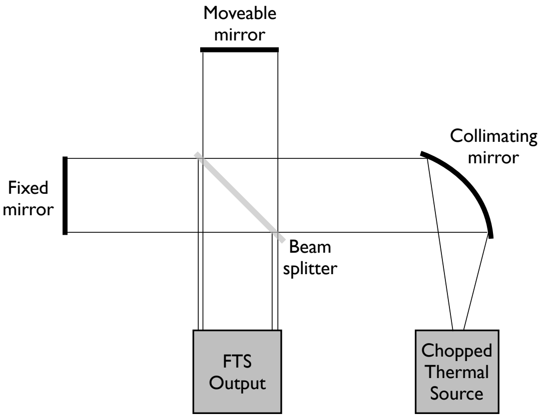

Figure 3.10: Schematic of a simple Fourier transform spectrometer. In this example, a parabolic mirror is used to collimate the beam from a source before it is split into two arms at the beam splitter. Optics are used to refocus the collimated output beam of the FTS.

reflected by and the other half transmitted by the beamsplitter, the resulting intensity at the output of the interferometer as a function of the path difference x is given by

$$I(x) - \frac{1}{2}I(0) = \int_0^\infty S(\sigma)\cos 2\pi\sigma x d\sigma \tag{3.11}$$

where $S(\sigma)$ represents the power spectrum of the source convolved with the spectral response of the interferometer and detector and σ is the wavenumber $1/\lambda$. We can carry out the Fourier transform to recover the spectrum

$$S(\sigma) = 4\int_0^\infty [I(x) - \frac{1}{2}I(0)]\cos 2\pi\sigma x dx \tag{3.12}$$

In practice, a discrete number of samples of the interferogram over a limited range of path length is taken. The resulting discrete spectrum is given by the convolution between the continuous spectrum and the instrument resolution function

$$S'(\sigma_m) = \frac{1}{N}\int_0^\infty S(\sigma)C(\sigma,\sigma_m)d\sigma \tag{3.13}$$

$$C(\sigma,\sigma_m) \approx \frac{2\sin N\alpha}{\alpha} \tag{3.14}$$

where $\alpha = 2\pi\Delta x(\sigma - \sigma_m)$ [129]. The sampled frequencies are given by $\sigma_m = m/2L$ where L is the maximum path length difference of the interferogram. The maximum wavenumber sampled is limited by the interferogram step size Δx and is given by $1/(2\Delta x)$ by the sampling theorem of information theory [130]. To avoid aliasing of higher frequency power into the measurement, low pass filters are generally employed to guarantee that $S(\sigma) = 0$ for all frequencies $\sigma > 1/(2\Delta x)$.

Since $S(\sigma)$ gives the spectrum of the source multiplied by any spectral filters of the interferometer and the detector itself, a reference spectrum taken with a flat response, broad-band detector can be used to divide out the source and interferometer spectral response and recover the band pass of the instrument and detectors. Alternatively, an estimate of this can be made for a source of known spectral dependence, such as a liquid nitrogen cold load, and for the known properties of dielectric beam splitters if other effects in the interferometer can be ignored.

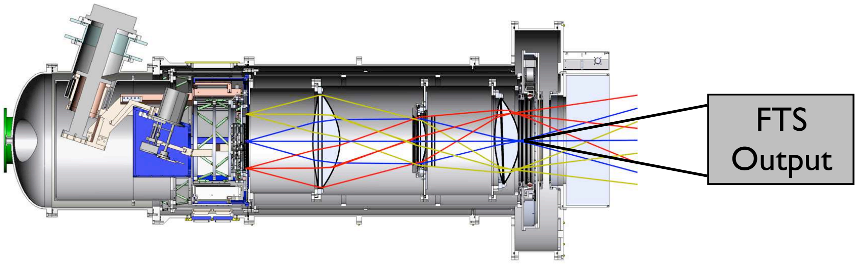

Figure 3.11: Setup of the FTS measurements for T-0. Note that the $f/2.5$ output mirror of the open air FTS results in an under-filled beam for the $f/1.8$ detector beams exiting the receiver.

For POLARBEAR, measurements were made by coupling an open-air FTS to the receiver. Efforts were made to couple the output focus of the FTS to the field focus point in the receiver, as shown in Figure 3.11. As we'll discuss in Section 5.2.2, having the detector beam's solid angle filled by the imaged source is critical for accurately measured bands. This requirement was not met during these early measurements. As shown in Figure 3.12, the resulting spectrum shows deep fringing across the band. The level and location of the fringing varied with subtle alignment changes of the receiver relative to the spectrometer. Further investigation of this effect with a test pixel in a smaller wet dewar convinced us that the fringing was not inherent to the microstrip filters themselves and due to reflections in the system.

The fringing spacing can be related to the distance between reflectors in a Fabry-Perot resonator. For resonator surfaces with reflectance R, the transmission in the Fabry-Perot is given by

$$T = \frac{1}{1 + F \sin^2 \delta/2} \tag{3.15}$$

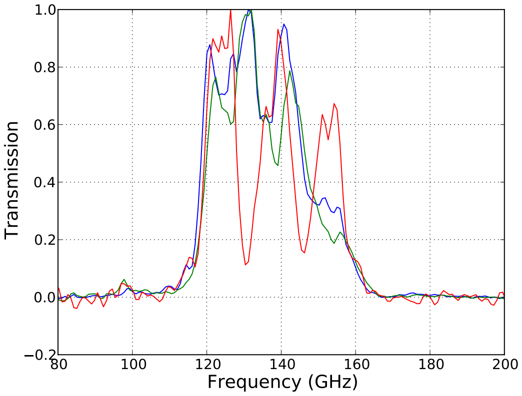

Figure 3.12: Measured spectra for several detectors in the T-0 run. Note that there is consistent fringing with $\Delta f \sim 15GHz$ seen in all curves.

where $F = 4R/(1-R)^2$ is the coefficient of finesse and

$$\delta = \left(\frac{2\pi f}{c}\right) 2nl\cos\theta \tag{3.16}$$

where θ is the beam's angle of incidence to the resonator input and n is the index of refraction in the resonator. The fringe spacing is therefore related to the physical spacing in the resonator by

$$\Delta f = \frac{c}{2nl\cos\theta} \tag{3.17}$$

Assuming $\theta \sim 0$ and using $n \sim 3.2$ for alumina, the ∼15GHz spacing seen in the fringes corresponds to $l = 3.13$ mm. This is a close match to the 3 mm radius of the alumina lenslet, the difference possibly being accounted for from $\theta \neq 0$ at the lenslet surface. If the resonator were occuring in some other optical elements in the optical chain in vacuum, the distance would correspond to 10 mm.

As the resonator distance found was quite suggestive of the lenslets being involved, a solution to this was explored in later runs by ensuring the full solid angle of the beam was filled. The goal of this approach was to average over the reflections from all angles of the beam, effectively reducing the finesse of the cavity. As we'll show in 5.2.2, this resulted in significantly lower fringing and improved measurements of the true spectrum.

3.4 Beam maps

Near-field beam maps of all active detectors were also carried out during the T-0 run. These maps were made near the window of the receiver using a chopped liquid

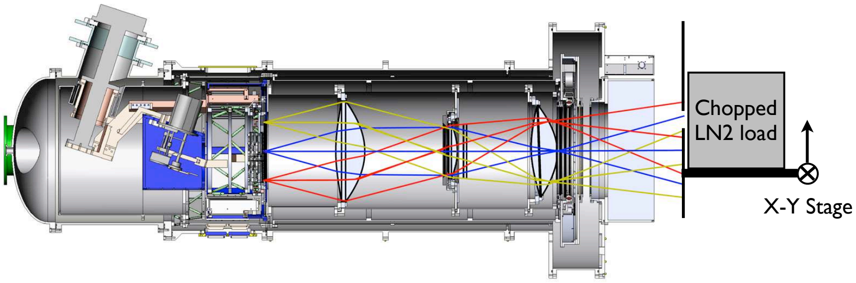

Figure 3.13: Setup for near-field beam mapping on the POLARBEAR receiver.

nitrogen source behind an aperture and mounted to a vertically oriented x-y stage, as shown in Figure 3.13.

The expected beam sizes were found through Zemax ray tracing simulations and are shown in Figure 3.14. Results from the beam maps of two detectors in a single pixel along with contours for the best-fit Gaussian beams are shown in Figures 3.15(a) and 3.15(b).

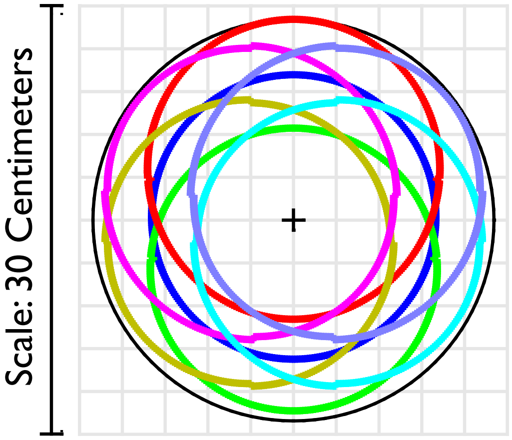

Figure 3.14: Beam footprints from different positions on the focal plane shown at the window where near field beam maps were done. The footprints correspond to the aperture stop vignetted ray-traced beams, or the 10dB level.

From these near field maps, we were able to see that the beams were nearly Gaussian and had the expected beamwidths of $\sim$ 22 cm at the 10 dB contour. A small sidelobe was seen at the $\sim$ 20dB level on several pixels at the same position, as seen on the right side of the maps in Figure 3.15. This sidelobe was not seen above

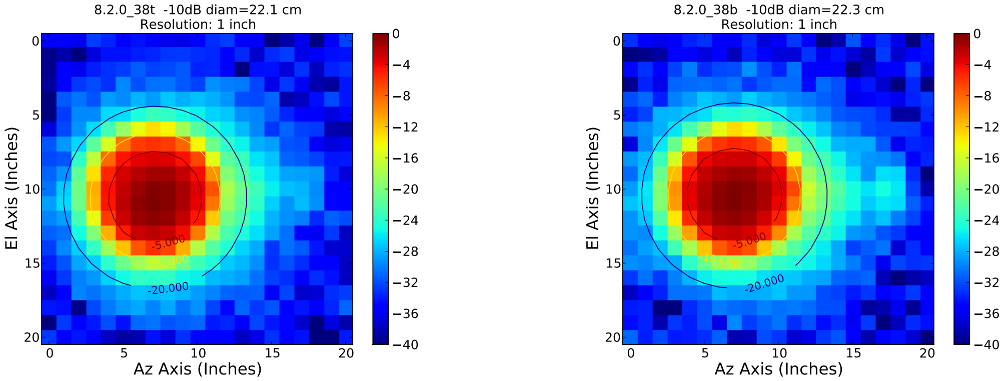

(a) Near field beam map of the top detector of a pixel pair. Contours are for the best-fit Gaussian.

(b) Near field beam map of the bottom detector of a pixel pair. Contours are for the best-fit Gaussian.

Figure 3.15: Individual detector beammaps taken in the near field of the receiver.

the level of the noise for most central pixels of the focal plane. Because of this, at the time the sidelobe was attributed to scattering off a diode that was left attached at the edge of one of the metal mesh filters in the optical stack. The limited travel of the beam mapping setup did not let us explore far sidelobes at the receiver.

3.5 Polarization sensitivity

Polarization sensitivity was measured using a rotating polarizing grid between the chopped LN2 load and the receiver window. The setup is illustrated in Figure 3.16. The grid was moved to several angles using a stepper motor and the magnitude of the chopper response measured at each angle. Such a measurement was carried out for several HWP positions to verify the expected polarization performance and modulation. Results from these measurements are shown in Figure 3.17 for a pair of detectors within a pixel. These results demonstrated the functionality of our HWP and showed that the polarization sensitivity of our detectors, measured earlier in simpler receivers, was not being degraded by other optical elements in our receiver.

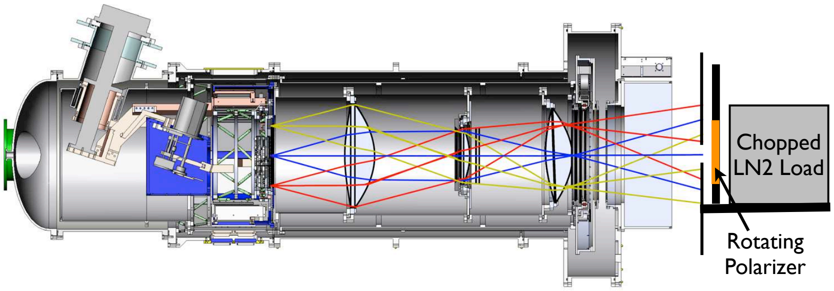

Figure 3.16: Setup for polarization sensitivity measurements in the POLARBEAR receiver. Note that the polarizer was set at an angle of 45 degrees to the receiver window to mitigate reflections, which is not indicated in this illustration.

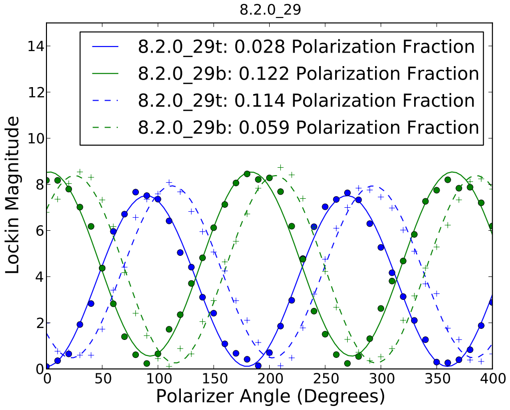

Figure 3.17: Results for the polarization sensitivity of a pixel pair. The filled circles (pluses) show the response with the HWP at 0 (11.25) degrees.

Chapter 4

The Cedar Flat deployment

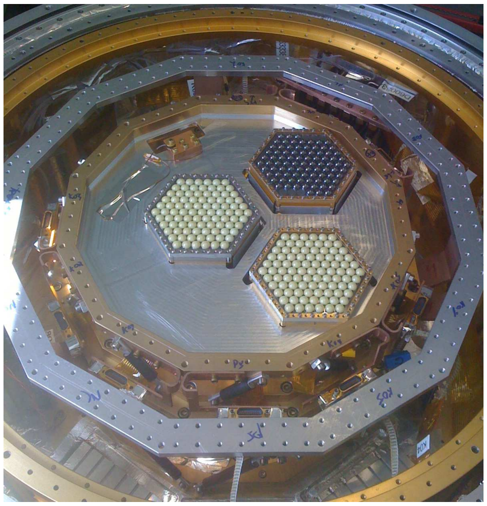

Figure 4.1: The focal plane deployed in Cedar Flat, installed in the receiver.

The successful integration tests performed on the POLARBEAR receiver presented in the previous chapter allowed us to deploy the full experiment in an engineering run at the Cedar Flat site in the eastern Sierra mountains in the spring and summer of 2010. Much of the infrastructure for this deployment was graciously provided by the CARMA observatory. The Huan Tran Telescope was constructed and taken through preliminary servo and control tests by a team from Vertex RSI and members of our collaboration earlier that year. The POLARBEAR receiver was disassembled in the lab, shipped to Cedar Flat, unpacked, reconstructed in a lab container at the site and installed on the receiver within one month. The focal plane installed, shown in Figure 4.1, consisted of the wafers 8.2.0 and KT8 from the T-0 configuration discussed in the previous chapter, plus a third wafer, 8.2.1, with similar properties to 8.2.0. Readout was limited to allow 2/7 of all possible detectors to be read out. Due to its poor yield, only 1/3 of the KT8 wafer was read out to enable 2/3 of wafer 8.2.1 and the full 8.2.0 wafer to be read.

I was primarily responsible for the organization of the deployment of the receiver to Cedar Flat and the disassembly, shipping and reconstruction of the receiver. Once mounted in the telescope, the receiver cooldown took another 7 days and first light was achieved with an elevation nod on April 16th, 2010 with the telescope nominally aligned. A scan of Jupiter was performed shortly after that on April 18th, 2010. Alignment of the receiver and secondary mirror with respect to the primary mirror was refined by a combination of measurements to tooling balls and theodolite targets using a coordinate measuring machine (CMM) arm and a theodolite as well as through feedback from planet maps made at several focus positions.

In this chapter, we present the final results from the Cedar Flat deployment. Since the temperature of the atmosphere at the Cedar Flat site averages around 80 Kelvin for the elevations we were observing at, a 50% transmissive NDF was used. The high opacity and atmospheric fluctuations of the Cedar Flat site coupled with reduced instrument throughput meant maps of blank CMB fields on the sky would require long integration times to resolve features. Instead, the goal of this deployment was a proof-of-concept of the instrument. Data products desired included:

- **Planet maps** to measure the throughput and NET of the system as well as characterize the individual and differential beam properties of the instrument.
- **Pointing measurements** using millimeter maps of celestial sources as well as optical measurements with a separate star camera to validate our telescope control and begin to develop a pointing model.
- **Polarization sensitive measurements** of both ground based and celestial sources. This would allow us to prove the instrument met its requirements on polarization sensitivity and purity, as well as allow us to characterize the polarization modulation provided by our half-wave plate, contributing to our understanding of systematic errors.

4.1 Planet maps

Maps of planets such as Mars and Jupiter provide a unique ‘all-in-one’ method to measure several aspects of the instrument’s performance. If the source is significantly smaller than the designed beam-size, a planet provides a way to probe the structure of the beams themselves. This allows the designed beam-size to be verified for every detector. The location of each pixel on the sky relative to the telescope boresite pointing, known as the pixel offset, is also measured from these maps to allow co-adding of individual detector maps. Gain-calibrating the two detectors of a single pixel via

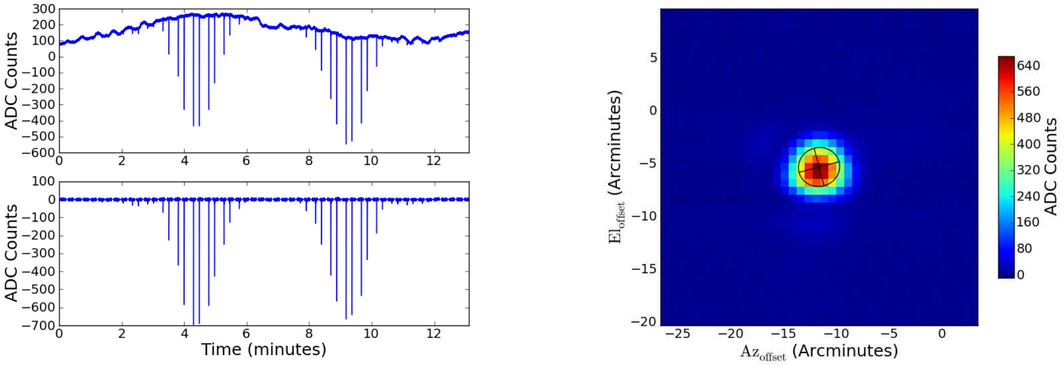

(a) Unfiltered (upper) and filtered (lower) timestream for a single detector

(b) Map of a single channel produced by binning the filtered timestream in azimuthal and elevation coordinates

Figure 4.2: Raw and filtered timestreams (a) and resulting map (b) of a single detector channel rastering a planet with and without polynomial filtering applied.

the response to atmospheric signal or using the beam map itself normalized to a known source temperature, the planet maps can also be used to probe the differential beam properties of each pixel by differencing the two orthogonal polarizations of each pixel and characterizing the residual multipole moments, as discussed in Section 1.4.2. Planet maps also provides a means to measure both the fractional throughput bandwidth product, $\eta\Delta\nu$ and the detector NET directly for a known planet temperature and angular extent. If dark saturation powers of the bolometers are known, an estimate of the dewar loading can also be made and checked for consistency with the measured NETs. Finally, beam maps of planets and other non-extended sources that cover a larger range of azimuth and elevation values can be used to develop a pointing model for the telescope. We present in this section the results from analyses to investigate all of these.

In Figure 4.2(a), we show the raw data timestream from a single detector for a raster scan of Jupiter. A raster scan simply sweeps the telescope in azimuth, taking small elevation steps after one to several azimuth sweeps. The sharp peaks correspond to the planet crossing the detector beam at different elevations, and the remaining structure is due to both signal from the atmosphere and whatever other drifts are present in the system. The lower panel in Figure 4.2(a) shows the same data after a simple polynomial removal filter has been applied to each constant velocity subscan and the regions where the telescope was accelerating have been zeroed. An important subtlety in this filtering is that an accurate baseline must be established by masking the area surrounding the beam response so that power is not inadvertently subtracted from the beam.

To get the detector offsets from the telescope boresite, we must first transform to the appropriate coordinate system. The telescope boresight can be represented by rotations in azimuth and elevation of a unit vector.

$$\vec{v}_{az,el} = R_b^{az,el}\hat{x} = R_z^{az} R_y^{el}\hat{x} \tag{4.1}$$

If we see the peak response from a planet at a given az, el in a particular bolometer for a particular boresite pointing, we can represent the detector offset as an additional rotation, R_o, to be applied:

$$R_p\hat{x} = R_b R_o\hat{x} \rightarrow R_o = R_b^{-1}R_p = R_y^{-el}R_z^{-az}R_p \tag{4.2}$$

Inserting the planet azimuth and elevation coordiantes az_p, el_p, we find

$$R_o = R_y^{-el}R_z^{-az}R_z^{az_p}R_y^{el_p} = R_y^{-el}R_z^{az_p-az}R_y^{el_p} \tag{4.3}$$

For the case of a raster scan where we track a planet and apply small perturbations in azimuth sweeps and elevation steps, the boresite pointing angles are represented by

$$\begin{aligned} az_b &= az_p + \delta_{az} \\ el_b &= el_p + \delta_{el} \end{aligned} \tag{4.4}$$

We can explicitly solve for the offset angles in the approximation of small perturbations:

$$\begin{aligned} az_o &\approx \delta_{az}\cos(el_p) \\ el_o &\approx \delta_{el} + \frac{\delta_{az}^2}{2}\cos(el_p)\sin(el_p) \end{aligned} \tag{4.5}$$

Note that there is an elevation dependence to both offset coordinates and that the elevation offset is also dependent on the square of the azimuth perturbation.

If we use the rotation matrix in Equation 4.3 to transform the boresite pointing to the offset coordinate system, the azimuth and elevation offsets that we find for the beam centers give us the appropriate rotation angles to apply to offset each detector. Taking the timestream data shown in Figure 4.2(a) and binning in the azimuth and elevation offset coordinates produces the map shown in Figure 4.2(b). Fits to the timestream data and offset coordinates are made using the two dimensional elliptical Gaussian model in Equation 1.52 to get the beam offsets and beam parameters for each detector in the full array. The measured beam offsets and beam widths for the entire array are shown in figures 4.3(a) and 4.3(b) for both 'top' and 'bottom' detectors, respectively. Applying the offsets and normalizing each individual detector beam to the peak of the Gaussian fit allows us to combine data from multiple detectors

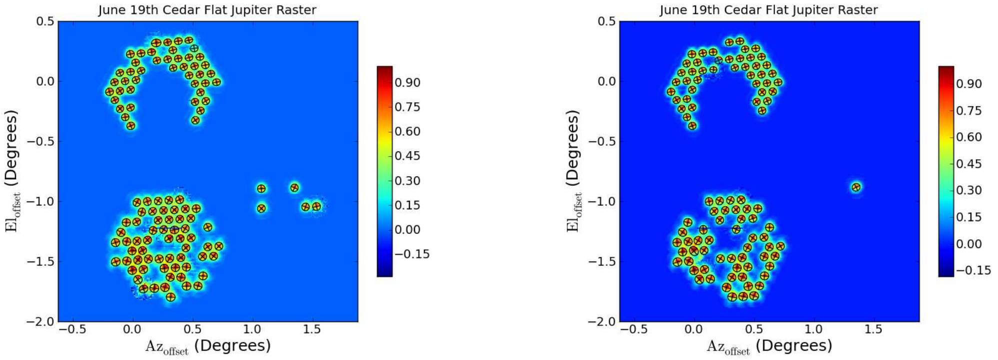

(a) 'Top' detector beam maps and elliptical Gaussian fits across the focal plane.

(b) 'Bottom' detector beam maps and elliptical Gaussian fits across the focal plane.

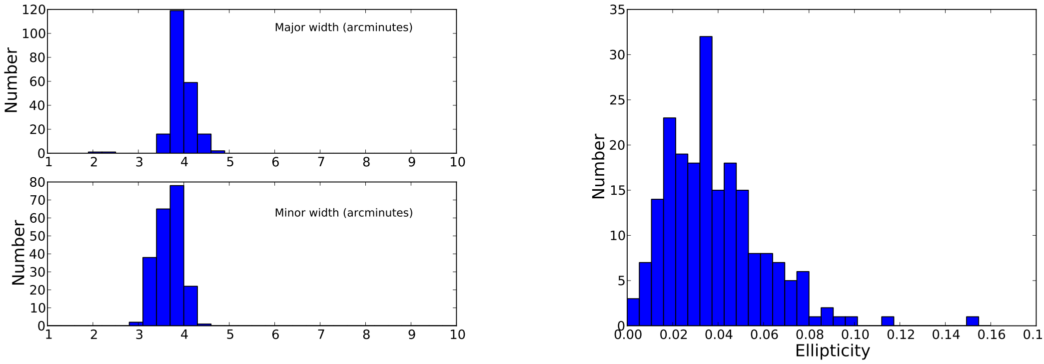

(c) Measured major and minor beamwidths

(d) Measured ellipticity.

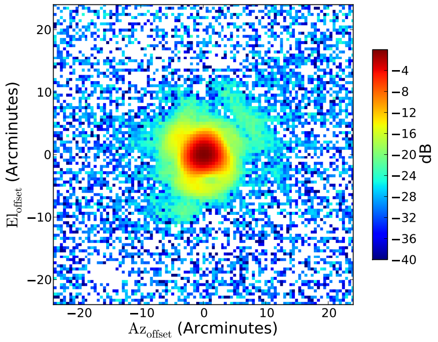

(e) Coadded instrument beam.

Figure 4.3: Detector beam offsets, beam widths and ellipticities from beam maps and the full instrument co-added beam.

for higher fidelity maps, as shown by the co-added full array beam map in Figure 4.3(e). Histograms of the major and minor beamwidths as well as the ellipticity from the Gaussian beam fits are shown in figures 4.3(c) and 4.3(d).

4.1.1 Differential beams

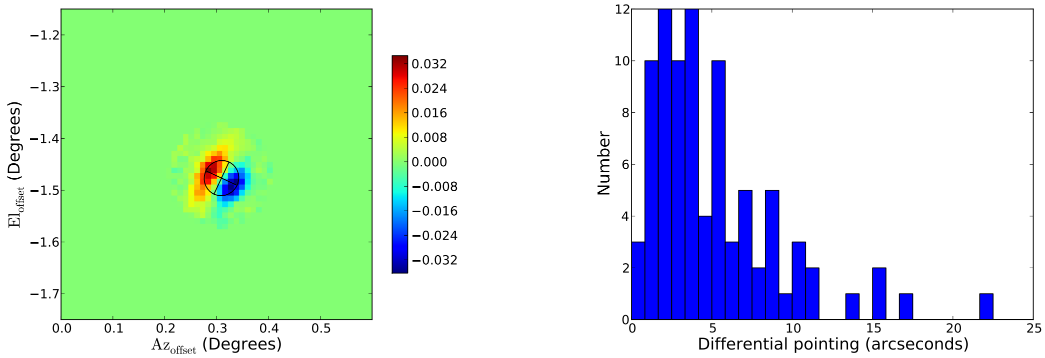

(a) An example measured differential beam for a pixel. The single detector beams are normalized to 1 before differencing.

(b) Measured differential pointing for all active pixels from a Jupiter planet observation.

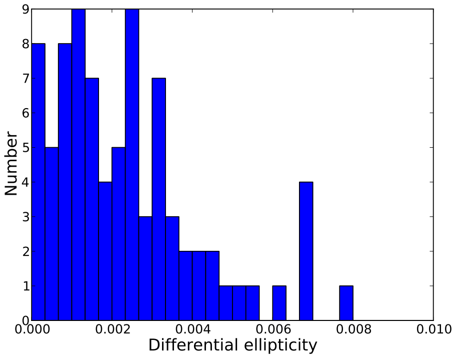

(c) Measured differential ellipticity for all active pixels from a Jupiter planet observation.

Figure 4.4: Measured differential beams and differential beam properties for all active pixels.

Differencing the individual detector pair within a pixel gives us a map of the differential beam. As seen in Figure 4.4(a), the differential beams are dominated by the dipole effect of differential pointing. Histograms of the differential pointing and ellipticity are shown in Figures 4.4(b) and 4.4(c), respectively.

In Figure 4.5, we show the resulting contributions to the B-mode systematic signals from the average measured levels of differential beam asymmetries. The dominant component for $l > 100$ is that due to differential pointing. For reference, we also plot the contribution of differential pointing when sky rotation is employed in the scan strategy to average down the effect. Even in this case, the differential pointing contribution remains dominant when considering a single detector.

As with all differential beam asymmetries, the truly important quantity is the *uncertainty* in the measured asymmetry. Assuming the ability to accurately measure the differential pointing for each detector, the contribution to the systematic signal from the combined beams would decrease as $1/\sqrt{N_{det}}$. In this way, while we're above the required level of differential polarization beam asymmetry for a single-detector instrument, the level for our multiple-detector instrument will not adversely effect our measurement of the B-mode spectrum.

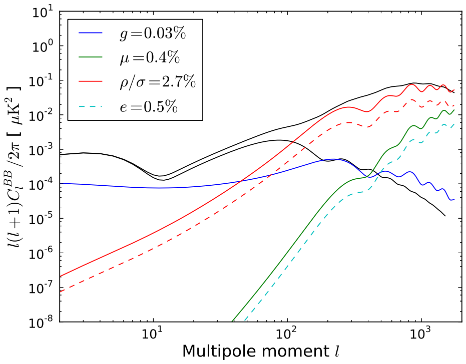

Figure 4.5: The resulting contributions to systematic error signals in C_l^{BB} for the measured differential beam properties. For differential pointing, we've also shown how sky rotation will suppress the effect, as it is the largest contributor. We were not able to make a definitive measurement of differential gain, so we've plotted the required value of $g = 0.03\%$ again for comparison.

4.1.2 $\eta\Delta\nu$ measured with Jupiter

A measurement on the sky takes the form

$$m(\theta,\phi) = \int d\theta' d\phi' B(\theta-\theta',\phi-\phi')T(\theta',\phi') \tag{4.6}$$

where $T(\theta,\phi)$ is the temperature on the sky, $B(\theta,\phi)$ is the beam profile in units of ADC counts per Kelvin. The resulting map $m(\theta,\phi)$ is in units of ADC counts with

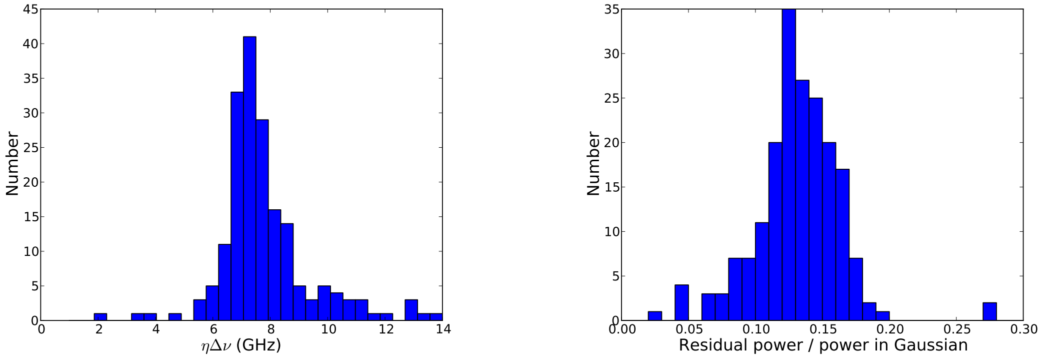

(a) (b)

Figure 4.6: $\eta\Delta\nu$ measured using Jupiter.

the integral taken over the extent of the beam size to properly convolve the beam response. With a planet of extent sufficiently smaller than the beam size Equation 4.6 reduces to

$$m(\theta,\phi) \approx T_p\Omega_p B(\theta,\phi) \tag{4.7}$$

with Ω_p the solid angle subtended by the planet.

A calibration between the detector output, in ADC counts, to Rayleigh Jeans temperature on the sky can be found by considering a beam filling load. In that case, the calibration is given simply by the measured output divided by the known load temperature:

$$\mathrm{g}_{\mathrm{ADC/T}} = \frac{\int d\theta d\phi m(\theta,\phi)}{T_{load}} = \frac{\int d\theta d\phi B(\theta,\phi) T_{load}}{T_{load}} = \int d\theta d\phi B(\theta,\phi) \tag{4.8}$$

In the case of a planet map, the calibration can be found by integrating over the measured map, $m(\theta,\phi)$

$$\int d\theta d\phi m(\theta,\phi) = T_p\Omega_p \int d\theta d\phi B(\theta,\phi) \tag{4.9}$$

The final result is that the calibration from ADC counts to Rayleigh Jeans temperature is given by

$$\mathrm{g}_{\mathrm{ADC/T}} = \frac{\int d\theta d\phi m(\theta,\phi)}{T_p\Omega_p} \tag{4.10}$$

This result is valid when looking at a point source whose spectral emission lies in the Rayleigh-Jeans limit for the detectors. A correction factor can be applied that takes the instrument's spectral response into account for sources that are not in the Rayleigh-Jeans regime for a given detector frequency. Deconvolution of Equation 4.6 must be taken into account for extended sources.

The results of this gain measurement can be converted to the fractional throughput $\eta\Delta\nu$ of the detector if the responsivity is known. Figure 4.6 shows a histogram of the measured $\eta\Delta\nu$, given by

$$\eta\Delta\nu = \frac{\mathcal{L}+1}{\mathcal{L}}\frac{V_{RMS}}{kX}\mathrm{g}_{\mathrm{ADC/T}} \tag{4.11}$$

where we've used responsivity in Equation 2.11. As discussed earlier, the calibration factor X is the overall conversion factor between the RMS carrier current amplitude and DC counts returned by the demodulator. This factor depends on the particular gains used in the dfMux. It's important to note that if detectors are not operating in the high loopgain limit, a correction factor needs to be applied for the operating loopgain. The results shown in Figure 4.6 are consistent with our expectations for the receiver fractional throughput and the 50% NDF used shown in Table 4.1, assuming the actual bandwidths are ~30GHz and using the estimated loopgain of $\mathcal{L} = 4$.

4.1.3 NETs from Jupiter

The measured calibration $\mathrm{g}_{\mathrm{ADC/T}}$ from beam maps can also be used to find the detector NET. Finding the detector noise equivalent counts, NEC, in units of ADC/$\sqrt{\mathrm{Hz}}$ as in Section 3.2, we can find the $\mathrm{NET}_{\mathrm{cmb}}$ from Equation 2.38

$$\mathrm{NET}_{\mathrm{cmb}} = \frac{1}{0.576\sqrt{2}}\left[\frac{\mathrm{NEP}}{k\eta\Delta\nu}\right] = \frac{1}{0.576\sqrt{2}}\left[\frac{\mathrm{NEC}}{\mathrm{g}_{\mathrm{ADC/T}}}\right] \tag{4.12}$$

where the physical calibration constant X/V_{RMS} appears in both the NEC $\rightarrow$ NEP and the $\mathrm{g}_{\mathrm{ADC/T}} \rightarrow k\eta\Delta\nu$ conversions and cancels out. An advantage of this measurement is that no knowledge of the calibration factor X is needed and subtleties with the operating loopgain being smaller than the high loopgain limit don't come into play in the calculation. A timestream and resulting map in whatever the natural readout units happen to be is all that is required to get this overall detector NET.

In figure 4.7(a), we again show the timestream during the Jupiter observation, highlighting subscans away from the planet that were used for the noise floor estimation. The result of this measurement of the NET from the Jupiter beam maps is shown in Figure 4.7(b). The expected NET is shown in Table 4.3 along with contributions from individual noise terms in Equation 2.27. We see that our measurement is in line with expectations for the assumed 29 Kelvin dewar load.

Table 4.1: Estimate of 8.2.0 fractional throughput and dewar loading for the POLARBEAR experiment during the Cedar Flat engineering run.

Element	Termination temperature	Loss or reflection	Cumulative fractional throughput	T_{RJ} referred to primary mirror (K)
Load resistor mismatch	0.5	0%	100%	0
Miscrostrip filter	0.25	8.2%	100%	0
Antenna mismatch	0.25	0%	91.8%	0
Antenna backlobe	0.25	9.0%	91.8%	0
Lenslet surface reflection	0.25	15.0%	83.5%	0
Attenuating filter	5	50.0%	71.0%	4.1
Collimating lens	7	5.0%	35.5%	0.4
Aperture stop truncation	6	13.0%	33.7%	0.7
Aperture lens	7	5.0%	29.3%	0.3
Metal mesh reflection	7	2.0%	27.9%	0.1
Metal mesh absorption	7	2.0%	27.3%	0.1
Field lens	7	5.0%	26.8%	0.3
Metal mesh reflection	7	2.0%	25.4%	0.1
Metal mesh loss	20	2.0%	24.9%	0.4
4K IR shaders	20	2.0%	24.4%	0.4
HWP reflection	25	2.0%	23.9%	0.5
HWP loss	70	2.0%	23.4%	1.6
Metal mesh reflection	50	2.0%	23.0%	1.1
Metal mesh loss	90	2.0%	22.5%	2.0
Teflon filter absorption	90	4.0%	22.1%	3.9
Teflon filter reflection	100	1.6%	21.2%	1.7
77K IR shaders	80	5.0%	21.2%	4.1
300K IR shader	100	1.0%	20.2%	1.0
300K Zotefoam window	300	1.0%	20.0%	3.0
Secondary scattering	200	0.3%	19.8%	0.6
Secondary absorption	300	0.3%	19.7%	0.9
Primary scattering	200	0.3%	19.6%	0.6
Primary absorption	300	0.3%	19.6%	0.9
Total			20.0% $\eta\Delta\nu$ =6.5GHz	28.8

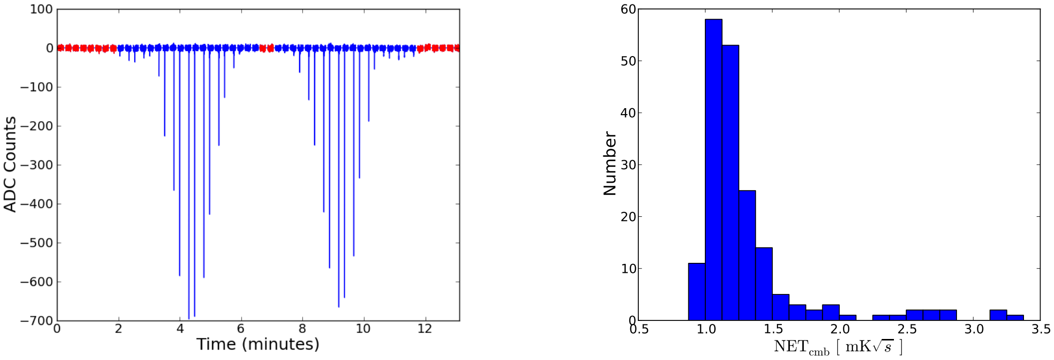

(a) Timestream subscans used for noise estimation are highlighted in red.

(b) Measured NET from Jupiter observations.

Figure 4.7: $\mathrm{NET_{cmb}}$ measured using Jupiter.

Table 4.2: Example measured bolometer properties.

Bolometer property	Value
Bias power P_b	18 pW
$\eta\Delta\nu$	6.5 GHz
Dewar load	29 K
Sky temperature	77 K
Optical power P_{opt}	9.5 pW
Total operating power P_{tot}	27.5 pW

Table 4.3: Expected noise contributions from various noise terms given the example bolometer properties in table 4.2.

Noise component	NEP Contribution ($aW/\sqrt{Hz}$)	NET Contribution (mK $\times\sqrt{s}$)
Photon noise	65	0.9
Phonon noise	39	0.5
Readout noise	32	0.4
Total	82	1.1

4.1.4 Pointing observations

A reliable pointing model of the telescope is necessary to allow us to know the true boresight pointing of the telescope when compared to the commanded values. For certain physical effects, the true boresight pointing can be modeled in terms of telescope mis-alignments and repeatable flexure:

$$\begin{aligned}\Delta az(az_s, el_s) &= -\mathrm{AN}\sin(az_s)\sin(el_s) - \mathrm{AW}\cos(az_s)\sin(el_s) \\ &\quad + \mathrm{NPAE}\sin(el_s) - \mathrm{CA} + \mathrm{IA}\cos(el_s) \\ \Delta el(az_s, el_s) &= \mathrm{AN}\cos(az_s) - \mathrm{AW}\sin(el_s) - \mathrm{IE} + \mathrm{TF}\cos(el_s)\end{aligned} \tag{4.13}$$

where terms in the above equations correspond to the physical effects, described in Table 4.4. In practice, Δaz and Δel are found in offset space, as described earlier. Ideally, maps taken over the full range of azimuth and elevation as different sources traverse the sky should be used to fully characterize the pointing dependence and the accuracy of the model. It is also possible to have non-repeatable aspects to the pointing model such as those due to differential thermal expansion of various structural elements. To help capture and model such effects, we also need to monitor temperatures of structural elements on the telescope.

Table 4.4: Description of terms in pointing model

Parameter	Description
AN	Azimuth axis north of vertical
AW	Azimuth axis east of vertical
NPAE	Elevation axis not perpendicular to azimuth axis
CA	Telescope beam not perpendicular to elevation axis
IA	Azimuth encoder zero-point
IE	Elecation encoder zero-point
TF	Flexure

The results from a single pointing observation using Saturn are shown in Figure 4.8. Each point represents a fit to the planet position at a different azimuth and elevation as the planet moves across the sky. The fit to the model of Equations 4.13 is also shown. Table 4.5 shows the best-fit pointing model terms from several observations made during the Cedar Flat run. The pointing analysis was led by Bryan Steinbach and Stephanie Moyerman.

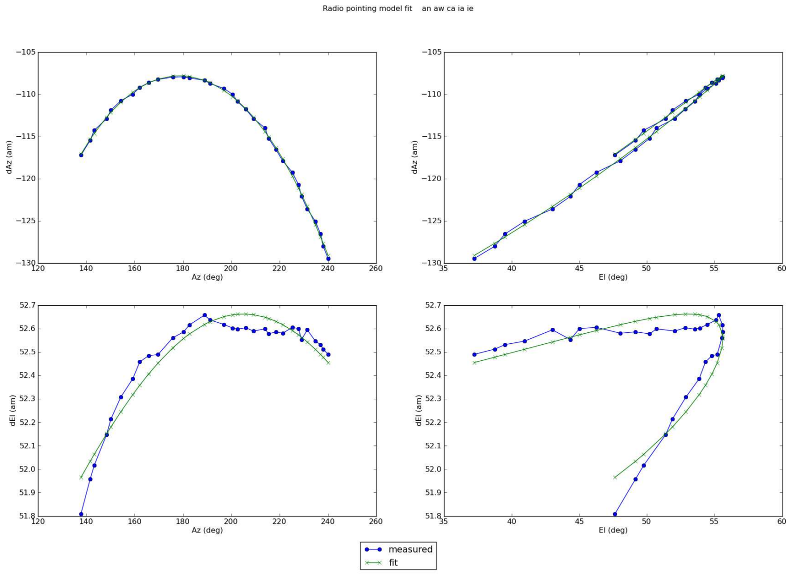

Figure 4.8: Pointing observations of Saturn and the best-fit pointing model. Figure courtesy of Bryan Steinbach.

Table 4.5: The best fit values to the pointing model of Equations 4.13 from a combination of observations of several sources. The RMS of the residuals to the fit is 12.7753 arcseconds.

Parameter	Value (arcseconds)	1 σ error
AN	-0.196	0.0314
AW	-0.0092	0.0251
NPAE	3.9507	0.7012
CA	7.9958	0.8945
IA	6.1837	0.5905
IE	2.3764	0.9107
TF	3.1307	0.5976

4.2 Polarized response measurements

4.2.1 Atmospheric rejection

Quantifying how well the atmospheric fluctuations can be subtracted when differencing the two detectors of a pixel was another important goal of the Cedar Flat deployment. As discussed earlier, the level of $1/f$ knee in the differenced noise spectrum informs our scan strategy and and can possibly limit our ability to measure large scale polarization. Using the fluctuations themselves as a means to relatively gain calibrate pixels, we looked at the power spectral densities of both summed and differenced timestreams.

Figure 4.9 shows the resulting sum and difference timestream NECs for an example pixel during the Jupiter observation used for the above NET analysis. The largest length subset of the timestream when the pixel is pointed away from the planet was used. The gains within a pixel were matched using a linear time-variable gain function for each constant-velocity subset of the scan. Note that the resulting $1/f$ knee is at 115 mHz for the differenced timestream. This poorer performance when compared against lab data taken with a cold load and presented in Section 3.2.2 can be the result of several effects. Electrical noise that remains uncorrelated on a pixel-pair of detectors or inaccurate differential gain calibration are both possibilities that can be addressed, while more fundamental issues such as spectral mismatch between the pixel-pair of detectors could prove to limit our performance.

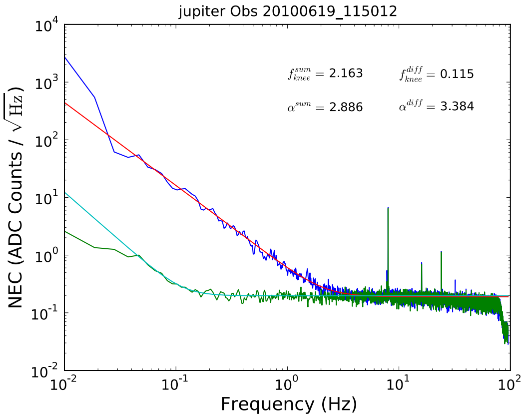

Figure 4.9: Noise equivalent count (NEC) spectral densities for the sum and difference pixel timestreams during a Jupiter observation.

4.2.2 Polarization calibration measurements

The absolute and relative polarization angles of detectors were found using several methods. A Gunn diode coupled to a pyramidal horn was used as a polarized source in the far-field of the telescope. Rotating this source and rotating our HWP allowed us to characterize the polarization sensitivity of the fully assembled instrument, including any effects from the telescope optics. The polarization purity of the Gunn source allowed us to study systematic effects of the HWP itself and measure the polarization efficiency of the entire instrument.

In practice, since the far field Gunn source was located on a nearby mountain at a low elevation, measurements using the source had to be taken using the high transition of the bolometers. The high transition is simply a second, higher T_c aluminum TES placed in series with the standard AlTi bi-layer TES. In normal operation, when the focal plane temperature is kept below the bi-layer transition of $T_c \sim 0.45$ K, the higher T_c TES is simply a superconducting trace that does not adversely effect the lower transition. To use the high transition, we bring the stage temperature above the bi-layer transition to ~ 0.7 K. The low T_c TES is now a resistive element remaining in series with the high T_c TES. Due to its higher T_c, the high transition has a significantly higher saturation power, allowing operation with substantially greater optical loads, such as those from the atmosphere near the horizon. Early wafers were designed with this high transition explicitly to allow such higher loading measurements in the lab and the field.

Results from analysis of these far-field polarization calibration measurements are shown in Figures 4.10(a) - 4.10(e). This analysis, led by Haruki Nishino, indicated that either the HWP thickness was incorrect for our 150GHz detection band or the Gunn diode was not actually operating at 150 GHz. The latter of these two options proved to be the case as the Gunn diode was found to be running at a lower voltage, unstable state, resulting in decreased amplitude and a lower frequency being output. As we'll discuss in Section 5.1.3, subsequent similar measurements done in the lab once the Gunn diode was repaired were able to verify this and verify the proper HWP modulation.

The resulting measurement of the absolute and relative detector polarization angles was used to analyze celestial polarized data with several detectors.

4.2.3 TauA polarized maps

Perhaps the most interesting result from the Cedar Flat deployment is our map of TauA. This polarized source was used as an end-to-end check of the polarized sensitivity of the instrument. Using beam offsets found from planet maps and the polarization angles found from the far field Gunn source measurements, several pixels were coadded to make I, Q and U maps of TauA. Methods to use TauA as a celestial calibrator of polarization angle were also tested using this data. We present here the resulting I, Q, U and polarized fraction, P, maps of TauA at several HWP angles in Figure 4.11. This analysis was led by Haruki Nishino.

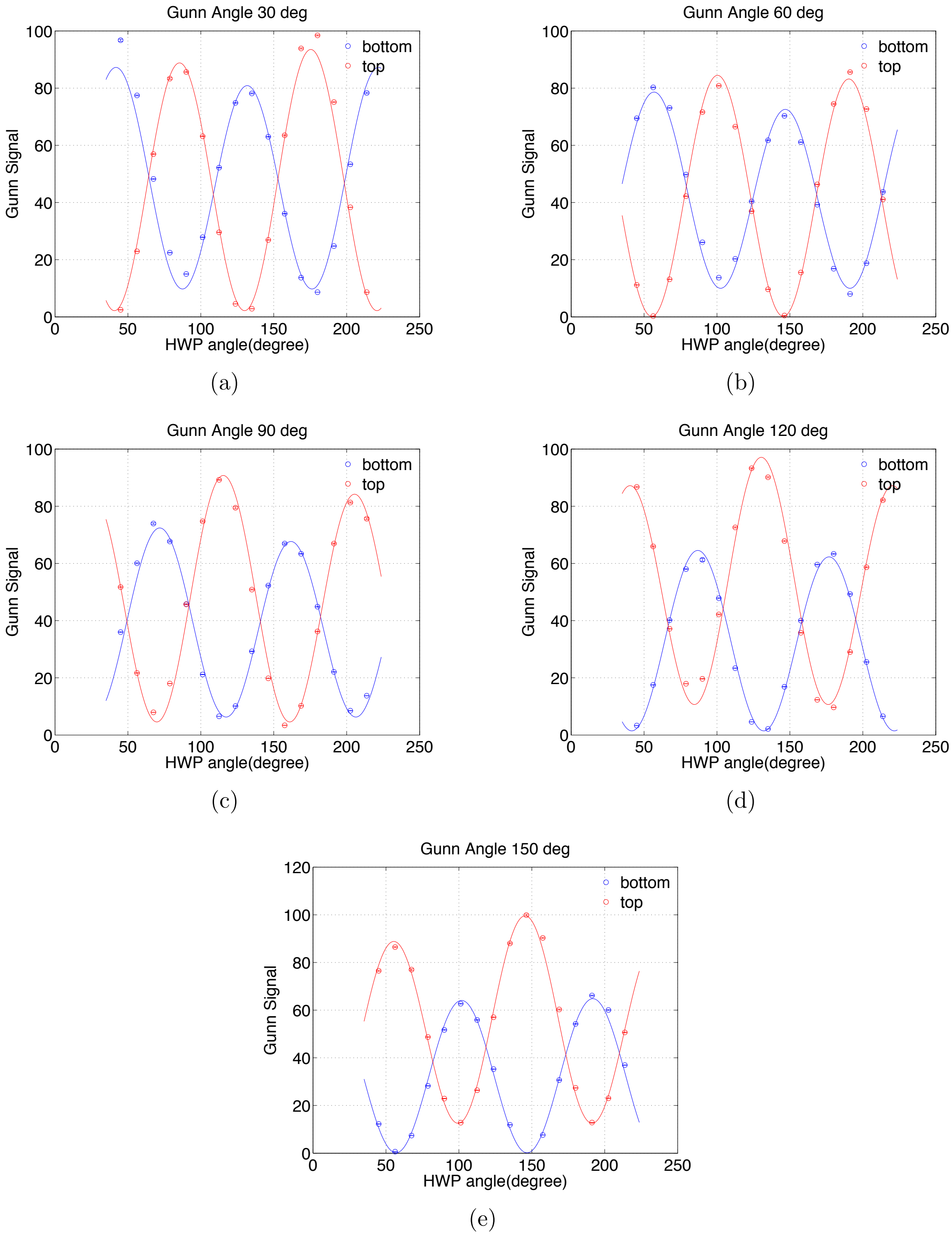

(a) (b)

(c) (d)

(e)

Figure 4.10: Reponse of top and bottom detectors as a function of HWP and Gunn diode angle for an example detector at several Gunn orientation angles. All plots courtesy of Haruki Nishino.

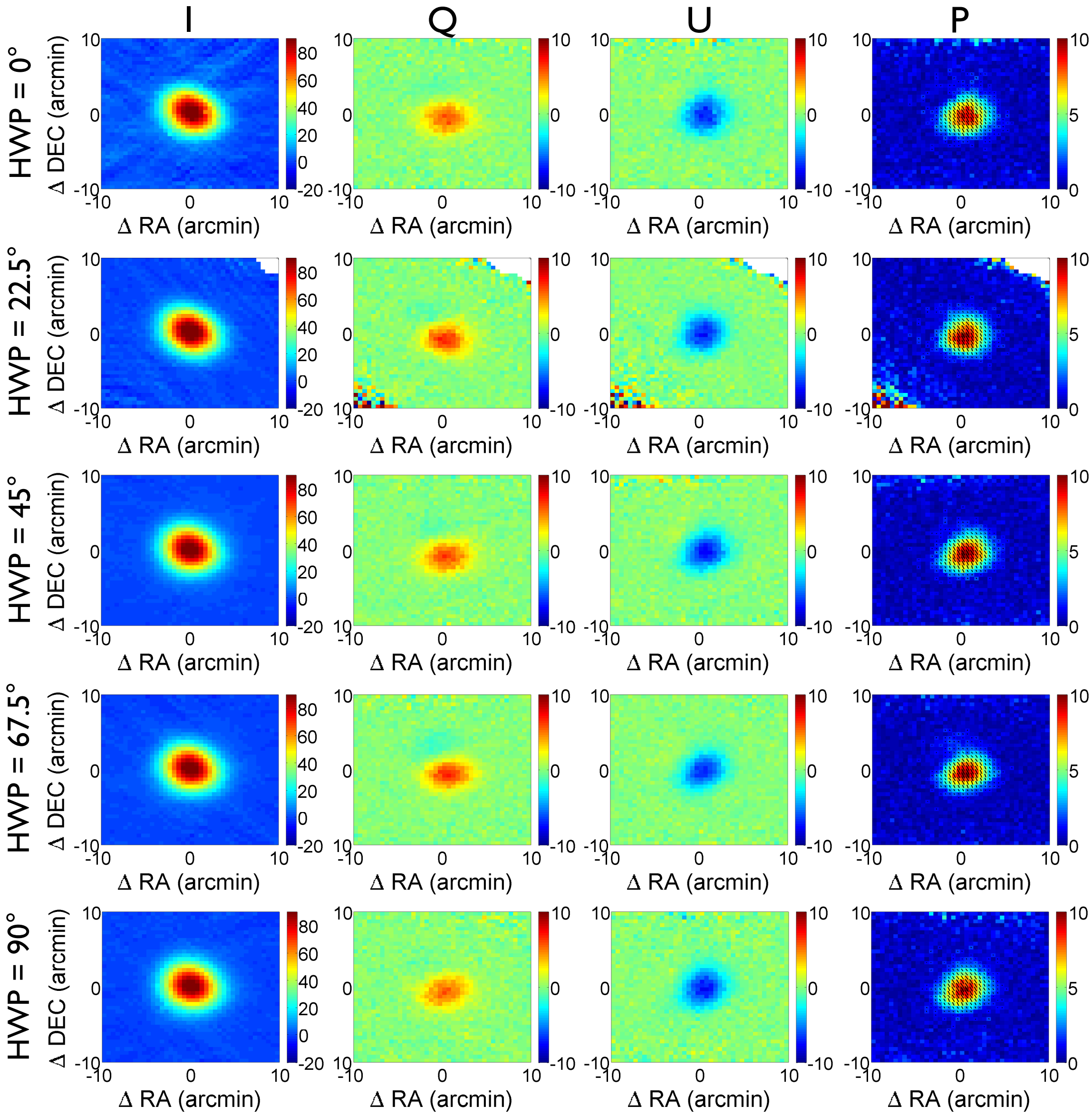

Figure 4.11: I, Q, U and polarized fraction, P, maps of TauA at several different HWP orientations. The P map also indicates the polarization angle. Figure courtesy of Haruki Nishino.

Chapter 5

Preparations for the Chilean deployment

There were several issues remaining that had to be addressed upon returning from the Cedar Flat deployment. Among them was the desire to better understand our dewar load, to run the system without a neutral density filter to see if any optical or cryogenic issues were mitigated by the NDF, and to develop a better understanding of the Gunn diode results presented in Section 4.2.2. Beyond these issues, the full 7 wafer focal plane for Chile had yet to be constructed and characterized.

In Section 5.1, we present measurements taken using the focal plane deployed to Cedar Flat to address the issues discovered. Characterization of the Chilean focal plane is then presented in Section 5.2.

5.1 Cedar Flat configuration revisited

Developing a better understanding of the dewar load was a high priority since the photon noise due to background loading could very well be dominated by the dewar itself and limit our sensitivity in Chile. Since we were still in need of saturation powers for wafers KT8, 8.2.0 and 8.2.1 in the POLARBEAR receiver necessary to understand the dewar load, a run (PCF1) was carried out with a cold load installed attached to the 4K stage just above the focal plane and with the NDF removed. A variable-temperature coldload was chosen over a proper dark run with the focal plane blanked off at millikelvin temperatures to allow us to simultaneously investigate focal plane efficiency and detector responsivity by varying the temperature of the load.

5.1.1 Out of band excess power

Initial measurements of $\eta\Delta\nu$ from the focal plane to the load using the cold load at temperatures of 6 Kelvin and 6.5 Kelvin provided inconsistent results. A non-physical fractional throughput greater than 1 was being calculated using the standard analysis previously used and presented in earlier chapters. This issue was quickly attributed to excess power outside of the detector band. The power seen is degenerate with several mechanisms: wafer heating due to a relatively large emissivity of the silicon device wafer or lenslet array, spectral leaks in the microstrip filters allowing in out of band power, or direct stimulation of the bolometer island, which would again present itself as out of band power but most likely with a diffuse or off-axis beam. Such excess power didn't appear as a large effect in earlier measurements since the NDF was in place and the resulting change in loading seen by the wafers was small.

A method was devised to enable removal of this excess power and extraction of the optical power on the bolometers for two of these possibilities: direct bolometer stimulation and wafer heating. We carried out another run (PCF2) with the focal plane now blanked off at millikelvin to assure essentially zero optical power. We then varied the base temperature of the stage and took IV curves to get the saturation power as a function of the bath temperature, T_b. Assuming the conduction along the weak thermal link is dominated by phonon conduction, we can fit to a model $P_{sat}(T_b)$ using

$$P_{sat}(T_b) = \frac{k_{phon}}{4}\left(T_c^4 - T_b^4\right) \tag{5.1}$$

The transition temperature T_c can either be found via direct measurement or a fit from the data of $P_{sat}(T_b)$.

Each focal plane has several 'dark' or 'antenna-less' bolometers that are not coupled to an antenna or microstrip filters. In this way, the antenna-less bolometers are useful probes of the excess power being deposited on the wafers. Using a fit to the individual bolometer model, we can solve for the bath temperature which gives $P_{sat}(T_b) - P_{elec} = 0$ for the antenna-less bolometers during an optical run. Data and fits from such a measurement are shown in Figures 5.1(a) and 5.1(b). Since antenna-less detectors should receive no in-band optical power, the T_b that solves this equation represents the physical wafer temperature if the only effect is wafer heating due to large wafer emissivity. In the case of out of band response due to direct stimulation, this simply parametrizes the excess power. Spectral leaks in the microwave or optical filters would not be corrected for with this method as there is no optical power going through the standard optical-microwave chain with the absence of an antenna. The fractional throughput bandwidth product $\eta\Delta\nu$, dewar load and effective Rayleigh-Jeans temperature of the dewar can then be found as usual, where we now explicitly keep track of the saturation power as a function of bath temperature

$$\eta\Delta\nu = \frac{P_{sat}(T_b^{300K}) - P_{sat}(T_b^{77K}) - \left(P_{elec}^{300K} - P_{elec}^{77K}\right)}{k\Delta T} \tag{5.2}$$

$$P_{dewar} = P_{sat}(T_b) - P_{elec} - \eta\Delta\nu k T_{load} \tag{5.3}$$

$$T_{RJ} = \frac{P_{dewar}}{k\eta\Delta\nu} \tag{5.4}$$

where we've used the measured electrical power on optical bolometers and inferred bath temperature from dark bolometers in runs with a 300 K and 77 K load to determine $\eta\Delta\nu$. The dewar load can then be calculated using either load temperature. Of course, this result generalizes for any two temperature loads.

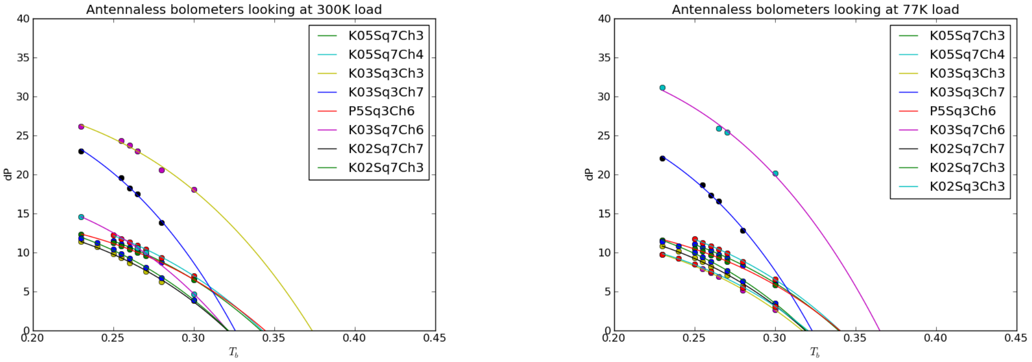

(a) Data and fits to $P_{sat}(T_b) - P_{elec}$ for antenna-less detectors looking at a 300 Kelvin load. The 0 intercept of the curves gives the inferred bath temperature for the case of wafer heating being responsible for the excess power.

(b) Data and fits to $P_{sat}(T_b) - P_{elec}$ for antenna-less detectors looking at a 77 Kelvin load. The 0 intercept of the curves gives the inferred bath temperature for the case of wafer heating being responsible for the excess power.

Figure 5.1: $P_{sat}(T_b) - P_{elec}$ for antenna-less detectors.

Any errors on the power measured would contribute to errors on $\eta\Delta\nu$ and T_{RJ} with scalings given by

$$\delta(\eta\Delta\nu) = \frac{\delta P}{k\Delta T} = \left[0.32\frac{GHz}{pW}\right]\delta P \tag{5.5}$$

$$\delta T_{dewar} = \frac{\delta P}{\eta\Delta\nu k} = \left[5.57\frac{Kelvin}{pW}\right]\delta P \tag{5.6}$$

where we've used ΔT =233 Kelvin when using a 300K and 77K load and the expected fractional throughput bandwidth product of $\eta\Delta\nu \sim 13$ GHz.

If we assume these errors in measured power are dominated by how well we constrain the bath temperature, or equivalently how well we measure and parametrize the excess power, the errors are given by

$$\delta\left(\eta\Delta\nu\right) = \left|\frac{dP}{dT_B}\right|\frac{\delta T_b}{k\Delta T} \tag{5.7}$$

$$\delta T_{dewar} = \left|\frac{dP}{dT_b}\right| \delta T_b \frac{1}{\eta \Delta \nu k} \tag{5.8}$$

Assuming a conservative constraint on δT_B of 40 milliKelvin and using the measured mean $dP/dT_b \sim 30pW/K$, this implies less than 0.5 GHz errors on $\eta\Delta\nu$ for a measurement using 300K and 77K loads and a 7 Kelvin error on T_{RJ}.

This method was applied to the cold load measurements with temperatures of 6 Kelvin and 6.5 Kelvin from the earlier PCF1 run. Results for $\eta\Delta\nu$ are shown in Figure 5.2 and are consistent with expectations for the fractional throughput. Figures 5.3(a) and 5.3(b) show the resulting measured load temperature and are consistent with the expected errors given our knowledge of the bath temperature, as shown in Table 5.1.

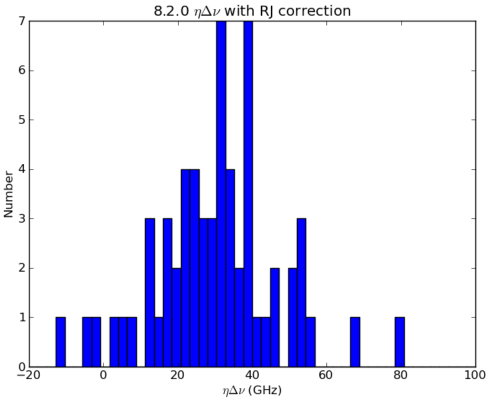

Figure 5.2: The measured $\eta\Delta\nu$ between the focal plane and coldload found when accounting for excess out of band power.

Table 5.1: Results from measurements of dewar load and $\eta\Delta\nu$ using a 6 Kelvin and 6.5 Kelvin coldload directly in front of the focal plane. Excess out of band power effects were accounted for using the method described in section 5.1.1

Load temperature (Kelvin)	Expected T_{RJ} (Kelvin)	Mean T_{RJ} measured (Kelvin)	Measured $\sigma_{T_{RJ}}$
6.47	3.52	3.63	0.78
5.99	3.09	3.30	0.91

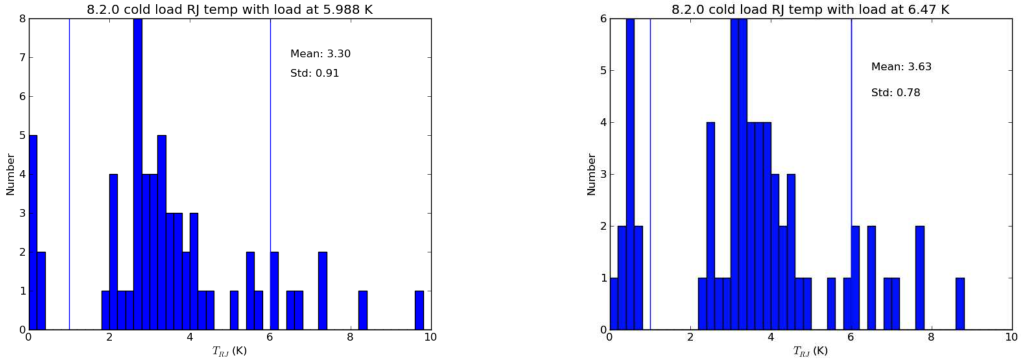

(a) 6.5 Kelvin cold load inferred RJ temperature

(b) 6 Kelvin cold load inferred RJ temperature.

Figure 5.3: Inferred T_{RJ} of coldload at temperatures of 6 Kelvin and 6.5 Kelvin

5.1.2 $\eta\Delta\nu$ and T_{RJ} measured with high transition

With the neutral density filter removed and the focal plane open to the room in the next run (PCF3), we used the methods described in the previous section to measure both $\eta\Delta\nu$ and T_{RJ} of the receiver. Without the ND in place, the optical load from 77 Kelvin saturates the low transition of the detectors, so using the high transition was necessary. The results from this measurement are shown in figures 5.4(a) and 5.4(b).

These results are both consistent with an error in the measured power of $\delta P \sim 10$ pW. This is not an unreasonable expectation for the high transition since saturation powers are on the order of 1000 pW and readout stability and parasitics might be an issue. The measurement of $\eta\Delta\nu$ is also consistent with expectations of 13GHz from a detector bandwidth of 32 GHz and fractional throughput of 41 percent. This result is also consistent with the results from Cedar Flat, verifying the expected 50% attenuation of the NDF used during the engineering run.

The mean of the distribution for the dewar load measurement is significantly higher than expected. This can be attributed to some combination of spectral leaks in the optical chain resulting in in-band power or direct stimulation or out-of band response not accounted for by our measurement of power on antenna-less bolometers. It was also realized that a feedthrough port in the 4 Kelvin optical tube was not properly covered during close-up, leaving a ~0.25 inch diameter 80 Kelvin hole staring at the focal plane with no filtering, so spectral leaks were a clear candidate.

All possibilities were addressed by adding a 5.6icm filter just above the focal plane and covering the feedthrough port in the next run (PCF4). While errors remained large since this was still a high-transition measurement, a substantial decrease in the mean of the distribution was found, as shown in figure 5.5(b)

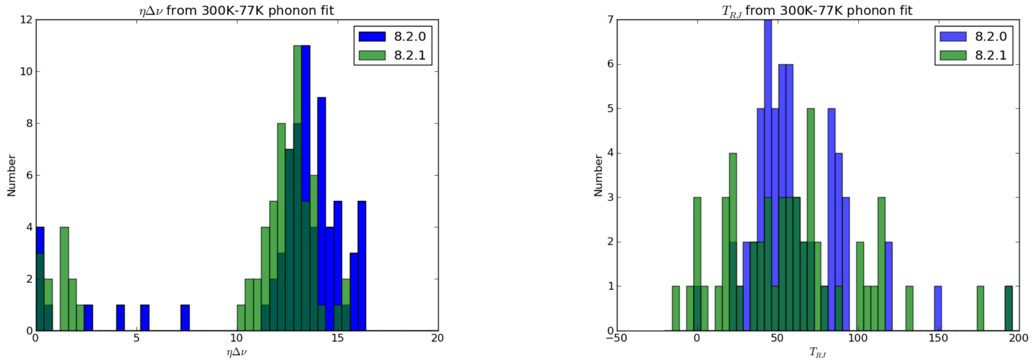

(a) $\eta\Delta\nu$ as measured using a 300 Kelvin and 77 Kelvin beam-filling cold load at the receiver window

(b) T_{RJ} as measured using a 300 Kelvin and 77 Kelvin beam-filling cold load at the receiver window.

Figure 5.4: Chopped cold load measurements.

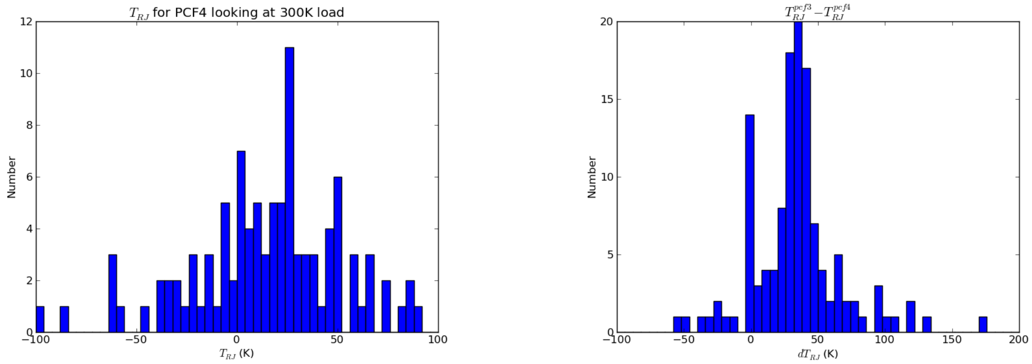

(a) T_{RJ} dewar load measured using the high transition and a beam filling load chopped between 300K and 77K.

(b) The difference in T_{RJ} between runs PCF3 and PCF4 taken on a bolometer by bolometer basis.

Figure 5.5: The dewar load measured in PCF4 using a beam filling 300K to 77K chop. Compared to PCF3, a clear improvement can be seen from the repaired light leak at the optics tube.

While a more definitive measurement of the dewar load could have been made using the low transition where errors would be smaller and the spread in distributions of T_{RJ} would be lower, this required the development of a 4 Kelvin cold load. While efforts began to construct such a cold load using a separate pulse tube cooler, this load was not constructed in time to be used in the PCF4 run.

5.1.3 Polarization calibration measurements

We also revisited polarization calibration measurements using the Gunn diode source and detectors in the high transition during the PCF4 optical run. The main motivation of these measurements was to verify the performance of the HWP after the Gunn diode was repaired and its operating frequency confirmed. Measurements were taken with the Gunn diode source in the near field of the receiver. Figures 5.6(a) - 5.6(d) show the response measured in an example pixel pair for several gunn and HWP angles. The analysis of this data, again led by Haruki Nishino, verified our expectation that the HWP was behaving properly and that the issues seen in the Cedar Flat data was due to the Gunn diode's instability. However a separate issue was discovered in analyzing this data.

The level of expected crosstalk from detectors on the same mux set increases when working in the high transition compared to the low transition simply because the TES resistance is higher. The amount of cross talk can be estimated by calculating how much bias current from the detector of interest leaks down neighboring channels, and how much bias current from neighboring channels leaks into the modulated bias current of the detector of interest. The result for a channel i due to neighboring channels n is

$$\frac{\delta I_n}{\delta I_i} = \sum_{n\neq i}^{\text{comb}} \frac{I_n}{I_i}\frac{dR_n/|Z_n|}{dR_i/|Z_i|} + \sum_{n\neq i}^{\text{biased}} \frac{I_i}{I_n}\frac{dR_i/|Z_i|}{dR_n/|Z_n|} \tag{5.9}$$

$$\approx \sum_{n\neq i}^{\text{comb}} \frac{R_i^2}{R_n^2 + L^2\left[2\pi f_i(1-(f_n/f_i)^2)\right]^2} + \sum_{n\neq i}^{\text{biased}} \frac{R_n^2}{R_i^2 + L^2\left[2\pi f_n(1-(f_i/f_n)^2)\right]^2} \tag{5.10}$$

where L is the inductor value and f_n, Z_n and R_n are the resonant frequencies, complex filter impedances, and bolometer resistances on a comb. The first sum is the crosstalk due to the current leakage of the bias of interest into all neighboring combs, the second sum the leakage from all neighboring biases into the resonant circuit of interest. Note that only a single bias frequency is needed for contributions from neighboring detectors to the first term. The approximation assumes that $dR_n/dR_i = 1$.

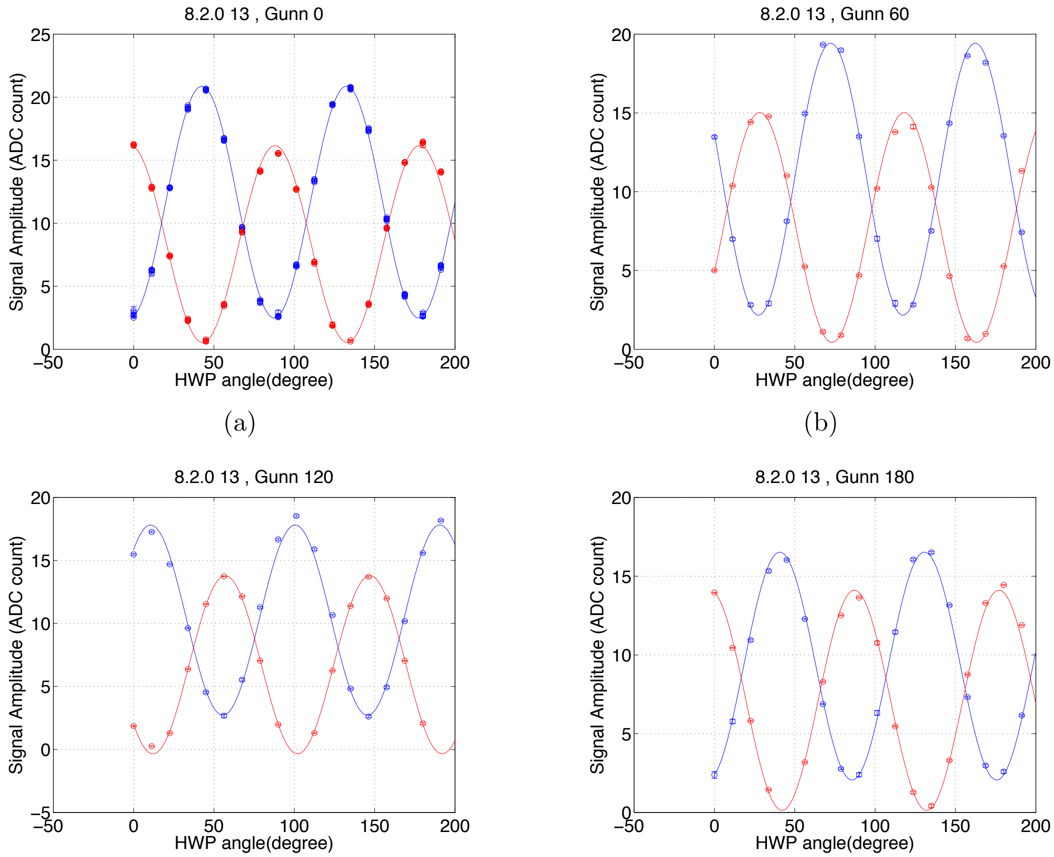

(a) (b)

(c) (d)

Figure 5.6: Measured polarized response for bottom (blue) and top (red) detectors of a pixel at several Gunn diode and HWP rotation angles. Figures courtesy of Haruki Nishino.

Practical limitations in the available output of the dfMux carrier synthesizers allowed us to only bias 4 of the 8 possible channels on a comb for simultaneous operation in the high transition. This resulted in the unexpected outcome that bolometers with unbiased detectors on the same comb nearby in frequency had higher crosstalk than those with biased detectors. These are shown as the higher outliers from the expected crosstalk shown as the line in Figure 5.7. While a detailed study wasn't carried out at the time, these can most likely be explained by the fact that the approximation of $dR_n/dR_i = 1$ is invalid when bolometers are left unbiased and at substantially different locations in their $R(T)$ curves then their biased neighbors. More appropriate modeling of the change of the neighboring channel resistance R_n in the first sum of Equation 5.9 is required to have a more accurate estimate. This added complication in using the high transition moved us away from making measurements using it when possible.

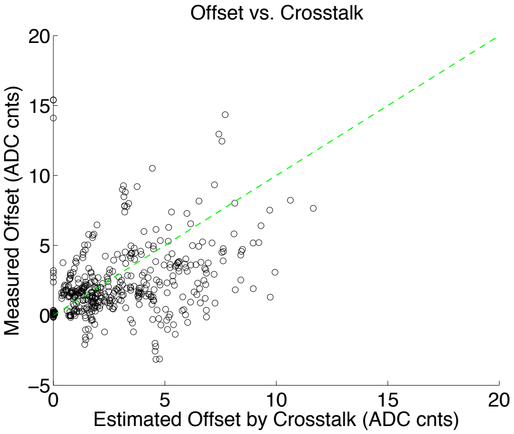

Figure 5.7: Estimated versus measured crosstalk in the high transition. Figure courtesy of Haruki Nishino.

5.2 Chile focal plane characterization

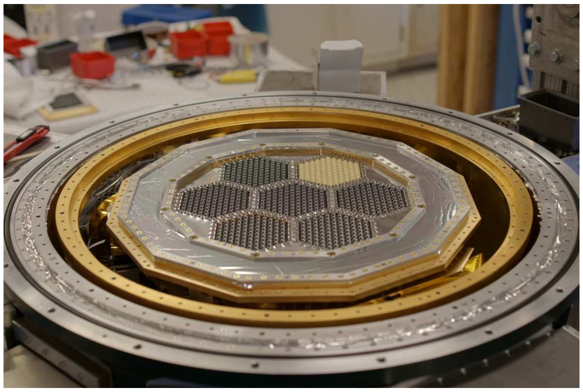

Figure 5.8: The Chile focal plane installed in the POLARBEAR receiver.

Several candidate wafers were produced while characterization of the Cedar Flat focal plane and upgrades to the receiver were being performed. Individual witness pixels and a subset of detectors on some single wafers were tested from both the 10 series and 9 series of wafers. A candidate focal plane consisting of wafers 10.1, 10.2, 10.3, 10.4, 10.5, 9.4 and 8.2.0 was assembled, shown in Figure 5.8. These wafers were considered the most likely to deploy due to measurements of detector saturation powers and spectral bands from witness pixels. The wafers were not fully characterized, so a characterization of the entire focal plane in the POLARBEAR receiver was needed. A dark run (PCF6) was carried out with full readout of the 7 wafer focal plane to measure the saturation powers of the detectors as a function of temperature. This was followed by an optical run (PCF7) to characterize $\eta\Delta\nu$, NETs, and measure spectral response. The optical run was conducted without a neutral density filter in place, so a cold load capable of reaching temperatures below ~ 40 Kelvin was required to investigate detector performance in the low transition.

5.2.1 Saturation powers

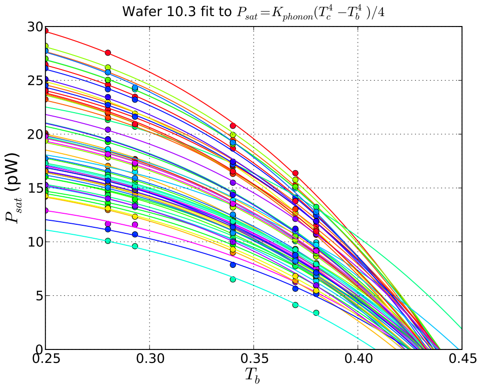

Figure 5.9: Measured saturation powers as a function of bath temperature and best fit curves to Equation 5.11 for wafer 10.3.

Saturation powers of all detectors were measured during PCF6 at several base temperatures to enable later characterization of the wafer temperature when the optical chain was open to the room. The PCF6 run ensured negligible optical load on the detectors by installing a blackened plate just above the focal plane attached to the 350 mK stage. Results for the saturation power as a function of temperature for an example wafer are shown in figure 5.9. Rather than assuming phonon dominated conduction, we were able to directly fit to the conductivity index, n and the thermistor T_c from

$$P_{sat}(T_b) = \frac{k_0}{n+1}\left(T_c^{n+1} - T_b^{n+1}\right) \tag{5.11}$$

The results are shown in figures 5.10(a) and 5.10(b) for all wafers. The conductivity index is consistent with phonon dominated conduction with $n \sim 3$, and T_c values match those found by varying the stage temperature slowly and looking for the increased current flow when a small voltage bias is applied.

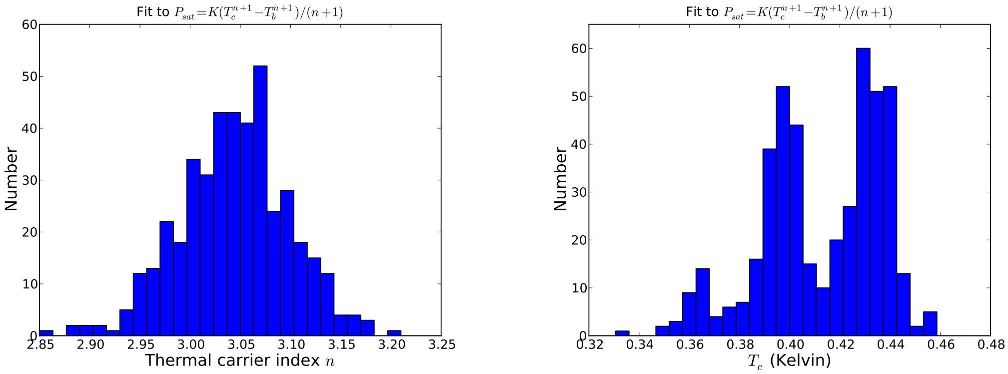

(a) Histogram of fit conductivity index n for all wafers.

(b) Histogram of fit T_c for all wafers.

Figure 5.10: Conductivity index n and transition temperature T_c found by fitting to Equation 5.11

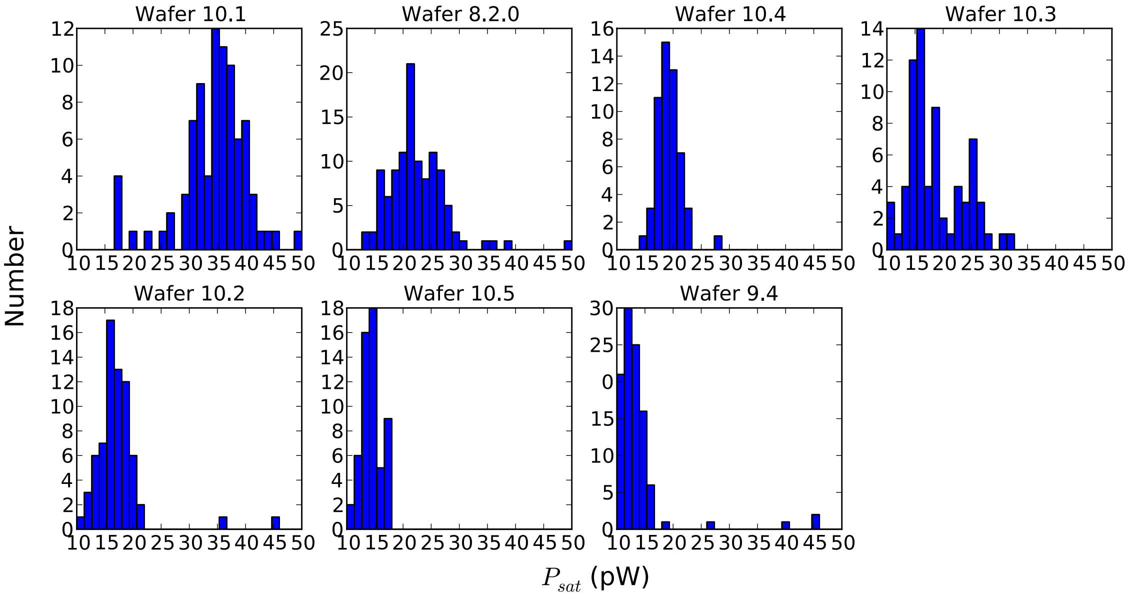

Figure 5.11: Histograms of dark turnaround powers for each wafer with a 0.25K stage temperature as measured during the PCF6 dark receiver run.

Histograms of the dark saturation powers measured at the coldest temperature are plotted for each wafer in figure 5.11. The range of saturation powers is such that we have two conservative wafers (10.1 and 8.2.0) with high saturation powers compared to our design spec of 16 picoWatts, and two that are slightly more aggressive (10.5 and 9.4). The focal plane will therefore give us more information from data on the sky to help better optimize the tradeoff between noise performance and load capability in planned upgrades to the receiver with future arrays.

5.2.2 Band measurements

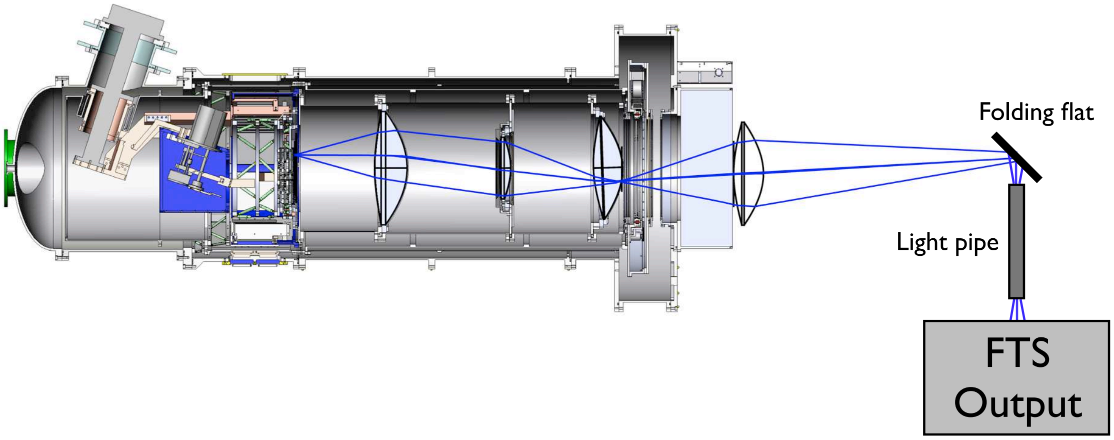

Figure 5.12: Setup of the beam-filling FTS measurements.

As discussed earlier in Section 3.3, previous measurements of the spectral bands of detectors did not have the FTS output filling the input beam of the detectors. We believe this set up a Fabry-Perot resonator at the silicon lenslets, resulting in the deeply fringed spectra measured. For the PCF7 run, we employed techniques developed on smaller test receivers to properly fill the detector beam with the output of the FTS. As shown in Figure 5.12, a reimaging lens just outside the receiver window was used to refocus the diverging beam into a light pipe. This light pipe was then used to translate the focus of the FTS output to match the input beam at the receiver. Note that the reimaging lens needs to be repositioned and the optimum focus remapped for every different pixel positions on the focal plane. In practice, we only measured the spectrum for pixels near the center of each wafer, so we used seven lens and focus positions. Measurements had to be carried out using the high transition.

Results from the measurements are shown in Figure 5.13. We present the average spectrum for each wafer, using both top and bottom detectors from whatever pixels were measured. Note that there was a polarization dependence of the FTS seen in the differential response between top and bottom detectors that we're not presenting here. This is not unexpected given the polarization dependence of the dielectric sheet beam-splitter, however the level of this differential response was not fully investigated. To assure that any differential response at the detector level not due to the measurement method is accounted for in the final science analysis, a more careful spectral band characterization is needed. This measurement is planned to be carried out on the telescope, using the secondary mirror and a larger throughput FTS to aid in properly beam-filling the detectors.

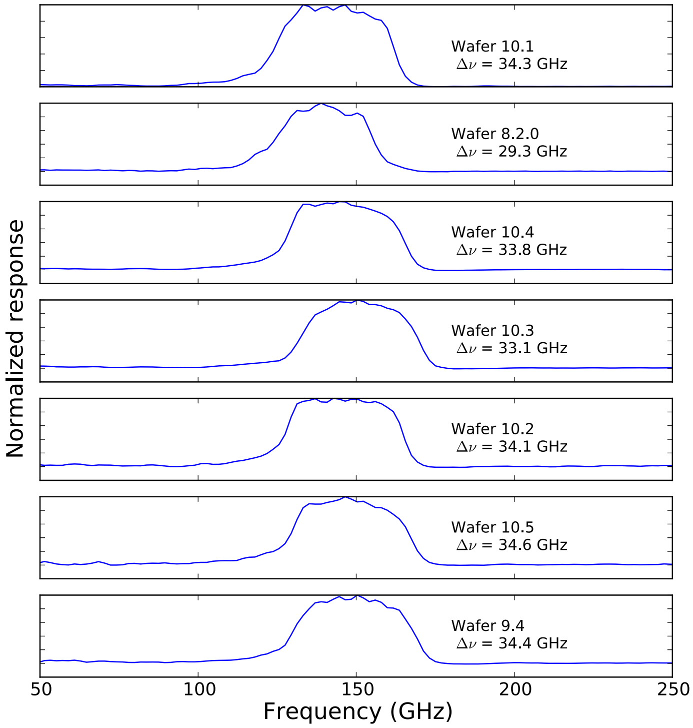

Figure 5.13: Averaged wafer spectra measured with the beam filling setup illustrated in Figure 5.12.

The results shown in Figure 5.13 let us know that our band placement was appropriate for the 150 Ghz atmospheric observing window. Nominal detector loading and NETs calculated given the band edges and band width indicated excellent performance, even for the slightly lower band center wafers. A slight hit in performance was expected from wafer 8.2.0 given that it has both a lower band center and narrower band width.

5.2.3 Cold load measurements

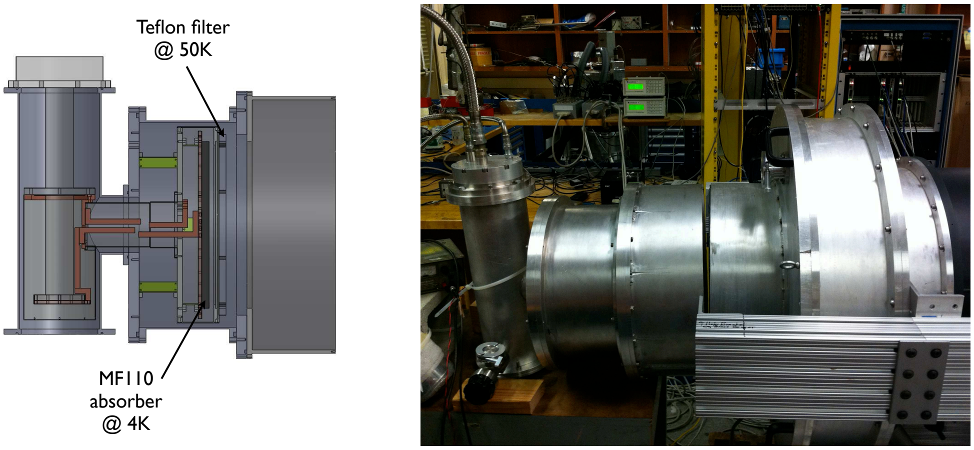

(a) CAD drawing of the pulse tube cooled coldload.

(b) Setup for measurements with the pulse tube coldload at the POLARBEAR receiver window.

Figure 5.14: CAD drawing of the pulse tube cooled coldload (a) and a photograph of it in use at the receiver window (b).

A pulse-tube cooled coldload was constructed out of spare parts to enable measurements of noise and fractional throughput in a reduced loading environment. A CAD drawing illustrating the constructed coldload is shown in Figure 5.14(a). A simple solid teflon filter was attached to the 50 Kelvin stage of the pulse tube to help absorb IR radiation and prevent it from heating the MF110 absorber attached to the 4 Kelvin coldhead. While the hope was to bring the effective temperature of the coldload below 20 Kelvin to produce loading similar to the Chilean sky temperatures expected, we were not able to verify that the effective load temperature reached this goal. The MF110 absorber attached to the 4 Kelvin coldhead was cooled to $\sim$12 Kelvin at its center. Measurements that compared the response of a single test bolometer using a DC SQUID readout system between a chopped 77 Kelvin load and the cold load indicated the effective temperature at the center of the load reached $\sim$ 30 Kelvin. This suggested either the teflon filter was heating substantially near the center, contributing to the larger total effective temperature, or reflections in the system were causing rays to terminate on warmer objects in the cold load receiver.

The photo in Figure 5.14(b) shows how the coldload was used with the POLARBEAR receiver during the PCF7 run. Aligning both the receiver and coldload windows allowed the largest amount of the beam to reach the coldload from all focal plane positions. For the pixels further from the center, a substantial amount of the beam was truncated by the warm aperture of the vacuum window of the cold load. This would contribute to an even higher effective load temperature seen by these detectors.

Despite these limitations, we measured $\eta\Delta\nu$ and NETs from the bolometer response to a small change in the coldload temperature. Our lack of knowledge on the precise beam illumination of the coldload for all detectors means we'd expect reduced fractional throughput and increased noise measurements compared to naive expectations. Beyond that, our inability to accurately measure the effective coldload temperature prevented us from making quantitative predictions for the expected NET, even for pixels well centered in the array that might feasibly be beam-filled by the load. The goal of these measurements was therefore simply to see an improvement in noise performance compared to the Cedar Flat measurements and trends consistent with the expected radial dependence of both the NET and fractional throughput. The measured $\eta\Delta\nu$ measured near the center should be an accurate representation of the receiver given ray tracing simulations.

Figure 5.15(a) shows a set of timestreams on a comb as the coldload absorber temperature is changed from 9.068Kelvin to 9.797 Kelvin. The known ΔT and the DC change in the timestream are used to calculate $\eta\Delta\nu$ according to Equation 4.11. Similar to our planet measurements during the Cedar Flat run, using the noise level of the timestream, we can calculated the NET independent of calibration factors and knowledge of the loopgain. The results for $\eta\Delta\nu$ and the NETs are shown in Figures 5.15(b) and 5.15(c). Note that we've highlighted the center wafer 10.2 in both plots. As expected, wafer 10.2 has a higher $\eta\Delta\nu$ of $\sim$ 14GHz, consistent with expectations while the edge wafers and the array as a whole has a lower mean fractional throughput. The center wafer also has the lowest NET, as expected, with a peak near 650 $\mu K\sqrt{s}$.

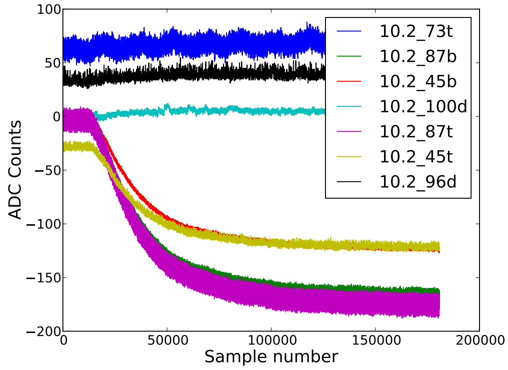

(a) The resulting timestreams on a comb from a step in the coldload temperature of ~ 0.7 Kelvin.

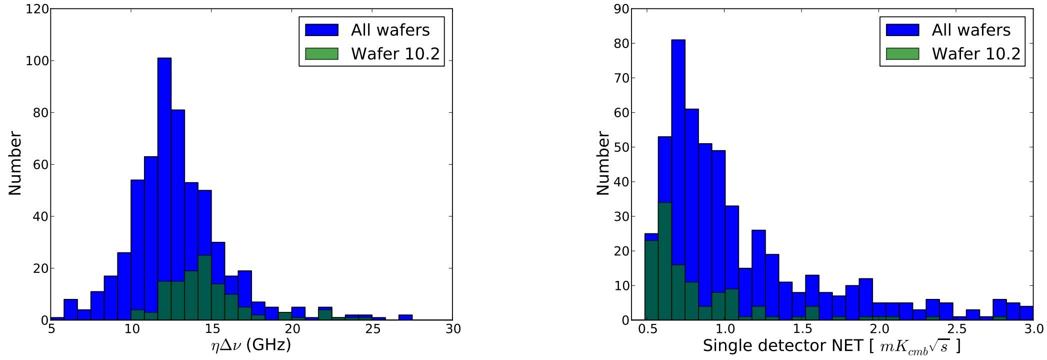

(b) $\eta\Delta\nu$ measured from the timestream in Figure 5.15(a) and the known ΔT and bolometer bias parameters.

(c) NET measured using the timestream in Figure 5.15(a).

Figure 5.15: Measurements of $\eta\Delta\nu$ and NETs using the pulse tube cooled coldload.

Chapter 6

The Chilean deployment

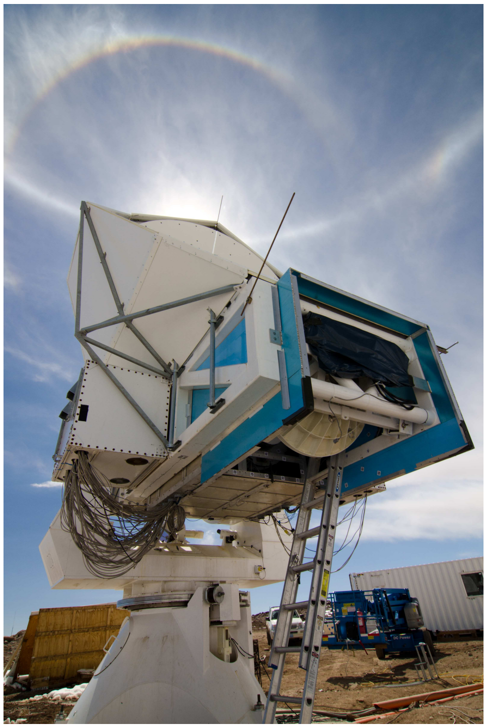

Figure 6.1: The POLARBEAR experiment installed in the Atacama Desert of Chile. Photo courtesy of Nathan Stebor.

While the receiver and candidate focal plane were being characterized in the Berkeley lab, efforts were underway to move the Huan Tran Telescope to the Atacama dessert in Chile and begin construction of our site and necessary infrastructure. Despite delays in construction due to weather and the relocation of the proposed Chilean site, the major components of the telescope and most of the needed infrastructure were installed in Chile by late October of 2011. At this point, the lab characterization presented in Section 5.2 had validated the saturation powers and spectral bands of the candidate wafers to be near our design goals for the Chilean sky. The noise characterization using the coldload provided limited insight into the expected array sensitivity in Chile given the unknown load temperature. The decision was made to deploy the receiver and proceed with noise characterization on the Chilean sky.

The receiver was disassembled, packed, and shipped to Chile in early November. It was reassembled and cooled down in a lab container in Chile before being mounted on the telescope. A 'first light' of sorts was achieved with the non-reimaged receiver beams directed to the sky and detectors seeing turnarounds in their IV curves on December 22, 2011. First light with the receiver installed on the telescope was achieved in the first week of January, 2012. A combination of beam maps using planets and photogrammetry of mirror surfaces revealed that the telescope's primary mirror was being deformed by stresses in its mount. The deformation of the primary mirror was severely limiting the telescope's performance. Significant effort was put into relieving these stresses to bring the mirror surface back to the desired shape within the required accuracy. After addressing these issues and aligning the other elements of the telescope, focus was achieved with diffraction-limited beams in the first week of March.

Characterization of the instrument is still an ongoing endeavor as we are currently moving towards regular science observations in Chile. In this Chapter, we present the current status of this characterization, focusing on results from planet observations in Section 6.1, and from nominal science scans of blank sky and galaxy patches in Section 6.2.

6.1 Planet maps

As discussed in Section 4.1, maps of sources significantly smaller than the beam size can be used to characterize many aspects of the instrument. We made measurements with planets similar to those done during the Cedar Flat deployment to characterize our detector beams. As before, these measurements allowed us to investigate the level of differential beam asymmetries, coadd all pixels for high fidelity maps of the overall instrument beam, and quantify detector sensitivities.

6.1.1 Detector beam properties and the instrument beam

The Gaussian fits to all active detectors during a recent Saturn scan are shown in Figure 6.2(a), with histograms of the individual detector beamwidths and ellipticities shown in Figures 6.2(c) and 6.2(d), respectively. Its clear from Figure 6.2(a) that a significant fraction of the detectors are not yet operational. This particular scan had

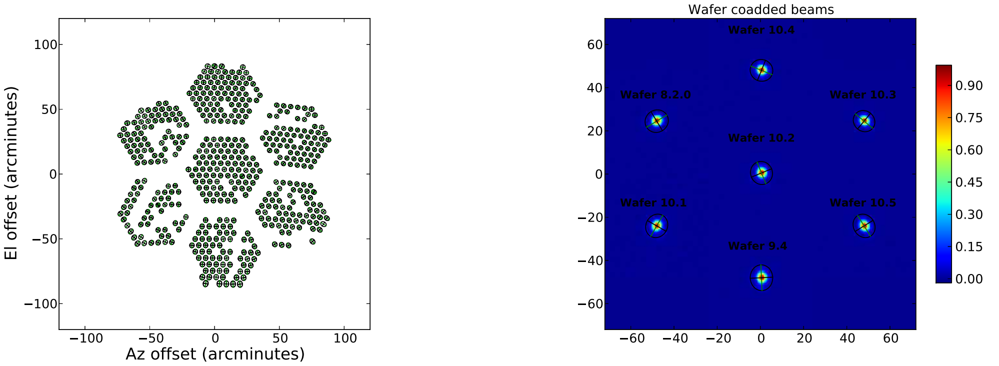

(a) Gaussian fits to detector beams (b) Co-added effective wafer beams.

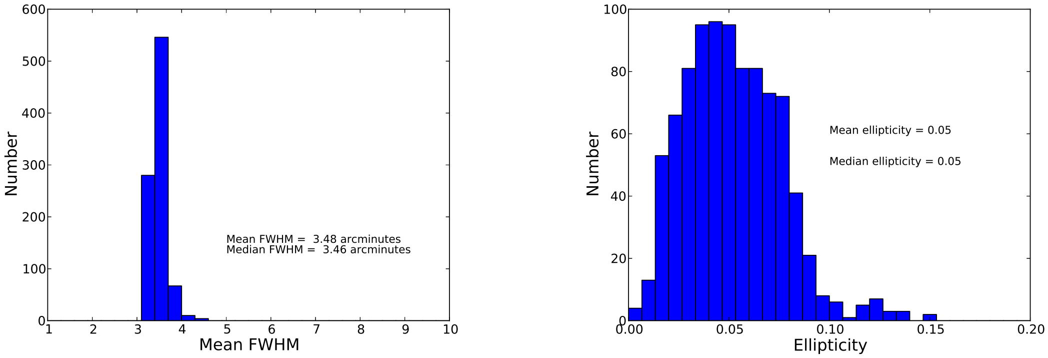

(c) Measured beam widths (d) Measured beam ellipticities

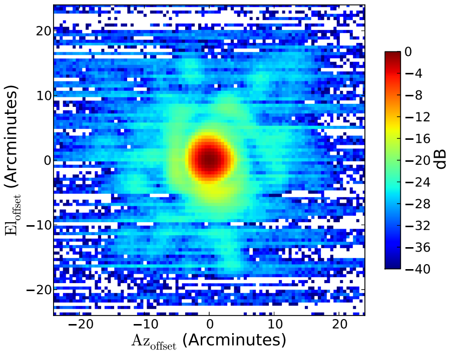

(e) Co-added instrument beam

Figure 6.2: Beam characterization in Chile.

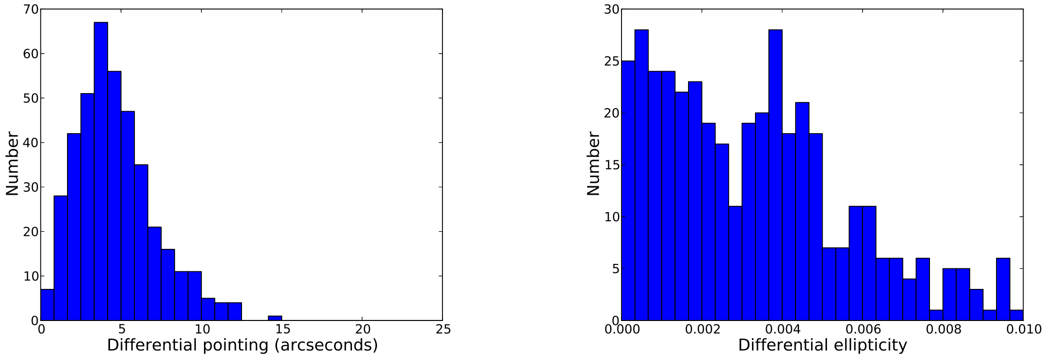

(a) Differential pointing measured in Chile.

(b) Differential ellipticity measured in Chile.

Figure 6.3: Differential beam properties measured in Chile.

906 beam fits returned, or ∼70% of the ideal yield of 1274 optical detectors. From all combined observations, we currently have beam fits for ∼1000 detectors. This is nearing the expected yield of 85% given cold measurements of network analyses from multiplexer combs. Channels are currently being lost for a variety of reasons, among them detectors latching superconducting and rendering an entire multiplexed comb inoperable. Addressing this issue and others in operating the full array are currently active areas of investigation.

The beam offsets from these fits are used to co-add maps. Figure 6.2(b) shows a composite co-added map for each wafer in the focal plane. The best fit elliptical Guassian fit to each effective wafer beam is over-plotted, exaggerated by a factor of four, to illustrate the ellipticity orientation as a function of field position. The full focal plane co-add is shown in Figure 6.2(e), plotted on a decibel scale to highlight the near-sidelobes of the beam.

Differential beam properties were also measured from these maps. The results, shown in Figures 6.3(a) and 6.3(b) for the two largest contributions from differential pointing and ellipticity, are similar to those found with the Cedar Flat focal plane, and therefore well within our requirements.

6.1.2 $\eta\Delta\nu$ and noise analysis

Using the same methods discussed in Sections 4.1.2 and 4.1.3, we found $\eta\Delta\nu$ and NETs for detectors in the focal plane. Similar to our lab measurements, $\eta\Delta\nu$ is consistent with expectations for a ∼35% overall efficiency given the measured bands of ∼34 GHz. Tuning of the array to optimize NETs and yield is still an active area of investigation, so we do not present results here. The array is nearing expected

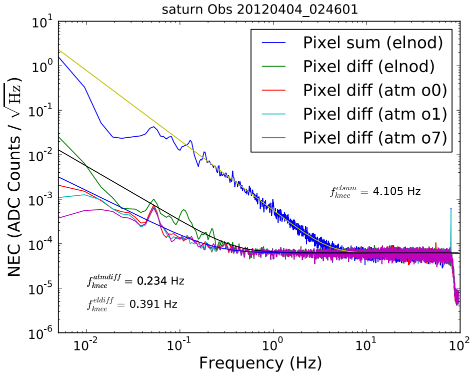

Figure 6.4: Sum and difference timestream noise during a Saturn observation in Chile.

sensitivity given the current yield, with a substantial fraction of detectors operating with NET $< 550\,\mu\mathrm{K_{cmb}}\sqrt{\mathrm{s}}$.

Figure 6.1.2 shows a comparison of different relative gain calibration methods for an example pixel. We are currently still investigating optimal relative gain calibration methods to improve our atmospheric rejection in polarization detection.

6.2 Preliminary science scans

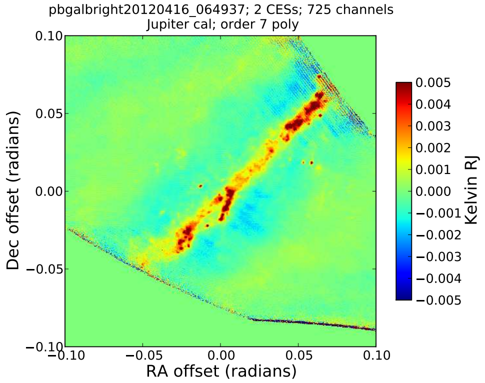

Figure 6.5: Preliminary map of the the galaxy.

While many complications have yet to be addressed in the integration of the instrument, we have started running preliminary scans of the sky on larger 'science-like' patches to begin to tackle issues in data acquisition and analysis. The resulting map from a scan across the galactic center is shown in Figure 6.5. The map was made

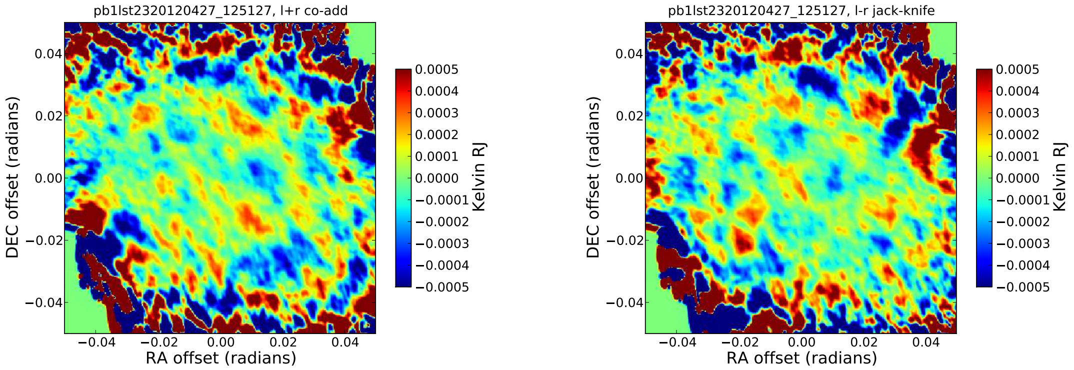

(a) Preliminary co-added map of left-going and right-going half-scans of a PB1LST23 patch observation.

(b) Preliminary jack-knife map of left-going and right-going half-scans of a PB1LST23 patch observation.

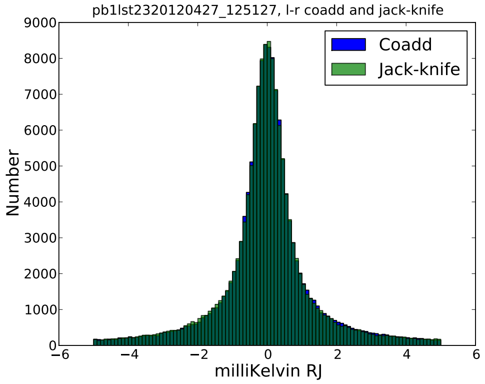

(c) Comparison of the histograms of the co-add and jack-knife maps shown in Figures 6.6(a) and 6.6(b), repsectively. The distributions overlap quite well, indicating that this dataset is still noise dominated.

Figure 6.6: Preliminary sky maps. In all maps, the temperature gain is referenced to a planet map using the stimulator response before each observation.

using data from 725 detectors. The bright features along the diagonal of the map are well correlated with features seen in WMAP maps of the same region. The blue features seen on either side of the galactic structure are artifacts from our polynomial removal filter. A proper treatment of this data would mask the galaxy when applying the filter, but this has not yet been implemented.

Similar maps have been made on our planned CMB patches. A co-added map of several constant elevation scans (CESs) of our patch PB1LST23 is shown in Figure

6.6(a). Figure 6.6(b) shows the jack-knife map made by differencing maps of only left-going and right-going half-scans during the observation. As Figure 6.6(c) illustrates more clearly, the noise properties of the maps are nearly identical, showing that we are still noise-dominated. A detection of CMB temperature power is eminent as more integration time is accumulated.

Bibliography

[1] A. A. Penzias and R. W. Wilson. “A Measurement of Excess Antenna Temperature at 4080 Mc/s.” In: *Astrophysical Journal* 142 (July 1965), pp. 419–421.

[2] D. J Fixsen et al. “The Cosmic Microwave Background Spectrum from the Full COBE FIRAS Data Set”. In: *Astrophysical Journal v.473* 473 (1996), p. 576.

[3] C. L Bennett et al. “Four-Year COBE DMR Cosmic Microwave Background Observations: Maps and Basic Results”. In: *Astrophysical Journal Letters v.464* 464 (1996), p. L1.

[4] E. Torbet et al. “A measurement of the angular power spectrum of the microwave background made from the high chilean andes”. In: *Astrophys.J.* 521 (1999), pp. L79–L82. eprint: `astro-ph/9905100`.

[5] A.D. Miller et al. “A measurement of the angular power spectrum of the cmb from l = 100 to 400”. In: *Astrophys.J.* 524 (1999), pp. L1–L4. eprint: `astro-ph/9906421`.

[6] C.B. Netterfield et al. “A measurement by Boomerang of multiple peaks in the angular power spectrum of the cosmic microwave background”. In: *Astrophys.J.* 571 (2002), pp. 604–614. eprint: `astro-ph/0104460`.

[7] S. Hanany et al. “MAXIMA-1: A Measurement of the cosmic microwave background anisotropy on angular scales of 10 arcminutes to 5 degrees”. In: *Astrophys.J.* 545 (2000), p. L5. eprint: `astro-ph/0005123`.

[8] N. W. Halverson et al. “DASI First Results: A Measurement of the Cosmic Microwave Background Angular Power Spectrum”. In: *Astrophys. J.* 568 (2002), pp. 38–45. eprint: `astro-ph/0104489`.

[9] C. L. Reichardt et al. “High-Resolution CMB Power Spectrum from the Complete ACBAR Data Set”. In: *The Astrophysical Journal* 694 (Apr. 2009), pp. 1200–1219. eprint: `0801.1491`.

[10] M. Lueker et al. “Measurements of Secondary Cosmic Microwave Background Anisotropies with the South Pole Telescope”. In: *The Astrophysical Journal* 719 (Aug. 2010), pp. 1045–1066. eprint: `0912.4317`.

[11] S. Das et al. “Detection of the Power Spectrum of Cosmic Microwave Background Lensing by the Atacama Cosmology Telescope”. In: *Physical Review Letters* 107.2, 021301 (July 2011), p. 021301. eprint: `1103.2124`.

[12] S. Das et al. “The Atacama Cosmology Telescope: A Measurement of the Cosmic Microwave Background Power Spectrum at 148 and 218 GHz from the 2008 Southern Survey”. In: *The Astrophysical Journal* 729, 62 (Mar. 2011), p. 62. eprint: `1009.0847`.

[13] E. Shirokoff et al. “Improved Constraints on Cosmic Microwave Background Secondary Anisotropies from the Complete 2008 South Pole Telescope Data”. In: *The Astrophysical Journal* 736, 61 (July 2011), p. 61. eprint: `1012.4788`.

[14] John Kovac et al. “Detection of polarization in the cosmic microwave background using DASI”. In: *Nature* 420 (2002), pp. 772–787. eprint: `astro-ph/0209478`.

[15] QUIET Collaboration et al. “First Season QUIET Observations: Measurements of CMB Polarization Power Spectra at 43 GHz in the Multipole Range $25 \leq l \leq 475$”. In: *arXiv* astro-ph.CO (2010). eprint: `1012.3191v2`.

[16] M. L. Brown et al. “Improved Measurements of the Temperature and Polarization of the Cosmic Microwave Background from QUaD”. In: *Astrophys.J.* 705 (Nov. 2009), pp. 978–999. eprint: `0906.1003`.

[17] H. C. Chiang et al. “Measurement of Cosmic Microwave Background Polarization Power Spectra from Two Years of BICEP Data”. In: *Astrophys.J.* 711 (Mar. 2010), pp. 1123–1140. eprint: `0906.1181`.

[18] C. Pryke et al. “Second and Third Season QUaD Cosmic Microwave Background Temperature and Polarization Power Spectra”. In: *The Astrophysical Journal* 692 (Feb. 2009), pp. 1247–1270. eprint: `0805.1944`.

[19] Thomas E. Montroy et al. “A Measurement of the CMB <EE> spectrum from the 2003 flight of BOOMERANG”. In: *Astrophys.J.* 647 (2006), pp. 813–822. eprint: `astro-ph/0507514`.

[20] Francesco Piacentini et al. “A Measurement of the polarization-temperature angular cross power spectrum of the cosmic microwave background from the 2003 flight of BOOMERANG”. In: *Astrophys.J.* 647 (2006), pp. 833–839. eprint: `astro-ph/0507507`.

[21] C. Bischoff et al. “New Measurements of Fine-Scale CMB Polarization Power Spectra from CAPMAP at Both 40 and 90 GHz”. In: *Astrophys.J.* 684 (2008), pp. 771–789. eprint: `0802.0888`.

[22] J. L Sievers et al. “Implications of the Cosmic Background Imager Polarization Data”. In: *The Astrophysical Journal* 660 (2007), p. 976.

[23] Sean Carroll. *Spacetime and Geometry: An Introduction to General Relativity*. Benjamin Cummings, 2003.

[24] A. Friedman. “Über die Krümmung des Raumes”. In: *Zeitschrift für Physik A Hadrons and Nuclei* 10 (1922), pp. 377–386.

[25] G. Lemaître. “Un Univers homogène de masse constante et de rayon croissant rendant compte de la vitesse radiale des nébuleuses extra-galactiques”. In: *Annales de la Societe Scietifique de Bruxelles* 47 (1927), pp. 49–59.

[26] E. Hubble. “A Relation between Distance and Radial Velocity among Extra-Galactic Nebulae”. In: *Proceedings of the National Academy of Science* 15 (Mar. 1929), pp. 168–173.

[27] Alan H. Guth. “Inflationary universe: A possible solution to the horizon and flatness problems”. In: *Phys. Rev. D* 23.2 (1981), pp. 347–356.

[28] Andreas Albrecht and Paul J. Steinhardt. “Cosmology for Grand Unified Theories with Radiatively Induced Symmetry Breaking”. In: *Phys. Rev. Lett.* 48.17 (1982), pp. 1220–1223.

[29] Andrei D. Linde. “A New Inflationary Universe Scenario: A Possible Solution of the Horizon, Flatness, Homogeneity, Isotropy and Primordial Monopole Problems”. In: *Phys. Lett.* B108 (1982), pp. 389–393.

[30] Daniel Baumann et al. “CMBPol Mission Concept Study: Probing Inflation with CMB Polarization”. In: *arXiv* astro-ph (2008). eprint: `0811.3919v2`.

[31] D Larson et al. “Seven-year Wilkinson Microwave Anisotropy Probe (WMAP) Observations: Power Spectra and WMAP-derived Parameters”. In: *The Astrophysical Journal Supplement* 192 (2011), p. 16.

[32] Antony Lewis, Anthony Challinor, and Anthony Lasenby. “Efficient Computation of Cosmic Microwave Background Anisotropies in Closed Friedmann-Robertson-Walker Models”. In: *The Astrophysical Journal* 538 (2000), p. 473.

[33] Wayne Hu and Martin White. “A New Test of Inflation”. In: *Phys. Rev. Lett.* 77 (1996), p. 1687.

[34] Wayne Hu and Martin White. “Acoustic Signatures in the Cosmic Microwave Background”. In: *Astrophysical Journal v.471* 471 (1996), p. 30.

[35] Scott Dodelson. “Coherent Phase Argument for Inflation”. In: *arXiv* hep-ph (2003).

[36] Wayne Hu, David N. Spergel, and Martin White. “Distinguishing causal seeds from inflation”. In: *Phys. Rev. D* 55.6 (1997), pp. 3288–3302.

[37] Robert Crittenden, Richard L Davis, and Paul J Steinhardt. “Polarization of the Microwave Background Due to Primordial Gravitational Waves”. In: *Astrophysical Journal Letters v.417* 417 (1993), p. L13.

[38] R Keisler et al. “A Measurement of the Damping Tail of the Cosmic Microwave Background Power Spectrum with the South Pole Telescope”. In: *The Astrophysical Journal* 743 (2011), p. 28.

[39] Arthur Kosowsky. “Introduction to microwave background polarization”. In: *New Astronomy Reviews* 43.2-4 (1999), pp. 157 –168. ISSN: 1387-6473.

[40] Marc Kamionkowski, Arthur Kosowsky, and Albert Stebbins. “Statistics of cosmic microwave background polarization”. In: *Phys. Rev. D* 55.12 (1997), pp. 7368–7388.

[41] Matias Zaldarriaga and Uroš Seljak. “All-sky analysis of polarization in the microwave background”. In: *Phys. Rev. D* 55.4 (1997), pp. 1830–1840.

[42] Wayne Hu and Martin White. “A CMB polarization primer”. In: *New Astronomy* 2 (1997), p. 323.

[43] Antony Lewis and Anthony Challinor. “Weak gravitational lensing of the CMB”. In: *Physics Reports* 429 (2006), p. 1.

[44] Kendrick M Smith et al. “CMBPol Mission Concept Study: Gravitational Lensing”. In: *arXiv* astro-ph (2008). eprint: `0811.3916v1`.

[45] A. van Engelen et al. “A measurement of gravitational lensing of the microwave background using South Pole Telescope data”. In: *arXiv* astro-ph.CO (2012).

[46] N. J Miller, M Shimon, and B. G Keating. “CMB beam systematics: Impact on lensing parameter estimation”. In: *Phys. Rev. D* 79 (2009), p. 63008.

[47] Kendrick M Smith, Wayne Hu, and Manoj Kaplinghat. “Weak lensing of the CMB: Sampling errors on B modes”. In: *Physical Review D* 70 (2004), p. 43002.

[48] Manoj Kaplinghat, Lloyd Knox, and Yong-Seon Song. “Determining Neutrino Mass from the CMB Alone”. In: *arXiv* astro-ph (2003).

[49] Wayne Hu and Takemi Okamoto. “Mass Reconstruction with Cosmic Microwave Background Polarization”. In: *The Astrophysical Journal* 574 (2002), p. 566.

[50] Dorothea Samtleben, Suzanne Staggs, and Bruce Winstein. “The Cosmic Microwave Background for Pedestrians: A Review for Particle and Nuclear Physicists”. In: *arXiv* astro-ph (2008).

[51] Shaul Hanany and Philip Rosenkranz. “Polarization of the atmosphere as a foreground for cosmic microwave background polarization experiments”. In: *New Astronomy Reviews* 47 (2003), p. 1159.

[52] Brian Keating et al. “Large Angular Scale Polarization of the Cosmic Microwave Background Radiation and the Feasibility of Its Detection”. In: *Astrophysical Journal v.495* 495 (1998), p. 580.

[53] J. M Gildemeister, Adrian T Lee, and P. L Richards. “A fully lithographed voltage-biased superconducting spiderweb bolometer”. In: *Applied Physics Letters* 74 (1999), p. 868.

[54] Michael J Myers et al. “Arrays of antenna-coupled bolometers using transition edge sensors”. In: *Nuclear Instruments and Methods in Physics Research Section A* 520 (2004), p. 424.

[55] Michael J Myers et al. “An antenna-coupled bolometer with an integrated microstrip bandpass filter”. In: *Applied Physics Letters* 86.11 (2005), p. 114103.

[56] C. L Kuo et al. “Antenna-coupled TES bolometer arrays for CMB polarimetry”. In: *Millimeter and Submillimeter Detectors and Instrumentation for Astronomy IV. Edited by Duncan* 7020 (2008), p. 38.

[57] P Richards. “Bolometers for infrared and millimeter waves”. In: *J. Appl. Phys.* (1994).

[58] Daniel O’Dea, Anthony Challinor, and Bradley R Johnson. “Systematic errors in cosmic microwave background polarization measurements”. In: *Monthly Notices of the Royal Astronomical Society* 376 (2007), p. 1767.

[59] Wayne Hu, Matthew M Hedman, and Matias Zaldarriaga. “Benchmark parameters for CMB polarization experiments”. In: *Physical Review D* 67 (2003), p. 43004.

[60] Meir Shimon et al. “CMB polarization systematics due to beam asymmetry: Impact on inflationary science”. In: *Phys. Rev. D* 77 (2008), p. 83003.

[61] Max Tegmark. “CMB mapping experiments: A designer’s guide”. In: *Physical Review D (Particles* 56 (1997), p. 4514.

[62] Lloyd Knox. “Determination of inflationary observables by cosmic microwave background anisotropy experiments”. In: *Physical Review D (Particles* 52 (1995), p. 4307.

[63] J. R Bond, G Efstathiou, and M Tegmark. “Forecasting cosmic parameter errors from microwave background anisotropy experiments”. In: *Royal Astronomical Society* 291 (1997), p. L33.

[64] Andrew H Jaffe, Marc Kamionkowski, and Limin Wang. “Polarization pursuers’ guide”. In: *Physical Review D (Particles* 61 (2000), p. 83501.

[65] Emory F Bunn et al. “E/B decomposition of finite pixelized CMB maps”. In: *Physical Review D* 67 (2003), p. 23501.

[66] Antony Lewis, Anthony Challinor, and Neil Turok. “Analysis of CMB polarization on an incomplete sky”. In: *Phys. Rev. D* 65 (2002), p. 23505.

[67] Kendrick M Smith. “Pseudo-C_l estimators which do not mix E and B modes”. In: *Phys. Rev. D* 74 (2006), p. 83002.

[68] Tom Crawford. "Power spectrum sensitivity of raster-scanned CMB experiments in the presence of 1/f noise". In: *Phys. Rev. D* 76 (2007), p. 63008.

[69] B. R Johnson et al. "MAXIPOL: Cosmic Microwave Background Polarimetry Using a Rotating Half-Wave Plate". In: *The Astrophysical Journal* 665 (2007), p. 42.

[70] Britt Reichborn-Kjennerud et al. "EBEX: a balloon-borne CMB polarization experiment". In: *Proceedings of SPIE* 7741.1 (2010), p. 77411C.

[71] M. C Runyan et al. "Design and performance of the Spider instrument". In: *arXiv* astro-ph.IM (2011).

[72] G Savini, G Pisano, and PAR Ade. "Achromatic half-wave plate for submillimeter instruments in cosmic microwave background astronomy: modeling and simulation". In: *Applied Optics* 45.35 (2006), pp. 8907–8915.

[73] G Pisano et al. "Achromatic half-wave plate for submillimeter instruments in cosmic microwave background astronomy: experimental characterization". In: *Applied Optics* 45.27 (2006), pp. 6982–6989.

[74] M Betoule et al. "Measuring the tensor to scalar ratio from CMB B-modes in the presence of foregrounds". In: *Astronomy and Astrophysics* 503 (2009), p. 691.

[75] J Dunkley et al. "CMBPol Mission Concept Study: Prospects for polarized foreground removal". In: *arXiv* astro-ph (2008).

[76] C. Dragone. "Offset multireflector antennas with perfect pattern symmetry and polarization discrimination". In: *ATT Tech. J.* 57 (1978), 26632684.

[77] M. Akagawa Y. Mizugutch and H. Yokoi. "Offset dual reflector antenna". In: *IEEE International Symposium on Antennas and Propagation* (1976), 25.

[78] H Tran et al. "Comparison of the crossed and the Gregorian Mizuguchi-Dragone for wide-field millimeter-wave astronomy". In: *Applied Optics* 47.2 (2008), pp. 103–109.

[79] J. Ruze. "Antenna tolerance theory, A review". In: *Proceedings of the IEEE* 54.4 (1966), pp. 633 –640. ISSN: 0018-9219.

[80] J. M. Gildemeister, Adrian T. Lee, and P. L. Richards. "A fully lithographed voltage-biased superconducting spiderweb bolometer". In: *Applied Physics Letters* 74.6 (1999), pp. 868 –870. ISSN: 0003-6951.

[81] J. Mehl et al. "TES Bolometer Array for the APEX-SZ Camera". In: *Journal of Low Temperature Physics* 151 (2008), pp. 697–702.

[82] E. Shirokoff et al. "The South Pole Telescope SZ-Receiver Detectors". In: *Applied Superconductivity, IEEE Transactions on* 19.3 (2009), pp. 517 –519. ISSN: 1051-8223.

[83] D. Schwan et al. “The APEX-SZ Instrument”. In: *ArXiv e-prints* (Aug. 2010). eprint: `1008.0342`.

[84] J. E. Carlstrom et al. “The 10 Meter South Pole Telescope”. In: *ArXiv e-prints* (July 2009). eprint: `0907.4445`.

[85] G Chattopadhyay and J Zmuidzinas. “A dual-polarized slot antenna for millimeter waves”. In: *Antennas and Propagation, IEEE Transactions on* 46.5 (1998), pp. 736 –737.

[86] J Zmuidzinas et al. “Low-noise slot antenna SIS mixers”. In: *Applied Superconductivity, IEEE Transactions on* 5.2 (1995), pp. 3053 –3056.

[87] D.F Filipovic, S.S Gearhart, and G.M Rebeiz. “Double-slot antennas on extended hemispherical and elliptical silicon dielectric lenses”. In: *Microwave Theory and Techniques, IEEE Transactions on* 41.10 (1993), pp. 1738–1749.

[88] Kam Stahly Arnold. “Design and Deployment of the Polarbear Cosmic Microwave Background Polarization Experiment”. PhD thesis. University of California, Berkeley, 2010.

[89] Jongsoo Yoon et al. “Single superconducting quantum interference device multiplexer for arrays of low-temperature sensors”. In: *Applied Physics Letters* 78 (2001), p. 371.

[90] T Lanting et al. “A frequency-domain SQUID multiplexer for arrays of transition-edge superconducting sensors”. In: *Applied Superconductivity, IEEE Transactions on* 13.2, Part 1 (2003), pp. 626 –629.

[91] T. M Lanting et al. “Frequency domain multiplexing for bolometer arrays”. In: *Nuclear Instruments and Methods in Physics Research Section A* 520 (2004), p. 548.

[92] T. M Lanting et al. “Frequency-domain multiplexed readout of transition-edge sensor arrays with a superconducting quantum interference device”. In: *Applied Physics Letters* 86 (2005), p. 2511.

[93] T Lanting et al. “Frequency-domain SQUID multiplexing of transition-edge sensors”. In: *Applied Superconductivity, IEEE Transactions on* 15.2, Part 1 (2005), pp. 567 –570.

[94] T. M Lanting et al. “Frequency-domain readout multiplexing of transition-edge sensor arrays”. In: *Nuclear Instruments and Methods in Physics Research Section A* 559 (2006), p. 793.

[95] J. A Chervenak et al. “Superconducting multiplexer for arrays of transition edge sensors”. In: *Applied Physics Letters* 74 (1999), p. 4043.

[96] Martin Lueker. “Measurements of Secondary Cosmic Microwave Background Anisotropies with the South Pole Telescope”. PhD thesis. University of California, Berkeley, 2010.

[97] Trevor Michael Lanting. “Multiplexed readout of superconducting bolometers for cosmological observations”. PhD thesis. University of California, Berkeley, 2006.

[98] Adrian T Lee et al. “A superconducting bolometer with strong electrothermal feedback”. In: *Applied Physics Letters* 69 (1996), p. 1801.

[99] A.T Lee et al. “Voltage-biased high-T¡sub¿c¡/sub¿ superconducting infrared bolometers with strong electrothermal feedback”. In: *Applied Superconductivity, IEEE Transactions on* 7.2 (1997), pp. 2378–2381.

[100] Shih-Fu Lee et al. “Voltage-Biased Superconducting Transition-Edge Bolometer with Strong Electrothermal Feedback Operated at 370 mK”. In: *Applied Optics* 37 (1998), p. 3391.

[101] B Steinbach Z. Kermish. *DfMux Noise Calculations*. `http://bolowiki.berkeley.edu/twiki/bin/view/Main/DfMUXNoiseCalculation`.

[102] B Steinbach. *Nulling IV Curves*. Internal Memo.

[103] M Lueker et al. “Thermal Design and Characterization of Transition-Edge Sensor (TES) Bolometers¡newline/¿ for Frequency-Domain Multiplexing”. In: *Applied Superconductivity, IEEE Transactions on* 19.3 (2009), pp. 496–500.

[104] John C Mather. “Bolometer noise: nonequilibrium theory”. In: *Applied Optics* 21.6 (3), pp. 1125–1129.

[105] G Smecher. *DMFD Mixer Transfer Functions*. `http://kingspeak.physics.mcgill.ca/twiki/bin/view/DigitalFMux/DMFDMixerTransferFunctions`.

[106] R. S. Bhatia et al. “A three-stage helium sorption refrigerator for cooling of infrared detectors to 280 mK”. In: *Cryogenics* 40.11 (2000), pp. 685 –691. ISSN: 0011-2275.

[107] L Risegari et al. “Very-low-temperature thermal conductivity of polymeric supports for massive cryogenic detectors”. In: *Proceedings of 8th International Conference on Advanced Technology and Particle Physics* (2003).

[108] M Barucci et al. “Low temperature thermal conductivity of Kapton and Upilex”. In: *Cryogenics* (2000).

[109] ED Marquardt, JP Le, and R Radebaugh. “Cryogenic material properties database”. In: *Cryocoolers 11* (2002), pp. 681–687.

[110] A Connolly and K Mendelssohn. “Thermal Conductivity of Tantalum and Niobium Below 1°K”. In: *Proceedings of the Royal Society of London. Series AMathematical and Physical Sciences* (1962), pp. 429–439.

[111] J Olson. “Thermal conductivity of some common cryostat materials between 0.05 and 2 K”. In: *Cryogenics(Guildford)* (1993).

[112] J.S. Accetta and D.L. Shumaker. *The Infrared and electro-optical systems handbook*. The Infrared and electro-optical systems handbook. Infrared Information Analysis Center, 1993. ISBN: 9780819410726.

[113] R. Siegel and J.R. Howell. *Thermal radiation heat transfer*. Taylor & Francis, 2002. ISBN: 9781560328391.

[114] SL Bapat, KG Narayankhedkar, and TP Lukose. “Performance prediction of multilayer insulation”. In: *Cryogenics* 30.8 (1990), pp. 700–710.

[115] G.R. Cunnington C.W. Keller and A.P. Glassford. “Final report on thermal performance of multilayer insulations”. In: *NASA Report CR-134477* (1974).

[116] SL Bapat, KG Narayankhedkar, and TP Lukose. “Experimental investigations of multilayer insulation”. In: *Cryogenics* 30.8 (1990), pp. 711–719.

[117] P Ade et al. “A review of metal mesh filters”. In: *Proceedings of SPIE* 6275 (2006).

[118] C Tucker and P Ade. “Thermal filtering for large aperture cryogenic detector arrays”. In: *Proceedings of SPIE* 6275 (2006).

[119] D Benford, M Gaidis, and J Kooi. “Optical properties of Zitex in the infrared to submillimeter”. In: *Applied Optics* (2003).

[120] S Rosenblum, W Styert, and F Fickett. “A simple method for producing high conductivity copper for low temperature applications”. In: *CRYOGENICS* 17.11 (1977), pp. 645–647.

[121] Adam L Woodcraft. “Recommended values for the thermal conductivity of aluminium of different purities in the cryogenic to room temperature range, and a comparison with copper”. In: *Cryogenics* 45 (2005), p. 626.

[122] E Gmelin et al. “REVIEW ARTICLE: Thermal boundary resistance of mechanical contacts between solids at sub-ambient temperatures”. In: *Journal of Physics D: Applied Physics* 32 (1999), p. 19.

[123] A. L Woodcraft. “COMMENT: Comment on ‘thermal boundary resistance of mechanical contacts between solids at sub-ambient temperatures’”. In: *Journal of Physics D: Applied Physics* 34 (2001), p. 2932.

[124] LJ Salerno, P Kittel, and AL Spivak. “Thermal conductance of augmented pressed metallic contacts at liquid helium temperatures”. In: *Cryogenics* 33.12 (1993), pp. 1104–1109.

[125] P Kittel, L Salerno, and A Spivak. “Thermal conductance of pressed bimetallic contacts at liquid nitrogentemperatures”. In: *Cryogenics* 34 (1994), pp. 389–392.

[126] L Salerno, P Kittel, and A Spivak. “Thermal conductance of pressed metallic contacts augmented with indium foil or Apiezon grease at liquid helium temperatures?” In: *Cryogenics* 34.8 (1994), pp. 649–654.

[127] Erin Quealy. PhD thesis. University of California, Berkeley,

[128] William H. Press et al. *Numerical Recipes 3rd Edition: The Art of Scientific Computing*. 3rd ed. New York, NY, USA: Cambridge University Press, 2007. ISBN: 0521880688, 9780521880688.

[129] L Genzel K Sakai. “Interferometry from 1950 to the present”. In: *J. Opt. Soc. Am., JOSA* 67.7 (7), pp. 871–879.

[130] PL Richards. “High-resolution Fourier transform spectroscopy in the far-infrared”. In: *J. Opt. Soc. Am., JOSA* 54.12 (1964), pp. 1474–1484.